FOREWORD

This report was prepared by The Carborundum Company under USAF Contract No. AF 33 (616)-6806. This contract was initiated under Project No. 7350, "Ceramic and Cermet Materials," Task No. 73500, "Ceramic and Cermet Materials Development." The work was administered under the direction of the Directorate of Materials and Processes, Deputy for Technology, Aeronautical Systems Division, with Mr. K. S. Mazdiyasni acting as project engineer.

This report covers work conducted from October 1960 to December 1961.

The research has been conducted by the Applied Research Branch, Research and Development Division, of The Carborundum Company under the supervision of Dr. W. A. Lambertson.

ABSTRACT

An investigation of the material properties which affect the thermal shock resistance of polyphase ceramic systems composed of a high Young's modulus continuous phase containing a low Young's modulus dispersed phase has been conducted using the model system zirconium carbide-graphite.

The principal effect of the dispersed phase of graphite on the thermal shock resistance of the zirconium carbide is to reduce the degree of damage resulting from fracture by thermal shock.

The presence of the graphite also causes a decrease in strength and Young's modulus of elasticity in such a manner as to decrease the elastic energy stored at fracture and at higher volume fractions graphite to increase the extensibility (i.e., strain at fracture). Suitable thermal shock damage resistance factors were derived.

The coefficient of thermal expansion and Poisson's ratio to a first approximation were independent of graphite content.

Due to the relative differences in thermal properties the graphite causes an increase in thermal conductivity, thermal diffusivity and emissivity. Porosity was found to be a major variable.

Emissivity (absorptivity) was introduced as a variable affecting thermal shock resistance of ceramic materials. A quantitative theory of thermal shock by radiation was developed. Excellent agreement with experiment was shown. Calculations were carried out of the transient temperatures and thermal stresses in a sphere subjected to thermal shock in a medium with constant surface heat transfer coefficient. It was found that at the time of maximum stress the sphere is still close to its initial temperature. Using these results, thermal shock data in the literature were recalculated. Good agreement with experiment was shown.

PUBLICATION REVIEW

This report has been reviewed and is approved.

FOR THE COMMANDER:

W. G. RAMKE
Chief, Ceramics and Graphite Branch
Metals and Ceramics Laboratory
Materials Central

TABLE OF CONTENTS

TABLE OF CONTENTS (cont'd)

LIST OF TABLES

LIST OF TABLES (cont'd)

LIST OF FIGURES

LIST OF FIGURES (cont'd)

LIST OF FIGURES (cont'd)

LIST OF FIGURES (cont'd)

I. INTRODUCTION

Demands by the aircraft and missile industries for materials capable of withstanding severe erosive and thermal conditions are rapidly increasing. Many of the limits of temperature and erosion resistance eliminate metals and alloys from consideration. Ceramic materials, although possessing excellent high temperature properties, are generally limited because of poor thermal shock resistance.

Recently, ceramic bodies were developed based on a high Young's modulus continuous phase and a low Young's modulus dispersed phase with markedly improved thermal shock resistance(1).

The purpose of this research project was to determine the fundamental reasons for the improved thermal shock resistance of these composite bodies and to extend the concept of high Young's modulus continuous phase-low Young's modulus dispersed phase ceramic materials to new classes of refractory materials systems.

The material properties which principally determine the thermal shock resistance of ceramic materials* are: tensile strength, Young's modulus of elasticity, Poisson's ratio, coefficient of thermal expansion, thermal conductivity, thermal diffusivity and emissivity. Each of these is a function of temperature. For a polyphase system, additional variables are: volume fraction and distribution of the dispersed phase, particle size and particle shape. Porosity, which is usually present in ceramic bodies, introduces a major variable which strongly affects mechanical properties and to a lesser extent thermal properties. Another variable introduced when correlating thermal shock test data with the physical properties is the effect of the volume under stress on the strength value obtained. This depends on the homogeneity of the material, i.e., distribution of flaws. The effective surface energy required for crack propagation is a variable affecting the damage to be incurred after fracture has been nucleated. This damage is also a function of the elastic energy stored at fracture available for crack propagation.

All these material properties in combination affect the thermal shock behavior of polyphase ceramic bodies.

The number of variables to be investigated, therefore, amounts to a total of sixteen. Many of these variables are interdependent, thereby greatly complicating the investigation.

* For an excellent quantitative treatment of the thermal shock resistance of ceramic materials the reader is referred to the January issue of the Journal of the American Ceramic Society, 1955.

Manuscript released by authors February 1962 for publication as a WADD Technical Report.

The rate of effort expended on each variable depended on its relative importance and on the significance of the results obtained. Many variables were investigated only to allow correlation of the thermal shock test data with the individual physical properties obtained.

The major effort was directed towards a measurement of the mechanical properties, strength, and Young's modulus of elasticity. These were investigated as a function of temperature, composition, particle size, porosity, and anisotropy.

The investigation extended over a period of two years. The results obtained in the first year were reported previously in WADD TR 60-749, Part I[2]. The present report deals with observations made in the second year of the investigation. For the convenience of the readers a brief summary of the first report appears below.

A. Summary of First Report

The principal factors affecting the thermal shock resistance of ceramic materials were discussed.

The material system studied in this investigation consisted of zirconium carbide containing a dispersed phase of graphite. Zirconium carbide has a Young's modulus of elasticity of approximately 65×10^6 psi, whereas graphite has a Young's modulus of elasticity of approximately 1.5×10^6 psi.

It was shown, based on theoretical solutions of the elastic constants of heterogeneous systems[3], and the stress concentration factors around spherical particles[4], that to a first approximation for the system under study the graphite can be regarded as a dispersed phase of voids. The effect of the graphite on the mechanical properties of the zirconium carbide will, to a first approximation, be similar to the effect of porosity. It was shown that the internal stresses which will exist in composite bodies of different coefficients of thermal expansion, which could affect strength, are of orders of magnitude lower than the internal stresses expected in a composite material containing phases with Young's moduli of elasticity comparable to zirconium carbide. The maximum stress expected in the zirconium carbide phase was calculated to be approximately 1,900 psi.

Expressions were given for the coefficient of thermal expansion, thermal conductivity, and thermal diffusivity of the two-phase system. Little change in the coefficient of thermal expansion is to be expected while the zirconium carbide remains the continuous phase. The effect of addition of a low Young's modulus dispersed phase to a high Young's modulus continuous phase on the thermal conductivity and thermal diffusivity will depend on the relative thermal conductivity and thermal diffusivity of the components. If the dispersed phase has the higher thermal conductivity, the overall thermal conductivity will be increased, leading

to an increase in thermal shock resistance. If the dispersed phase has the lower thermal conductivity, the overall thermal conductivity will be lowered, thereby decreasing the thermal shock resistance.

The major variables in this investigation were, therefore, Young's modulus of elasticity and the tensile strength. It was predicted and experimentally verified that the addition of the graphite would lead to an increase in the strain at fracture (ratio of strength to Young's modulus of elasticity) and thereby lead to an increase in thermal shock resistance.

The experimental section in the first report described the various methods and results obtained for the measurements of the physical properties discussed above. Preliminary thermal shock results were given.

B. Summary of the Present Report

The present report deals principally with the experimental determinations of the material properties and thermal shock behavior of composites of zirconium carbide-graphite. Emissivity and the elastic energy stored at fracture were introduced as material variables affecting the thermal shock resistance of ceramic materials. The increase in thermal shock resistance with graphite content is principally due to the increase in the strain at fracture, a substantial decrease in the elastic energy stored at fracture and to a lesser degree to an increase in the thermal conductivity and diffusivity. The major effect of the graphite on the thermal shock resistance of the zirconium carbide is that the damage resulting from thermal shock is decreased considerably. The increase in emissivity with graphite content is the only factor lowering the thermal shock resistance for conditions of thermal shock where thermal radiation is the principal mechanism of heat transfer.

A complete quantitative theory for thermal shock on heating by thermal radiation was developed (Appendix B). Suitable thermal stress resistance parameters for thermal shock by radiation were derived. Excellent agreement is found between theory and experiment. To the best of the authors' knowledge this is the first quantitative treatment of thermal shock by radiation.

The elastic energy stored at fracture, which provides the driving force for crack propagation, will affect the thermal shock behavior of ceramic materials after fracture has been nucleated. Here too, suitable thermal shock damage resistance parameters were derived by which ceramic materials can be compared on the basis of the relative damage which can be expected on thermal shock.

Other possible material properties which could affect the fracture behavior of composite materials are the effective surface energy required for crack propagation and the dispersion and attenuation of stress waves accompanying the propagating crack at the elastic discontinuities at the boundaries

of the two phases.

Thermal stress calculations were carried out for a sphere subjected to thermal shock in a medium with constant surface heat transfer coefficient. On the basis of these calculations the predictions by Crandall and Ging[5] of the thermal shock behavior of alumina spheres were recalculated. For these calculations a graphical method was devised. Excellent agreement for both heating and cooling was obtained (Appendix C).

The effect of porosity on Young's modulus of zirconium carbide was investigated. A suitable mathematical expression for the porosity dependence was suggested. The effect of graphite on Young's modulus of elasticity of zirconium carbide was also determined quantitatively. The expressions obtained were compared with equations in the literature for the elastic constants of two-phase systems. The equations for the effect of graphite and porosity on Young's modulus of elasticity were then combined to predict Young's modulus of elasticity of the three-phase system zirconium carbide-graphite-porosity.

For the convenience of the reader, derivations of many of the equations are included in the form of appendices. For purposes of continuity, tables and figures required for the derivations are included in the appendices rather than in the main body of the report.

II. EXPERIMENTAL

In this section the materials, preparation of specimens, physical property testing and experimental results are described. For experimental techniques described previously the reader is referred to WADD TR 60-749 (Part I) (hereafter referred to as Part I). Techniques employed in the second year of the research period are discussed in detail. Experimental results reported in Part I are incorporated in the present report for completeness and clarity.

A. Materials

The principal materials selected for this study were zirconium carbide and graphite. The zirconium carbide was produced by the New Products Branch of The Carborundum Company and was in the form of -325 mesh powder. The spectrographic analysis for impurities was as follows:

0.1 - 0.5 percent Fe
0.01 - 0.05 percent Cr, Ca
0.005 - 0.01 percent B, Si, Ti

The graphite was regular mold stock manufactured by the International Graphite and Electrode Company. This graphite was ground and screened to a particle size between 70 mesh and 100 mesh. A fraction was also used with a particle size 100-140 mesh, 170-200 mesh, and -325 mesh. Microscopic examination showed the individual graphite particles to be approximately equidimensional. The bulk density of the 70-100 mesh graphite was determined in a vacuum-mercury-pycnometer to be 1.77 grams per cubic centimeter.

Other materials used in this investigation consisted of a silicon carbide-graphite composite ("GRB" silicon carbide) as made by the New Products Branch of The Carborundum Company. Also used were composites made from Alumina (Alcoa A301) and Reactor Grade zirconia (Carborundum Metals Company).

B. Preparation of Test Specimens

Mixtures of zirconium carbide and graphite of various compositions ranging from 0 to 60 volume percent graphite were intimately mixed in a rotary mill. Bodies measuring 4-1/2 inches in diameter by 4 inches high were then hot pressed in graphite molds at a temperature of 2250°C and pressure of 2000 psi. All bodies with two exceptions contained graphite in the particle size range 70-100 mesh. Two bodies were manufactured containing graphite with particle size 100-140 mesh. Test specimens of suitable size and shape for the determination of the various physical properties were than cut from the hot-pressed composites by means of a diamond saw and subsequently ground on a diamond lapidary wheel. Specimens were cut parallel and perpendicular to the hot-pressing direction, as indicated in Figure 1.

For the thermal shock tests, spheres with a diameter of two inches, containing similar volume fractions of graphite as in the hot-pressed pieces described above, were hot pressed in suitable graphite sphere molds. After hot pressing, the spheres were ground to a roundness of better than 0.01 inches.

Preparation of special samples employed for the measurement of certain physical properties will be described in the section discussing experimental techniques. Fabrication techniques of the materials used, other than zirconium carbide and graphite, will be described in the section discussing their physical properties.

In order to investigate the microstructure and the degree of dispersion of graphite in the zirconium carbide-graphite composites, polished sections were prepared of all composites. Microscopic examination of the polished sections revealed that the graphite particles were distributed evenly throughout the zirconium carbide. Of great importance, the microscopic examination of the polished sections revealed that an appreciable volume fraction of voids was contained within the carbide phase. This may be observed in photomicrographs published in Part I. Since voids (or porosity) strongly affect the mechanical properties of polycrystalline ceramic materials, the presence of the voids introduced another variable which substantially complicated the investigation. Since the bodies were prepared assuming complete densification, the presence of the voids reduced the volume content of the graphite with respect to the total volume of the composite. In addition, for bodies containing higher volume contents of graphite and whose microstructure revealed little or no porosity, values for bulk density were obtained which suggested considerable densification of the graphite during the hot pressing operation. The volume content of the phases present in the composite bodies were unknown and therefore had to be determined metallographically.

Initial attempts using a systematic point count technique proved to be unsatisfactory. The method finally adopted consisted of measuring the relative area covered by the graphite on a low magnification (20X) photomicrograph. The equipment used for this consisted of a Zeiss Particle Size Analyzer Type TGZ3. As densification of the graphite takes place during the hot pressing of the composite body, the final graphite density was determined from the measured volume fraction graphite and the bulk density of composite 60A (See Table No. I). The microstructure of this body shows little or no porosity. The graphite density was calculated to be 1.915 grams per cubic centimeter.

Since the hot pressing conditions were constant for all zirconium carbide-graphite composite bodies, this value of graphite density was assumed to be constant and was used to calculate the volume fractions of the zirconium carbide and porosity in the other composite bodies. Knowing the graphite content, the density of the remaining zirconium carbide plus porosity phase was calculated from the overall bulk density. By comparing the apparent density of the

zirconium carbide with its theoretical density, the porosity could then also be calculated. The density of the zirconium carbide was taken as 6.70 grams per cubic centimeter as calculated from crystal structure data. The final results of the volume contents of the zirconium carbide, graphite and porosity for all the composites prepared are given in Table No. I. The experimental error in determining the graphite content is estimated to be approximately three percent. Due to the length of time required for these measurements, volume analysis was not performed on each of the thermal shock specimens.

From the above discussion it is clear that the composites are regarded as consisting of a continuous matrix containing a dispersed phase of graphite and a dispersed phase of porosity. The porosity is contained within the carbide phase only. The graphite is being treated as a homogeneous material. In all subsequent discussions the same assumption is made.

Since the graphite particles are considerably larger than the size of the average pore, the composite may also be regarded as a graphite phase contained with a homogeneous zirconium carbide phase having a lower density than theoretical.

In preparing the photomicrographs for the volume analysis of the composites, an indication of anisotropy within the composite with respect to the direction of hot pressing was observed. Shown in Figure 2 are photomicrographs of composites containing high graphite contents viewing the composites parallel and perpendicular to the hot pressing direction. A definite flattening of the graphite particles in the direction of hot pressing is noticeable.

C. Equipment

1. Coefficient of Thermal Expansion

The equipment used to determine the coefficient of thermal expansion was described in detail in Part I. In this period of the research project the coefficient of thermal expansion was measured over the temperature range from room temperature to 1350°C. Temperature was measured with thermocouples rather than with an optical pyrometer used previously.

2. Young's and Shear Moduli of Elasticity and Poisson's Ratio

Young's modulus of elasticity and the shear modulus of elasticity were determined by means of a flexural and torsional resonance technique described in Part I. Calculations were made by means of tables compiled for this purpose by Hasselman[6]. Specimen size was approximately three by one-half by one-quarter inches.

The equipment described in Part I for the measurement of the temperature dependence of Young's modulus proved to be unsuitable for the relatively small specimen size employed. Accordingly, the apparatus was then redesigned as shown in Figure 3. In this technique the specimen is suspended at the center from a refractory metal wire attached to the driving unit. The resonant vibrations are detected by a microphone attached directly to the furnace wall. The bent aluminum tube protects the microphone from direct radiation from the hot zone of the furnace. For all measurements in this investigation an argon protective atmosphere was used.

3. Modulus of Rupture

No changes in technique or modifications in equipment were made. Specimen size, except where noted, was three by one-half by one-quarter inches. Loading span was two and one-half inches. Equipment used to determine the modulus of rupture at high temperature was similar to that described by Shaffer[7].

4. Strain at Fracture

One of the major variables in the thermal shock resistance of brittle materials is their extensibility, i.e., the amount of deformation they can be subjected to before fracture. The higher the extensibility of a material the higher its thermal shock resistance. One measure of the extensibility of a material is the ratio of its strength to Young's modulus of elasticity. In this investigation the strain at fracture was computed from the modulus of rupture and Young's modulus of elasticity.

5. Elastic Energy Stored at Fracture

On the basis of experimental observations on the thermal shock behavior of the composites, the elastic energy stored at fracture providing the driving force for crack propagation, is introduced as a material variable affecting its thermal shock resistance.

For a sphere of radius (b) the elastic energy content at fracture (W) can be calculated to be (See Appendix A)

$$W = \frac{4\pi}{7} \quad \frac{S_t^2 (1 - \nu) b^3}{E} \qquad (1)$$

where S_t is the tensile strength of the material, ν is Poisson's ratio, and E is Young's modulus of elasticity.

The reported elastic energy stored at fracture (W) in this investigation corresponds to the energy content of a unit cube deformed by a uniaxial

tensile stress equal to the modulus of rupture determined experimentally. This is given by

$$W = \frac{S_{tb}^2}{2E} \qquad (2)$$

where S_{tb} is the modulus of rupture.

6. Impact Resistance

Since impact resistance is a measure of the elastic energy stored at fracture (area under the stress-strain curve), tests were carried out to determine the effect of graphite additions on the impact resistance of the zirconium carbide.

The equipment used is illustrated schematically in Figure 5. The impact resistance of the specimen is determined by the change in kinetic energy of the free-falling rod. In order to eliminate the effect of size and geometry, specimen configuration was kept constant (three by one-half by one-quarter inch rectangular bars). The values of impact resistance were then compared with the ratio of strength squared divided by Young's modulus of elasticity. The relative changes in impact resistance and elastic energy stored at fracture were calculated by setting the property values of zirconium carbide equal to unity.

7. Thermal Diffusivity

In order to duplicate the conditions of thermal shock for which a spherical shape was employed, a sphere was selected to determine the thermal diffusivity. This was done by measuring the transient temperature at the center when the sphere is subjected to a temperature difference. Spheres containing 0, 10, 20, 30, 40 and 50 volume percent graphite were hot pressed in two-inch diameter sphere molds. The spheres were then subsequently ground to one and three-quarter inch diameter to a roundness of better than 0.001 inches. Small holes (one-eighth inch diameter) were drilled ultrasonically to the center of the sphere. A Chromel®-Alumel® thermocouple contained within an open-ended alumina thermocouple tube was inserted into the hole. The thermocouple tube was cemented into the hole with alumina refractory cement. Thermal diffusivity measurements were made at 25°C, 200°C, 275°C and 335°C. For measurements at 200°C, 275°C and 335°C, a liquid salt*bath was employed as the heat transfer medium. Measurements could not be extended to higher temperatures due to oxidation of the zirconium carbide. To measure the transient temperature rise of the center the sphere was submerged into the salt bath and the transient temperature recorded with an x-y recorder. In order to reduce the effect of the temperature dependence of the thermal conductivity and thermal diffusivity, the temperature difference to which the sphere was subjected was approximately twenty-five degrees centigrade. In order to record the transient thermocouple

*Hitec, E. I. duPont de Nemours

output approximately full-scale on the recorder, a variable bucking voltage was incorporated in the thermocouple circuit. For the thermal diffusivity measurements at 25°C, the spheres were first brought to equilibrium in a mixture of ice and water, then plunged into a container through which water at a temperature of approximately 25°C was passed continuously. When the transient temperature of the center of the sphere was obtained the logarithm of the temperature was plotted against time. The thermal diffusivity was then calculated using equations by Carslaw and Jaeger[10] as follows:

The transient temperature (T) of a sphere subjected to a temperature difference (V), in the notation of Carslaw and Jaeger[10], is given by:

$$T = \frac{2hV}{r} \sum_{n=1}^{\infty} e^{-\kappa \alpha_n^2 t} \frac{a^2\alpha_n^2 + (ah-1)^2}{\alpha_n^2 \left[a^2\alpha_n^2 + ah\,(ah-1) \right]} \sin a\alpha_n \sin r\alpha_n \qquad (3)$$

where h is the ratio of surface heat transfer coefficient to thermal conductivity
a is the sphere radius
r is the radial coordinate
t is the time
κ is the thermal diffusivity
α_n are the roots of

$$a\alpha \cot a\alpha + ah - 1 = 0 \qquad (4)$$

This expression converges so rapidly that after a sufficient time has passed the terms beyond the first may be neglected. The temperature at the center of the sphere is then given by:

$$T = 2V \frac{\sin a\alpha_1 - a\alpha_1 \cos a\alpha_1}{a\alpha_1 - \sin a\alpha_1 \cos a\alpha_1} e^{-\kappa \alpha_1^2 t} \qquad (5)$$

which can be written:

$$T = Ne^{-nt} \qquad (6)$$

The value of n can be determined from the slope of the curve of log T plotted against time. Knowing n, the value of N is calculated. A table of the values of the expression

$$\frac{N}{2} = \frac{\sin a\alpha_1 - a\alpha_1 \cos a\alpha_1}{a\alpha_1 - \sin a\alpha_1 \cos a\alpha_1} \qquad (7)$$

will give the value of α_1, from the known value of N. Since $n = \zeta \alpha_1^2$, the thermal diffusivity is then readily calculated. Table No. II lists values of N/2 for various values of $a\alpha_1$, as computed by a Univac® electronic computer. The experimental accuracy of this method is estimated to be between five and ten percent.

8. Thermal Conductivity

The apparatus initially constructed based on a design by Francl and Kingery[8] proved to be unreliable. Reproducible results could not be obtained. Thermal conductivity was, therefore, determined using an apparatus of design similar to that described by Heikes and Ure[9] shown in Figure 4. The method consists of calculating the thermal conductivity from the known quantity of heat flowing through the sample and the temperature gradient in the sample measured after a balance between internal heater and guard heater is obtained.

Referring to Figure 4, if Q is the quantity of heat flowing through the sample of cross-sectional area A, Δx is the distance, and ΔT the temperature difference between the two thermocouples then the thermal conductivity is calculated from:

$$K = \frac{Q}{A} \frac{\Delta x}{\Delta T} \qquad (8)$$

The experimental accuracy is estimated to be better than five percent.

Since cylindrical specimens were required, these were especially hot pressed in one-inch diameter graphite molds. In preparation of these samples a graphite density was assumed to be 1.915 grams per cubic centimeter. The porosity was then calculated directly, without resorting to metallographic volume analysis described in the section Specimen Preparation.

In addition to direct experimental determination, thermal conductivity was calculated from the thermal diffusivity.

9. Emissivity (Absorptivity)

At the high temperatures employed in the thermal shock tests in this investigation, heat transfer occurs principally by thermal radiation. The emissivity of the composites is, therefore, introduced as a variable. One of the difficulties is that emissivity of a surface, in general, is a function of the spectral distribution of the radiation being received. In addition, emissivity is also a function of the temperature of the surface itself.

In the thermal shock tests employed, the specimens at the time of fracture are still close to room temperature (calculated surface temperature at time of fracture $\sim 150^{\circ}C$). The desired values for the emissivity, therefore,

were approximated by measuring the reflectivity of the composites at room temperature for the incandescent radiation from a tungsten filament lamp.

The samples used for these measurements were the polished samples used for the metallographic volume analysis described previously.

The equipment used consisted of a Reichert microscope with Ipscaphot® attachment. Placing the polished section in the microscope, the reflectivity of the polished sections was indicated by the deflection of the galvanometer attached to the photocell of the Ipscaphot® attachment. The actual reflectivities of the composites were determined by comparison with a silvered mirror with reflectivity equal to 0.93[11]. The absorptivity (emissivity) was then calculated by means of the relation

$$\text{Absorptivity} = 1 - \text{Reflectivity} \tag{9}$$

The values obtained by this technique are, therefore, the total normal absorptivity at room temperature for incandescent radiation.

10. Thermal Shock Tests

Investigating the thermal shock behavior of ceramic materials, two types of thermal shock tests can be employed. A steady state test can be selected in which a hollow cylindrical specimen is heated internally by a concentric heater. The stresses developed are a function of the temperature difference between the inner and outer surface of the cylinder, Young's modulus of elasticity, Poisson's ratio, the coefficient of thermal expansion and geometry.

However, a transient state thermal shock test by which a specimen of suitable size and shape is suddenly subjected to a medium at a different temperature and of given surface heat transfer coefficient is to be preferred since the thermal stress level in addition to the physical properties mentioned in the steady state test are also a function of thermal conductivity, thermal diffusivity and emissivity.

In addition, if the transient state thermal shock test consists of thermal shock by heating, the center of the thermal shock specimen is placed in tension and the surface in compression. Fracture takes place internally and is independent of surface condition. A true measure of the thermal shock resistance is therefore obtained.

Another advantage of subjecting a material to thermal shock on heating is that at the time of maximum stress (i.e., time of fracture) the temperature of the thermal shock specimen is still close to the initial temperature

of the thermal shock test*. If room temperature is selected as the initial temperature of the thermal shock test, the values of the physical properties to be selected in the correlation of the thermal shock test results should correspond to the values obtained at room temperature. This greatly simplifies an investigation of this nature.

The sphere was selected as the most suitable shape of thermal shock specimen. These are relatively easy to manufacture but of greater importance, the sphere offers a convenient shape for the calculation of thermal stresses[5]. This greatly simplifies the problem of correlating physical properties with thermal shock behavior.

Various thermal shock media were investigated. A liquid salt** bath gave poor results due to rapid oxidation of the zirconium carbide at the higher temperatures ($> 400^{o}C$). This oxidation produced an insulating gas mantle between the sample and liquid.

A 180 grit silicon carbide powder fluidized bed proved to be unsuitable since the high temperatures required to fracture the sphere size selected (two-inch diameter) could not be attained.

The thermal shock tests giving best results qualitatively, as well as quantitatively, employed a horizontal three-inch diameter carbon tube furnace. The spheres initially at room temperature were subjected to thermal shock by placing them on a small tantalum metal ring attached to the end of a graphite rod, which was thrust rapidly into the hot zone of the tube furnace. After sufficient time had elapsed for fracture to have occurred the sphere was placed on the bottom of the graphite tube. The furnace was then allowed to cool down after which the sphere was removed and examined to determine whether fracture had occurred and to what extent the sphere was damaged by the thermal shock.

To investigate the qualitative thermal shock behavior as a function of composition, a series of spheres containing 0, 10, 20, 30, 40, 50 volume percent graphite was subjected to a temperature sufficiently high enough to initiate fracture.

To determine the temperature difference required to initiate fracture within the sphere, the approximate temperature required was first determined by subjecting the spheres to temperature intervals of $200^{o}C$. After the approximate temperature was determined, three spheres were subjected to thermal shock near this approximate temperature, at intervals of $25^{o}C$. The temperature required to fracture at least one of the spheres was then taken as the temperature desired.

---

* See Thermal Shock Tests under Experimental Results.
**Hitec, E. I. duPont de Nemours.

Due to the high temperatures required, thermal radiation was the principal mechanism of heat transfer. This introduced emissivity as a variable. A literature survey revealed that no quantitative treatment of thermal shock by radiation existed. This was investigated in detail and a quantitative theory of thermal shock by radiation for simple shapes was developed (See Appendix B). The temperature required to fracture the spheres was then calculated and compared with the experimental value.

In order to investigate the effect of emissivity, the surface of a number of spheres were blackened by painting the surface with a suspension of Dag® colloidal graphite. Upon evaporation of the solvent a thin layer of graphite powder was left on the surface. The temperature required to initiate fracture of these spheres was then determined in the same manner as described above.

D. Experimental Results

1. Coefficient of Thermal Expansion

Table No. III lists the results obtained for the coefficient of thermal expansion perpendicular to the hot pressing direction. Table No. IV lists the results obtained for the high-graphite composites parallel to the direction of hot pressing.

It may be noticed that the coefficient of expansion up to at least forty volume percent graphite is independent of graphite content, porosity or orientation. Composite 60A, however, does indicate a difference in coefficient of expansion perpendicular and parallel to the hot pressing direction.

Figure 6 shows the mean value of the coefficient of thermal expansion perpendicular and parallel to the hot pressing direction for various temperatures as a function of graphite content. Of interest is the decrease in thermal expansion at high graphite content and high temperature. This can be attributed to the difference in temperature dependence of the elastic moduli of the individual phases. Young's modulus of elasticity of the zirconium carbide decreases with temperature whereas Young's modulus of elasticity of the graphite increases with temperature. Since the coefficient of thermal expansion of a composite is a function of the relative stiffness of the components the thermal expansion of the composites with high graphite content at high temperature will start to deviate from the coefficient of thermal expansion of the zirconium carbide towards that of the graphite.

It can be concluded that the coefficient of thermal expansion is not a major variable in this investigation.

2. Young's Modulus of Elasticity, Shear Modulus of Elasticity and Poisson's Ratio

Table No. V lists the results obtained for Young's modulus of elasticity perpendicular and parallel to the hot pressing direction. The effect of the graphite is to decrease Young's modulus of elasticity considerably. Anisotropy may be observed between the Young's moduli of elasticity perpendicular and parallel to the hot pressing direction. The values parallel to the hot pressing direction are lower than those perpendicular to the hot pressing direction. Since the scatter in the values obtained for composite No. OA is well within the experimental error, the degree of anisotropy for zirconium carbide without graphite is negligible.

Comparing the results for Young's modulus of elasticity with the photomicrographs in Figure 1, it may be noticed that the lower Young's modulus of elasticity values are obtained in the direction of flattening of the graphite particles.

Comparing the values of Young's modulus of elasticity given in Table No. V with the graphite and porosity contents of the composites given in Table No. II shows that porosity is also quite effective in lowering Young's modulus of elasticity.

The reduction in Young's modulus of elasticity is apparently independent of graphite particle size.

Table No. VI lists the values obtained for the shear modulus of elasticity and Poisson's ratio. The same general behavior for the shear modulus of elasticity may be observed as for Young's modulus of elasticity. Poisson's ratio to a first approximation is independent of graphite content.

Since the resonant frequency in torsion of the specimen configuration used was close to the upper limit of the frequency response of the equipment, considerable difficulty was experienced obtaining these data. In fact, the shear modulus of elasticity could not be determined for all compositions.

In order to determine the individual effect of the graphite and porosity on Young's modulus of elasticity, various curve fitting programs were compiled for the Univac® electronic computer. Attempts were made to fit the data to equations of various form (polynominals, etc.) containing both graphite content and porosity as independent variables. These attempts proved to be unsuccessful. The approach then taken was to determine separately the effect of graphite content and the effect of porosity.

One of the major difficulties was that the value of Young's modulus of elasticity for zero porosity or zero graphite content was unknown. In order

to determine this value a number of specimens of zirconium carbide of various densities were obtained from the New Products Branch of The Carborundum Company and the value of Young's modulus of elasticity was determined for each. These data together with their porosity are listed in Table No. VII. A general form expressing the porosity dependence of Young's modulus of elasticity was then selected based on equations for the shear and bulk moduli of elasticity for heterogeneous materials suggested by Hashin[12].

The equations for the shear and bulk moduli of elasticity for a two-phase system, as derived by Hashin[12], can be written in the general form:

$$E = E_o \left[1 + \frac{A \left(1 - \frac{E_1}{E_o}\right) c}{1 - B \left\{ \frac{E_1}{E_o} + \left(\frac{E_o - E_1}{E_o}\right) c \right\}} \right] \qquad (10)$$

where $B = (A + 1)$
E = the elastic modulus (shear or bulk) of the composite
E_o = the elastic modulus of the continuous phase
E_1 = the elastic modulus of the dispersed phase
c = the volume fraction of the dispersed phase

Since in the case of porosity E_1 is identical to zero, equation (10) can be written in the general form:

$$E = E_o \left[1 + \frac{AP}{1-(A+1)P} \right] \qquad (11)$$

where P is the volume fraction porosity.

The present writers propose this equation to be applied to express the porosity dependence of the elastic moduli (Young's, shear or bulk) of polycrystalline refractory materials. This equation is based on a mathematical derivation of the elastic moduli of heterogeneous systems on the basis of an actual mechanical model and is to be preferred to the exponential relationship used by Spriggs and Vasilos[13] which is justified only because the data appear to fit the curve.

The statistical evaluation (see Appendix E) of the constants E_o and A in equation (11) involves a matrix inversion and multiplication operation* given by:

* The writers are indebted to Miss S. LeMarie of the Quality Control Branch for deriving the statistical equations used in this investigation.

$$\begin{bmatrix} E_o \\ A \end{bmatrix} = \begin{bmatrix} \sum_1^n \frac{1}{E^2} & \sum_1^n \frac{P}{E(1-P)} \\ \sum_1^n \frac{P}{E(1-P)} & \sum_1^n \frac{P^2}{(1-P)^2} \end{bmatrix}^{-1} \begin{bmatrix} \sum_1^n \frac{1}{E} \\ \sum_1^n \frac{P}{1-P} \end{bmatrix} \quad (12)$$

where n is the number of data points and E is the experimental value of Young's modulus of elasticity.

Applying this equation to the data points obtained yielded the following expression for the porosity dependence of Young's modulus of elasticity of zirconium carbide, given by:

$$E = 68.88 \times 10^6 \left[1 - \frac{4.255P}{1 + 3.255P} \right] \text{psi} \quad (13)$$

In order to illustrate equation (11), the value of E_o and A were also determined for several sets of data obtained by various investigators[14, 15] for the Young's modulus of elasticity of alumina. These results are shown in Table No. XXIV. Of significance is the fact that from these results no significant difference appears to exist between the porosity dependence of Young's modulus of elasticity for hot pressed or sintered bodies. Additional work to investigate this further should be undertaken.

A similar approach was taken to determine the effect of graphite content on Young's modulus of elasticity. Examination of Table No. II reveals that four composites were obtained with nearly zero porosity. On the basis of these values the dependence of Young's modulus of elasticity on graphite content could be determined. Young's modulus of elasticity of graphite was assumed to be 1.50×10^6 psi.

In terms of the Young's moduli of elasticity of zirconium carbide and graphite, equation (10) can be written

$$E = 68.88 \times 10^6 \left[\frac{1 + \frac{A\left(1 - \frac{1.50}{68.88}\right)c}{}}{1 - B\left\{\frac{1.50}{68.88} + \left(\frac{68.88 - 1.50}{68.88}\right)c\right\}} \right] \text{psi} \quad (14)$$

where c is the volume fraction graphite.

The constant A can now be determined statistically by the following equation given by:

$$A = \frac{\sum_{1}^{n}\left[\frac{c}{1-c}\cdot\frac{E}{E-68.88\times10^{6}}+\frac{0.02226}{1-c}\right]}{\sum_{1}^{n}\left[\frac{c}{1-c}\cdot\frac{E}{E-68.88\times10^{6}}+\frac{0.02226}{1-c}\right]^{2}} \qquad (15)$$

Using the data for all composites in evaluating A gave a curve which predicted a considerably higher value for Young's modulus for composite 60A than observed. Similarly, the calculated values for the other three composites were considerably lower than those observed. This suggested a discontinuity in the curve of observed values of Young's modulus as a function of graphite content. This discontinuity was expected since at the volume content graphite for composite 60A, the graphite will tend to become the continuous phase. The value of Young's modulus for composite 60A was, therefore, discarded. The data used for the determination of the constant A were those obtained for composites 25B, 35A and 40B. The value of A for Young's modulus of elasticity perpendicular to the hot pressing direction was found to be -3.497. Similarly, the value of A for Young's modulus of elasticity parallel to the hot pressing direction was found to be -4.688. Substitution of these values into (14) and simplification resulted in the expression for Young's modulus of elasticity ($E_{\perp}$) perpendicular to the hot pressing direction given by:

$$E_{\perp} = 68.88\times10^{6}\left[1-\frac{3.245c}{1+2.317c}\right]\ \text{psi} \qquad (16a)$$

Similarly, for Young's modulus of elasticity parallel to the hot pressing direction ($E_{\parallel}$) is given by:

$$E_{\perp} = 68.88\times10^{6}\left[1-\frac{4.244c}{1+3.339c}\right]\ \text{psi} \qquad (16b)$$

The actual experimental data used to establish the above equations can now be recalculated with a discrepancy of less than two percent which suggests good experimental accuracy in measuring Young's modulus of elasticity and in determining the volume content graphite.

It is rather unfortunate that zero porosity bodies were not obtained for low graphite contents. Equations (16a) and (16b) may not give the true dependence of Young's modulus for low graphite contents; however, they are expected to be quite accurate in the region of the data points used to establish the equation.

Comparing equation (13), which expresses the porosity dependence of Young's modulus of elasticity,with equations (16a) and (16b) the expressions for the dependence of Young's modulus of elasticity on graphite content, shows that to a first approximation the graphite acts like porosity. For this reason a plot of the experimental data of Young's modulus of elasticity against graphite content plus porosity is expected to show considerably less scatter than the same data points plotted against graphite content alone. The experimental data for Young's modulus of elasticity perpendicular and parallel to the hot pressing direction are shown in Figures 7 and 8, respectively, plotted against graphite content. Considerable scatter may be observed. The same data plotted against graphite plus porosity content are shown in Figures 9 and 10. The scatter is reduced considerably.

Similar observations may be made for the shear modulus of elasticity. Figure 11 shows the shear modulus of elasticity as a function of volume content graphite. Figure 12 shows the results for the shear modulus of elasticity as a function of volume content graphite plus porosity.

Since Poisson's ratio remains virtually constant, the experimental results are plotted against volume content graphite only as shown in Figure 13.

Of interest in this investigation is a comparison of the experimental values obtained for Young's modulus of elasticity with the theoretical or semi-empirical equations suggested by various investigators for the elastic moduli of heterogeneous systems[12, 16]. Since the expressions for the elastic moduli derived by Hashin[12] are rather complex, the present writers developed a simpler expression based on a parabolic approximation to the solution for the moduli for very small concentrations as given by Jane M. Dewey[3] and Hashin[12].

This simple expression is derived below.

The equation for the bulk modulus K of a matrix with bulk modulus (B_m) and Poisson's ratio (ν_m) containing a small concentration (c) of spherical particles with bulk modulus K_p is given by:

$$B = B_m \left[1 - \frac{3(1-\nu_m)\left(1 - \frac{B_p}{B_m}\right)}{2(1-2\nu_m) + (1+\nu_m)\frac{B_p}{B_m}} c \right] \quad (c \ll 1) \qquad (17)$$

Similarly, the expression for the shear modulus (G) of a matrix with shear modulus (G_m) and Poisson's ratio (ν_m) containing a dilute concentration (c) of spherical particles with shear modulus (G_p) is given by:

$$G = G_m \left[1 - \frac{15\,(1-\nu_m)\,\left(1-\frac{G_p}{G_m}\right)}{7-5\nu_m+2\,(4-5\nu_m)\,\frac{G_p}{G_m}}\, c \right] \qquad (c << 1) \qquad (18)$$

Both of these expressions can be written in the simple form:

$$B = B_m\,(1-\alpha c) \qquad (19)$$

and

$$G = G_m\,(1-\beta c) \qquad (20)$$

The parabolic approximation for higher values of c is made by writing (19) and (20) of the form:

$$B = B_m\,(1-\alpha c + Ac^2) \qquad (21)$$

and

$$G = G_m\,(1-\beta c + Bc^2) \qquad (22)$$

where A and B are evaluated by setting c = 1, $K = K_p$, and $G = G_p$.

Young's modulus of elasticity (E) can then be calculated from the relation:

$$\frac{3}{E} = \frac{1}{3B} + \frac{1}{G} \qquad (23)$$

Calculating Young's modulus of elasticity for various values of Poisson's ratio of the matrix (ν_m) using (21), (22) and (23), shows that to first approximation for values of (ν_m) from 0.10 to 0.30, Young's modulus of elasticity is independent of Poisson's ratio.

For simplicity, ν_m in (17) and (18) can be set equal to 0.20 and assuming $B_p/B_m = G_p/G_m = E_p/E_m$ yields

$$K = G = E \qquad (24)$$

The equation for Young's modulus of elasticity is then given by:

$$E = E_o \left[1 - \frac{2(1-K)}{1+K}\,\phi + \frac{(1-K)^2}{1+K}\,\phi^2 \right] \qquad (25)$$

where

$$K = E_p/E_m \qquad (26)$$

Since the third term in (25) at small values of volume fraction dispersed phase (ϕ) should be small compared to the second term, the equation will break down when K approaches infinity. An arbitrary upper limit on K, for which equation (25) can be applied, can be set at approximately five.

Expressions similar to that for Young's modulus of elasticity can be written for the shear and bulk moduli of elasticity. These, however, will contain Poisson's ratio as a variable. In general it will be found to be more convenient to evaluate first the constants (α) and (β) in equations (19) and (20) and then to evaluate the constants (A) and (B) in equations (21) and (22).

Figure 14 shows the experimental values of Young's modulus of elasticity of composites 25B, 35A and 40B compared with the equations of Paul[16], Hashin[12], and the simple equation proposed by the present writers. In order to compare the deviations of the various equations from linearity, a straight line based on simple addition of the volume fractions is included.

Figure 15 shows the same equations compared with the equations (16a) and (16b) which express the dependence of Young's modulus perpendicular and parallel to the hot pressing direction calculated from the experimental data.

It may be noticed that considerable difference exists between the various equations proposed.

The best agreement with experiment is found for Hashin's[12] lower bound and the expression proposed by the present writers. Paul's[16] equation shows a large discrepancy between calculated and observed data. Of interest is the fact that all equations accurately predict Young's modulus of elasticity of the system cobalt-tungsten carbide[17, 18, 19, 20, 21] as shown in Figure 16. Here Hashin's lower and upper bounds were omitted because they nearly coincide with the approximate equation. The results of Figure 16 are of special interest since both Paul[16] and Hashin[12] use the system cobalt-tungsten carbide as a justification for their equations.

It does appear that Paul's[16] equation can be applied to a heterogeneous system where the dispersed phase has the higher Young's modulus of elasticity. However, it breaks down when the dispersed phase has a lower Young's modulus of elasticity. Hashin's[12] equations can be applied to all possible heterogeneous systems and it appears from the results of this investigation that Hashin's[12] lower bound will give best agreement with experiment.

The equations for Young's modulus of elasticity as a function of porosity[13] can now be combined with the equations (16a) and (16b) for Young's modulus of elasticity as a function of graphite content to yield Young's modulus of elasticity for the three-phase system zirconium carbide-graphite-porosity.

The equation for Young's modulus of elasticity perpendicular to the hot pressing direction ($E_\perp$) after Hashin[12] is given by:

$$E_\perp = 68.88 \times 10^6 \left[1 - \frac{4.255P}{1 + 3.255\,(P + c)} - \frac{3.245c}{1 + 2.317\,(P + c)} \right] \text{ psi} \quad (27)$$

Similarly, the equation for Young's modulus of elasticity parallel to the hot pressing direction ($E_{||}$) becomes:

$$E_{||} = 68.88 \times 10^6 \left[1 - \frac{4.255P}{1 + 3.255\,(P + c)} - \frac{4.244c}{1 + 3.339\,(P + c)} \right] \text{ psi} \quad (28)$$

The predicted values for Young's modulus of elasticity for the various composites are given in Tables No. VIII and No. IX. Only those composites are listed for which the observed values are considered reliable. It may be noticed that agreement is only fair with relatively large discrepancies for those composites containing higher amounts of porosity. It is interesting, however, that much better agreement may be obtained if the volume contents graphite and porosity are considered relative to the carbide phase only. Equations (27) and (28) are then modified to be:

$$E_\perp = 68.88 \times 10^6 \left[1 - \frac{4.255 \left(\frac{P}{1-c}\right)}{1 + 3.255 \left(\frac{P}{1-c} + \frac{c}{1-P}\right)} - \frac{3.245 \left(\frac{c}{1-P}\right)}{1 + 2.317 \left(\frac{P}{1-c} + \frac{c}{1-P}\right)} \right] \text{ psi} \quad (29)$$

$$E_{||} = 68.88 \times 10^6 \left[1 - \frac{4.255 \left(\frac{P}{1-c}\right)}{1 + 3.255 \left(\frac{P}{1-c} + \frac{c}{1-P}\right)} - \frac{4.244 \left(\frac{c}{1-P}\right)}{1 + 3.339 \left(\frac{P}{1-c} + \frac{c}{1-P}\right)} \right] \text{ psi} \quad (30)$$

where the ratios P/1-c and c/1-P will be referred to as the "reduced" volume fractions porosity and graphite, respectively. The calculated values for the various composites using equations (29) and (30) are included in Tables Nos. VIII and IX.

Excellent agreement is found in the region of the data points used to establish the equations. It may also be noticed that the predicted values of Young's modulus of elasticity for composites containing small volume contents of graphite given in Tables Nos. VIII and IX are somewhat lower than the observed values. This suggests that the slope of the curve of Young's modulus of elasticity against graphite content at small values of graphite content is too steep. It, therefore, appears that at least for Young's modulus of elasticity perpendicular to the hot pressing direction, the curve will nearly coincide with Hashin's[12] lower bound.

Since the equations (29) and (30) contain the sum of the "reduced" volume fractions of graphite and porosity, the experimental results for Young's modulus of elasticity can also be plotted against "reduced" volume fraction graphite plus reduced volume fraction porosity. Figures 17 and 18 give Young's modulus of elasticity perpendicular and parallel to the hot pressing direction plotted against reduced volume content graphite plus porosity. The scatter in data is even smaller as compared with the data plotted against graphite content plus porosity.

Figure 19 shows the experimental values obtained for the shear modulus of elasticity plotted against reduced volume content graphite plus porosity. Included in Figure 19 is the equation for the shear modulus of elasticity for a material containing spherical holes as calculated by MacKenzie[22] with a semi-empirical parabolic approximation suggested by Coble[23]. It may be observed that Coble's[23] equation is identical to the simple equation (22) proposed by the present writers for the shear modulus of a material containing spherical holes.

Figure 20 shows the calculated curves for the shear modulus of elasticity of the system zirconium carbide-graphite from equations suggested by Hashin[12], Paul[16], and the present writers. The zero porosity value of the shear modulus of elasticity was calculated from the zero porosity value of Young's modulus of elasticity and Poisson's ratio to be 29.3×10^6 psi. Since the experimental data of shear modulus of elasticity plotted against reduced volume content graphite plus porosity show the least scatter, the experimental values included in Figure 20 are plotted on this basis.

Measurements were also made for some composites of the temperature dependence of Young's modulus of elasticity (Figure 21). These results did not indicate that the temperature dependence of Young's modulus of elasticity was a major variable affecting the thermal shock resistance of the composites and this aspect was not pursued further. Since Young's and shear modulus of elasticity are strongly affected by the graphite dispersed phase and the porosity, the elastic properties of the composite are major variables in this investigation.

3. Modulus of Rupture

Tables Nos. X and XI list the results obtained for the modulus of rupture at room temperature perpendicular and parallel to the hot pressing direction. The scatter in strength values obtained for a given composition is expressed in terms of the coefficient of variation. It can be concluded that modulus of rupture generally decreases with an increase in graphite content and porosity. Also, the modulus of rupture parallel to the hot pressing direction is considerably lower than perpendicular to the hot pressing direction. Judging by the strength values obtained for composites 20B and 40B it appears that a smaller particle size of graphite results in a higher value of strength.

Figures 22 and 23 show the modulus of rupture perpendicular and parallel to the hot pressing direction plotted against volume content graphite.

Figures 24 and 25 show the same values plotted against volume content graphite plus porosity. As in the case for Young's modulus of elasticity plotting modulus of rupture against volume content graphite plus porosity reduces the scatter obtained compared to the same data plotted against volume content graphite only.

Table No. XII gives the experimental results for modulus of rupture as a function of temperature for various compositions. These results are shown schematically in Figure 26. In general there appears to be a slight increase in strength up to approximately 1200°C, followed by a gradual decrease to 2000°C.

Of interest in the data for modulus of rupture at room temperature is the relatively large scatter obtained for the strength values of dense zirconium carbide compared with the small scatter obtained for the composites containing graphite or higher volume contents porosity. A large scatter in data for zirconium carbide has also been observed by Hall and Watt[24]. In general the degree of scatter in experimental data for strength is a measure of the homogeneity of the material (i.e., distribution of flaws) which strongly affect the value of strength obtained employing specimens of various size. The effect of volume under stress on the experimental value of strength was, therefore, determined for those composites employed in the thermal shock tests. These results are listed in Table No. XIII. The strength value for the dense zirconium carbide (composite OA) is more strongly affected by the volume under stress than the value of strength for composite 50A, containing approximately fifty volume percent graphite. This suggests that the addition of the graphite gives rise to an increase in homogeneity. A homogeneity factor (m) based on Weibull's[25] statistical theory of strength (see Appendix D) is included in Table No. XIII. The use of this homogeneity factor (m) becomes essential in correlating the results of the thermal shock tests with the individual physical properties.

As for Young's modulus of elasticity, an attempt was made to fit the experimental data obtained for modulus of rupture to an appropriate equation. Here too, the value of strength for zero graphite and zero porosity content was unknown. It therefore became rather difficult to draw any conclusions about the effect of the graphite additions on the modulus of rupture of zirconium carbide. A value for the modulus of rupture of zirconium carbide of 30,000 psi was taken as a value of strength that could conceivably be obtained for a low porosity body made in the manner described, for the grain size of the original material and size of test specimen used in the modulus of rupture test.

The general equation selected to which the data were fitted is of similar form as the equation used to express the porosity dependence of Young's modulus of elasticity (11) given by:

$$S_{tb} = 30,000 \left[1 + \frac{Ac}{1-Bc} \right] \text{ psi} \tag{31}$$

where S_{tb} is the modulus of rupture, c is the volume content graphite, A and B are constants which are a function of the mechanical properties of the zirconium carbide and graphite. The relationship between A and B was of specimen used in the strength test. The relationship between A and B was determined by substitution of the strength and graphite content of composite 60A into (31) and solving for the constant B. B can be expressed as a function of A by the equation:

$$B = \alpha + \beta A \tag{32}$$

For the data obtained perpendicular to the hot pressing direction ($B_\perp$) is given by:

$$B_\perp = 1.756 + 1.418 A \tag{33}$$

Similarly, for the data of modulus of rupture parallel ($B_\parallel$) is given by:

$$B_\parallel = 1.756 + 1.281 A \tag{34}$$

The constant A can now be determined statistically from (See Appendix E):

$$A = \frac{\sum_1^n \left[\frac{30,000}{S_{tb_i} - 30,000} + \beta \right] \cdot \left[\frac{c_i}{1 - \alpha c_i} \right]}{\sum_1^n \left\{ \left[\frac{30,000}{S_{tb_i} - 30,000} + \beta \right] \cdot \left[\frac{c_i}{1 - \alpha c_i} \right] \right\}^2} \tag{35}$$

where n is the number of data points and α and β are obtained from (33) and (34). The data used to determine the value of A were those of the dense composites containing less than one-half percent porosity and possessing high strength; namely, composites 25B and 35B. Composites 20B and 40B were excluded because they contain a different particle size of graphite and appear to have a somewhat higher strength. Solving for A and B and substitution into (31) yields the expression for the modulus of rupture perpendicular to the hot pressing direction ($S_{tb_\perp}$) given by:

$$S_{tb_\perp} = 30,000 \left[1 - \frac{9.34c}{1 + 11.46 c} \right] \text{ psi} \tag{36}$$

Similarly, the expression for the modulus of rupture parallel to the hot pressing direction $S_{tb_\parallel}$ is given by:

$$S_{tb_\parallel} = 30,000 \left[1 - \frac{8.03c}{1 + 8.53 c} \right] \text{ psi} \tag{37}$$

Setting c equal to unity yields the extrapolated value for the modulus of rupture of the graphite. These extrapolated values perpendicular and parallel to the hot pressing direction are 7,500 and 4,740 psi, respectively. These values of strength appear somewhat high but are not unreasonable for graphite with a density of 1.915 grams per cubic centimeter, which is the density of the graphite in the composites after hot pressing (See Specimen Preparation).

Since equations (36) and (37) give the values of the modulus of rupture which can be obtained using the method of composite and specimen preparation described previously, the calculated strength values will be referred to as those of a "dense body." Curves representing equations (36) and (37) are included in Figures 22, 23, 24 and 25.

For lack of sufficient data, the porosity dependence of modulus of rupture of zirconium carbide was not investigated. The writers propose that in an investigation of the porosity dependence of polycrystalline refractory materials an equation of the form of (11) be employed.

The decrease in strength of the zirconium carbide on addition of the dispersed phase of graphite can be explained on the basis of the difference in elastic properties between zirconium carbide and graphite. At a given deformation of the composite body, the zirconium carbide and graphite to a first approximation will be subjected to the same strain. However, due to its much lower value of Young's modulus of elasticity the graphite carries a much smaller load than the zirconium carbide than would be expected on the basis of volume fractions. The load, therefore, at least for small volume fraction graphite, is carried principally by the zirconium carbide. As a consequence of the decrease in volume content zirconium carbide bulk strength has been lowered. Since modulus of rupture is strongly affected by the presence of the graphite phase and porosity, the strength of the composites is a major variable in this investigation.

4. Strain at Fracture

The calculated strain at fracture perpendicular and parallel to the hot pressing direction are given in Table No. XIV. Figures 27 and 28 show the calculated values of the strain at fracture perpendicular and parallel to the hot pressing direction, respectively. Since the scatter in data obtained in the experimental values of Young's modulus of elasticity is less than one percent, the standard deviation of the calculated strain at fracture is based on the scatter in data obtained for modulus of rupture only. The calculated experimental strain at fracture may be observed to be approximately constant to forty volume percent graphite and then to rise rapidly. Figures 29 and 30 show the calculated strain at fracture plotted against graphite and porosity content. Due to the relatively constant value of the strain at fracture no decrease in the scatter of data is

obtained. Included also in Figures 27 through 30 are curves of the calculated strain at fracture based on equations (16a) and (16b) giving the dependence of Young's modulus of elasticity and equations (36) and (37) giving the modulus of rupture for a "dense body." Since a discontinuity appears to exist in the experimental data for Young's modulus of elasticity at graphite contents higher than fifty volume percent, the curve of the strain at fracture in Figures 27 through 30 for a "dense body" beyond approximately forty volume percent graphite is based on the actual experimental values obtained.

It is clear that for this specimen size the strain at fracture differs appreciably from the strain at fracture of the zirconium carbide only at volume contents of graphite in excess of fifty volume percent.

Of extreme interest is the strain at fracture as a function of specimen size. For the small specimen size listed in Table No. XIII, the strain at fracture of the zirconium carbide is nearly double the value of the strain at fracture for the composite (50A) containing approximately fifty volume percent. For the regular size specimen (three by one-half by one-quarter inches) the strain at fracture of the zirconium carbide plus fifty volume percent graphite is approximately twenty-five percent higher than for the zirconium carbide (composite OA), whereas in the thermal shock specimens the strain at fracture for zirconium carbide containing fifty volume percent graphite is nearly fifty percent higher than the strain at fracture of the zirconium carbide only. (See "Correlation of Thermal Shock Tests with Physical Properties" Section). This will affect thermal shock resistance appreciably. In this discussion the reasonable assumption is made that Young's modulus of elasticity is independent of specimen size.

The decrease in Young's modulus of elasticity and the slight increase in modulus of rupture with temperature results in an increase in the strain at fracture with temperature. No significant difference exists in the temperature dependence of the strain at fracture of zirconium carbide or zirconium carbide containing graphite.

No clear-cut conclusion can be drawn concerning the effect of porosity on the strain at fracture. In general the effect of porosity on the mechanical properties of a polycrystalline material is to affect strength more strongly than Young's modulus of elasticity, resulting in a decrease in the strain at fracture. This may be observed in composites OA and OB where composite OB having a porosity content of 8.8 percent has a strain at fracture appreciably lower than composite OA which contains only 4.4 percent porosity. In the presence of the graphite, however, the effect of porosity is not clear. This may be seen by comparing the calculated values of the strain at fracture in Table No. XIV with the composition listed in Table No. II. It is clear that the strain at fracture is a major variable in this investigation.

5. Elastic Energy Stored at Fracture

Table No. XV lists the calculated values of the elastic energy stored at fracture in a body subjected to a uniaxial stress equal to the strength (modulus of rupture). The effect of the graphite is to lower the elastic energy stored at fracture by a factor of approximately two or three. Porosity also lowers appreciably the elastic energy stored at fracture. The values for the elastic energy stored at fracture in graphite are based on the extrapolated values for the modulus of rupture of the "dense bodies" of zirconium carbide-graphite composites (See Modulus of Rupture Section). Young's modulus of elasticity was assumed to be 1.50×10^6 psi. Similar values of the elastic energy stored at fracture in industrial types of graphite can be calculated. It is interesting to note that due to its low value of Young's modulus of elasticity, graphite has a higher value of the elastic energy stored at fracture than the high strength zirconium carbide.

Figures 31 and 32 show the calculated values of the elastic energy stored at fracture perpendicular and parallel to the hot pressing direction, respectively, plotted as a function of graphite content. Included also are curves of the elastic energy stored at fracture for "dense bodies" calculated from equations (16a) and (16b) for Young's modulus of elasticity for non-porous composites and equations (36) and (37) for modulus of rupture for "dense bodies." As discussed under "Strain at Fracture" the plotted curves beyond forty volume percent graphite are based on the actual experimental values obtained. It may be observed that the curves representing the elastic energy stored at fracture for the "dense bodies" initially decrease with increase in graphite content to reach a minimum at approximately thirty-five volume percent graphite and then to increase to a value for graphite which exceeds the value for the dense zirconium carbide. It can be concluded that the elastic energy stored at fracture is a major variable to be taken into consideration in this investigation.

6. Impact Resistance

Table No. XVI lists the relative impact resistance for a number of composites compared with the relative energy stored at fracture. The effect of the graphite is to lower the impact resistance. The correlation between the energy stored at fracture and impact resistance can be considered as being fair only. The impact resistance in this investigation is of no consequence but was measured for the correlation with the elastic energy stored at fracture.

7. Thermal Diffusivity

Table No. XVII lists the experimental values of the thermal diffusivity as a function of volume content graphite and temperature. The effect of graphite is to increase the thermal diffusivity. In particular, at 25°C, due to

the low value of specific heat of the graphite[26], the value of thermal diffusivity for the composite containing fifty volume percent graphite is more than doubled. Thermal diffusivity decreases with an increase in temperature. Due to the strong temperature dependence of the specific heat of the graphite[26] in the temperature region employed, diffusivity of the composites containing graphite is more strongly dependent on temperature than that for zirconium carbide only.

Figure 33 shows the experimental values for thermal diffusivity as a function of graphite content. Since thermal diffusivity appears to depend approximately linearly on graphite content, straight lines representing the thermal diffusivity at a given temperature were drawn through the experimental points.

In order to illustrate the strong temperature dependence of the thermal diffusivity on graphite content, Figure 34 shows the heating curves obtained at 25°C for the zirconium carbide and zirconium carbide containing fifty volume percent graphite.

Since the thermal shock tests consisted of subjecting spheres to thermal shock on heating, whereby fracture occurs at temperatures close to the initial temperatures of the specimen (See Appendices B and C), thermal diffusivity was not determined at higher temperatures.

8. Thermal Conductivity

Table No. XVIII lists the compositions and values of thermal conductivity measured by the absolute method. The graphite content listed refers to the volume content when prepared. The porosity content was calculated from the bulk density and the densities of the individual components. The slight reduction in graphite content due to the presence of the porosity was neglected. The experimental values of thermal conductivity were corrected for porosity by assuming that the reduction in thermal conductivity was directly proportional to the volume content porosity.

From the values listed in Table No. XVIII, it can be concluded that the thermal conductivity increases with graphite content and decreases with temperature.

Table No. XIX lists the values of thermal conductivity calculated from the experimental values of thermal diffusivity and the known values of density and specific heat of zirconium carbide[27] and graphite[26] by means of the relation:

$$K = a \left[\rho_1 \; C_{p1} \; \phi_1 + \rho_2 \; C_{p2} \; (1-\phi_1) \right] \qquad (38)$$

where K is the thermal conductivity of the composite
a is the thermal diffusivity
ρ is the density
C_p is the specific heat
ϕ is the volume fraction

The subscript 1 and 2 refer to the volume content graphite and zirconium carbide, respectively.

The values of thermal conductivity calculated from the thermal diffusivity appear to be somewhat lower than the values of thermal conductivity measured directly. Similar observations were made by Mrosowski et al[31].

Figure 35 shows the general behavior of the thermal conductivity as a function of graphite content and temperature for the thermal conductivity measured directly, as well as the thermal conductivity calculated from the thermal diffusivity. For the purpose of clarity, the experimental points were omitted.

Since thermal conductivity changes rapidly with graphite content, it is clear that thermal conductivity is a major variable in this investigation. However, since the thermal conductivity is a function of the thermal properties of the components rather than the elastic properties, thermal conductivity is a major variable only insofar as it becomes essential in evaluating the thermal shock test results.

9. Emissivity (Absorptivity)

Table No. XX lists the experimental values for the total normal absorptivity of the composites at room temperature for incandescent radiation. Absorptivity increases with graphite content. Also, the high porosity bodies have a higher absorptivity than the low porosity bodies. This can be attributed to a larger surface area of the porous bodies as compared to the non-porous bodies.

Of interest is the fact that the absorptivity increases more rapidly with graphite content than would be expected on a volume fraction basis. Sieber[28,29] gives a value for the absorptivity of graphite at room temperature for radiation from 3000°K equal to 0.80. The higher values obtained experimentally were probably due to an increase in roughness of the surface. Due to the large difference in hardness between the zirconium carbide and graphite, smooth surfaces could not be obtained.

Figure 36 shows the experimental absorptivity values plotted against graphite content. Two parallel lines are drawn approximately through the values

for zero and ten percent porosity. It can be concluded that under conditions of heat transfer by radiation the additions of graphite to the zirconium carbide will decrease thermal shock resistance. From the results obtained it can be concluded that emissivity is also a major variable in this investigation and should strongly affect the results of the thermal shock test.

10. Thermal Shock Tests

Figure 37 shows a series of spheres of zirconium carbide containing 0, 10, 20, 30, 40 and 50 volume percent graphite subjected to a temperature of 2000°C. The sphere composed entirely of zirconium carbide had fractured catastrophically whereas the sphere containing graphite at first sight appeared to be unharmed. Closer examination, however, revealed that some cracks could be detected on the surface of the sphere containing ten percent graphite.

Figure 38 shows the same spheres dissected to investigate the extent of any internal damage. All spheres may be seen to contain internal cracks. These are probably the most significant results obtained in this investigation. The presence of the graphite dispersion not only affects the physical properties of the zirconium carbide which affect the nucleation of fracture by thermal shock but, in addition, strongly affects the fracture behavior after fracture by thermal shock has been initiated.

Table No. XXI lists the temperatures required to initiate fracture in the spheres of the zirconium carbide, the blackened zirconium carbide and zirconium carbide containing fifty volume percent graphite. It may be noticed that blackening of the surface appreciably lowered the temperature required to initiate fracture. Similarly, the effect of the graphite is to increase the temperature required to initiate fracture.

An attempt was made to investigate the fracture behavior of graphite using two-inch diameter spheres and the same thermal shock test. This proved to be unsuccessful. Due to the high thermal conductivity and strain at fracture, these spheres could not be fractured.

The effect of graphite particle size on the fracture behavior of the composites was also investigated. Spheres containing fifty volume percent graphite with particle size 170-200 mesh, minus 325 mesh, and Thermax® were subjected to thermal shock at 1800°C. The spheres with graphite particle size 170-200 mesh and minus 325 mesh showed internal cracks only. However, the spheres containing Thermax® fractured catastrophically.

Since a relationship exists between the thermal diffusivity and the time of maximum stress, an attempt was made to measure the time from the start of the thermal shock test (i.e., the time at which the sphere enters the

hot zone) to the time at which fracture occurred. This could only be detected for the zirconium carbide because of the catastrophic nature of fracture. This period of time was found to be so short (approximately five seconds) that no absolute value could be obtained without appreciable experimental error.

With the knowledge of the temperature required to initiate fracture, the temperature level of the thermal shock test can now be calculated.

The rise in temperature of the surface of the sphere from the start of the thermal shock test until the time the stress has reached ninety-five percent of its final value $T(b, t_{0.95})$, to a good approximation, is given by (See Appendix C):

$$T(b, t_{0.95}) = 0.707 \frac{q_o b}{K} \tag{39}$$

where b is the sphere radius
K is the thermal conductivity
q_o is the initial rate of heat flux to which the sphere is subjected at the start of the thermal shock and equal:

$$q_o = \rho \epsilon \quad T_{max}^4 \tag{40}$$

where ρ is the Stefan-Boltzmann constant ($\rho = 1.37 \times 10^{-12}$ cal. deg^{-4}. cm^{-2}. sec^{-1})
ϵ is the absorptivity
T_{max} is the minimum temperature required to initiate fracture, or the maximum temperature to which the sphere can be subjected without fracture.

Substitution of the appropriate physical properties listed in Table No. XXII yields a value for the rise in surface temperature equal to approximately 130°C. Assuming room temperature to be 25°C the actual temperature of the surface at the time of fracture is approximately 155°C.

Similarly, at the time of fracture the temperature of the surface of the spheres containing fifty volume percent graphite can be calculated to be approximately 200°C.

11. Correlation of Physical Properties with Temperature Required to Initiate Fracture

With a quantitative knowledge of the physical properties affecting thermal shock resistance the temperature required to initiate fracture can now be calculated and compared with the values obtained experimentally.

The expression for the maximum temperature (T_{max}) to which a sphere can be subjected under conditions of heat transfer by radiation (See Appendix B) is given by:

$$T_{max} = \left[\frac{5\, S_{ts}\, (1-\upsilon)\, K \left(\frac{1}{\epsilon_1} + \frac{1}{\epsilon_2} - 1 \right)}{\alpha E \rho\, b} \right]^{1/4} \qquad (41)$$

where S_{ts} is the tensile strength of a sphere under condition of thermal shock on heating
υ is Poisson's ratio
K is the thermal conductivity
α is the coefficient of thermal expansion
E is Young's modulus of elasticity
ϵ_1 is the absorptivity of the specimen
ϵ_2 is the emissivity of the enclosure
ρ is the Stefan-Boltzmann constant
b is the sphere radius

Combining Weibull's[25] statistical theory of strength and the theory of maximum stress for biaxial and triaxial stress states, expressions can be derived from which the value of tensile strength (S_{ts}) to be substituted into the equation for T_{max} (41) can be calculated from the modulus of rupture obtained by three-point loading (See Appendix D).

For failure to occur due to the radial stress the expression for S_{ts} is given by:

$$S_{ts} = S_{tb} \left[\frac{V_{bar}}{V_{sphere}} \right]^{\frac{1}{m}} \left[\frac{1}{3(m+1)^2\, B(\frac{3}{2}, m+1} \right]^{\frac{1}{m}} \qquad (42)$$

where S_{tb} is the modulus of rupture
V_{bar} is the volume of the modulus of rupture bar between the loading points
V_{sphere} is the volume of the sphere
m is the homogeneity factor
$B(\frac{3}{2}, m+1)$ is the Beta function of 3/2 and $m+1$

For failure to occur due to the tangential stresses the expression for S_{ts} is given by:

$$S_{ts} = S_{tb} \left[\frac{V_{bar}}{V_{sphere}} \right]^{\frac{1}{m}} \left[\frac{4}{3\sqrt{2}\,(m+1)^2\, B(\frac{3}{2}, m+1} \right]^{\frac{1}{m}} \qquad (43)$$

Table No. XXII lists the physical properties required for the calculation of T_{max} by means of equation (41).

Substitution for V_{bar}, V_{sphere} and m into (42) yields, for fracture to occur by the radial stress in the zirconium carbide,

$$S_{ts} = 0.336\ S_{tb} \tag{44}$$

and for the zirconium carbide containing fifty volume percent graphite

$$S_{ts} = 0.623\ S_{tb} \tag{45}$$

Similarly, for fracture to occur due to the tangential stress, we obtain for zirconium carbide

$$S_{ts} = 0.605\ S_{tb} \tag{46}$$

and for zirconium carbide containing fifty volume percent graphite

$$S_{ts} = 0.686\ S_{tb} \tag{47}$$

The calculated values of (S_{ts}) by means of equations (44), (45), (46) and (47) are included in Table No. XXII. It may be noticed that due to greater volume under stress under conditions of thermal shock as compared with the volume under stress under three-point loading, the reduction in strength is appreciable. Due to the difference in the homogeneity factor, the reduction in strength for the zirconium carbide is greater than the reduction in strength for the zirconium carbide containing fifty volume percent graphite.

For the selection of the other physical properties, a porosity of five percent was assumed, which is the value usually obtained in the hot pressed spheres. The mechanical and thermal properties, therefore, correspond to those obtained for composites OA and 50A. The values of thermal conductivity were obtained from the straight line in Figure 35 for the thermal conductivity at 50°C, measured by the absolute method. The value for thermal conductivity for five percent porosity was calculated on the assumption that the decrease in thermal conductivity was proportional to the volume fraction pores.

The emissivity of the blackened zirconium carbide was taken as unity. The emissivity of the enclosure (carbon tube) was assumed to be equal to 0.95. Comparison between the experimental and calculated values of T_{max} shows that excellent agreement exists. It can be argued that from the point of view of crack propagation, fracture will occur under the influence of the tangential stresses rather than the radial stresses. (See Appendix D). This is supported by the fact that agreement between the calculated and experimental values of T_{max} on the basis of fracture due to the tangential stresses is considerably better than for fracture to occur by the radial stresses.

12. Other Materials

a. Silicon Carbide-Graphite

In order to investigate a heterogeneous system composed of a carbide and graphite free of porosity, a number of composites of the system silicon carbide-graphite were prepared containing various volume contents graphite. The method of preparation consisted of siliconizing cold pressed carbon-graphite bodies. Due to experimental difficulty, bodies containing more than thirty-five volume percent graphite could not be manufactured. Suitable test bars of similar size as employed in the system zirconium carbide-graphite were cut by means of a diamond saw and their mechanical properties determined.

Table No. XXIII lists the modulus of rupture, Young's modulus of elasticity, the calculated strain at fracture, and the calculated elastic energy per unit volume stored at fracture. The general behavior of these mechanical properties are similar to those of the "dense bodies" of zirconium carbide-graphite. Both modulus of rupture and Young's modulus of elasticity decrease with increase in graphite content. The strain at fracture remains approximately constant, whereas the elastic energy at fracture decreases in a similar manner as for zirconium carbide-graphite.

No physical properties other than those listed in Table No. XXIII were determined for this system.

b. Alumina-Zirconia

The observations by Boronin et al[30] that alumina containing a dispersed phase of zirconia possessed better thermal shock resistance than alumina itself, suggested that these observations were similar to those in this investigation. Zirconia has a Young's modulus of elasticity of approximately 20×10^6 psi[15]. Dense alumina has a Young's modulus of elasticity of approximately 60×10^6 psi[14]. The system alumina-zirconia, therefore, represents an oxide analogy to the zirconium carbide-graphite or silicon carbide-graphite systems. In the system alumina-zirconia, however, the ratio of elastic modulus of the dispersed to the continuous phase is higher than in the carbide-graphite system.

Table No. XXIV lists the mechanical properties of a number of bodies of alumina-zirconia. For the bodies containing similar volume fractions of porosity, the strength as well as Young's modulus of elasticity decrease with increase in zirconia content. The rapid decrease in Young's modulus of elasticity is remarkable. This may be attributed to a lack of bonding between the alumina and zirconia. The strain at fracture increases with zirconia content whereas the elastic energy stored at fracture decreases with zirconia content. The decrease in elastic energy stored at fracture, however, is small.

An attempt was made to hot press a number of spheres to be used as thermal shock specimens. This proved to be unsuccessful as many of the spheres contained small surface cracks. Therefore, a number of cylinders measuring approximately one and one-quarter inches in diameter by one and one-quarter inches high containing twenty-five weight percent zirconia were cold pressed and subsequently sintered for two hours at 1600°C. These were subjected to thermal shock by plunging them from room temperature into a liquid salt bath*. Figure 39 shows the results obtained. The alumina cylinders fractured when subjected to a salt bath temperature of 400°C. The alumina-zirconia, however, had to be subjected to 500°C before fracture occurred. This increase in thermal shock resistance may be attributed to an increase in the strain at fracture.

Most significant, however, is the observation that the alumina cylinders fractured catastrophically, whereas the alumina-zirconia cylinders exhibited slight fracture only. These observations are similar to those made on the system zirconium carbide-graphite.

13. Additional Thermal Stress Calculations

As part of this project, complete calculations were made of the maximum thermal stresses occurring in a sphere subjected to thermal shock in a medium with constant surface heat transfer coefficient (See Appendix C). In addition to the maximum stresses the time of maximum stress and the temperature of the sphere at the time of maximum stress were also calculated. The values obtained for the maximum thermal stresses agreed with those given by Crandall and Ging[5]. Of interest, however, in these calculations was the result that at the time of maximum stress for values of Biot's modulus, usually found in thermal shock tests, the sphere is still close to its initial temperature. To a first approximation the value of the physical properties to be selected for the prediction of the temperature difference required to initiate fracture should correspond to the initial temperature of the sphere in the thermal shock test. Crandall and Ging[5], in their thermal shock analysis of spherical shapes, based their prediction of the temperature difference required to nucleate fracture in sphere on the value of the physical properties which correspond to a temperature approximately midway between the initial and final temperature of the thermal shock test. Good agreement was obtained for thermal shock on heating. On cooling, however, the calculated values exceeded the observed value by several hundred percent. Since the disagreement could be due to the selection of the physical properties at a temperature which differed from the temperature at which fracture occurred, the writers decided to recalculate the predictions of Crandall and Ging[5]. The complete calculations are given in Appendix C. A graphical method was developed to simplify the calculation of the predicted temperature difference required for fracture. Table No. XXXIII (included in

*Hitec, E. I. duPont de Nemours.

Appendix C) gives the observed and calculated values for both heating and cooling in a liquid salt bath. Excellent agreement is found.

Crandall and Ging[5] also calculated the temperature difference required for fracture by heating in air. However, at the temperatures employed heat transfer occurred principally by means of thermal radiation. This was treated successfully in Appendix B.

E. Discussion

Although the significance of the results for each of the physical properties obtained were discussed under Experimental Results, a general discussion of the overall thermal shock resistance of the zirconium carbide-graphite and other heterogeneous systems is in order.

In order to simplify the discussion of the physical properties affecting the thermal shock resistance of the system zirconium carbide-graphite, the experimental results obtained are shown in Figure 40 on a normalized basis setting the property values of the zirconium carbide equal to unity. All curves shown refer to the mean of the values of the physical properties obtained at room temperature between the directions perpendicular and parallel to the hot pressing direction. In addition, the curves correspond to the physical properties obtained for the "dense bodies" only, containing graphite with particle size 70-100 mesh. The physical properties shown are the coefficient of thermal expansion (α), Young's modulus of elasticity (E), Poisson's ratio (υ), modulus of rupture (S_t), and thermal conductivity (k). In order to avoid crowding of the diagram, thermal diffusivity and emissivity were omitted. Thermal diffusivity was omitted since in the thermal shock test used in this investigation, thermal diffusivity affects the time of maximum stress (i.e., time of fracture), but not the stress level. Similarly, the emissivity was omitted since it only affects thermal shock resistance when thermal radiation is the principal mechanism of heat transfer.

Included also in Figure 40 are the thermal stress resistance parameters

$$\frac{S_t\,(1-\upsilon)}{\alpha E} \quad \text{and} \quad \frac{S_t\,(1-\upsilon)\,k}{\alpha E} \tag{48}$$

hereafter referred to as the thermal stress resistance parameters R^I and R^{II}, respectively. For good thermal shock resistance high values of R^I and R^{II} are desired. The thermal stress parameter R^{III}, which is similar to R^{II} with the thermal conductivity replaced by thermal diffusivity, is omitted to avoid confusion*.

* These thermal stress resistance parameters in the literature[30] are usually referred to as R, R^1 and R^{11}. However, the introduction of additional parameters (this discussion and Appendix B) necessitates numbering them consecutively.

The advantage of adding the dispersed phase of graphite to the carbide becomes evident immediately. The factor R^I decreases slightly with graphite content then increases again to become equal to the value for the zirconium carbide at a graphite content of approximately thirty-five percent and with further increases in graphite rises rapidly. Therefore, for a composite body of zirconium carbide-graphite with a volume content of graphite greater than about thirty-five percent, the thermal shock resistance exceeds that of the zirconium carbide itself. Due to the increase in thermal conductivity with graphite content the factor R^{II} increases much more rapidly than the factor R^I. At a volume content of graphite of approximately fifty percent the thermal shock resistance is about double that of the pure zirconium carbide.

If another material was selected for the continuous phase with a thermal conductivity greater than zirconium carbide then the increase of thermal conductivity would be less rapid and the curve for R^{II} would be closer to the curve for R^I. In the case of equal thermal conductivities for the continuous and dispersed phases, these curves would coincide. The advantages of using graphite rather than porosity are as follows.

The initial parts of the curves of Young's modulus of elasticity (E), and modulus of rupture (S_t), up to approximately twenty volume percent graphite would be about the same as for porosity; however, beyond this volume content, where the strength of the graphite begins to play a role, the value of strength of the composite falls much less rapidly than Young's modulus of elasticity, resulting in an increase in the strain at fracture (i.e., a rise in the curve for R^I). This would not have been the case if the dispersed phase had consisted of porosity. In addition, since porosity (below radiation temperature) lowers thermal conductivity appreciable, the curve for thermal conductivity (k) would always be less than unity. As a result the curve for R^{II} will also be less than unity and actually fall below the curve for R^I.

From the point of view of nucleation of fracture by thermal shock the advantage of adding graphite to the zirconium carbide is to increase thermal conductivity and the extensibility (i.e., strain at fracture) resulting in increases in the factors R^I and R^{II}. Thermal diffusivity is also increased, especially at lower temperatures, so that in those cases where the magnitude of the thermal stresses are a function of the thermal diffusivity an increase in thermal shock resistance is obtained. A curve for R^{III}, if included in Figure 40, would rise very rapidly with graphite content.

These conclusions probably can be extended to other heterogeneous systems as well, and if the mechanical and thermal properties of the two phases are similar to the properties of the zirconium carbide and graphite the thermal shock behavior will be almost identical.

In order to extend the qualitative and quantitative results obtained in this investigation for the system zirconium carbide-graphite to other systems, it should be noted the mechanical properties of a composite to a good approximation will be a function only of the mechanical properties of the components and will not be affected by differences in thermal properties of the components. Similarly, the thermal properties of the composite will be a function of the thermal properties of the components only and will be unaffected by the mechanical properties. Only the coefficient of thermal expansion of the composite, if regarded as a thermal property, will be a function of the elastic properties of the individual components.

In drawing conclusions from Figure 40, it should be kept in mind that the results shown are valid only for specimens measuring three by one-half by one-quarter inches. Due to the increase in effective homogeneity with graphite content and therefore a subsequent decrease in strength dependence of the volume under stress, the strength for larger specimen size will decrease less strongly with graphite content, with the result that the curves for R^I and R^{II} will rise much more rapidly with graphite content than shown in Figure 40.

Similarly, due to the slight increase in strength with temperature accompanied by a decrease in Young's modulus of elasticity the effect of an increase in temperature is to raise the curves for R^I and R^{II}.

From the limited results obtained for the composites containing graphite with smaller particle size, the curves for R^I and R^{II} will also be raised slightly by decreasing the graphite particle size.

The introduction of emissivity as a material variable affecting thermal shock resistance and the development of a quantitative theory of thermal shock by radiation (See Appendix B) can be regarded as a major contribution to the quantitative understanding of the thermal shock behavior of ceramic materials.

It appears to the writers that emissivity due to the mathematical complexity of heat transfer by radiation has heretofore been neglected. In many laboratories, use is made of thermal shock tests in which radiation is the principal mechanism of heat transfer. The interpretation of the results of these tests, however, usually exclude emissivity as a variable. In particular, the results of thermal cycling tests of small modulus of rupture bars,which often employ temperatures in excess of 1000°C, should be treated with some caution. As shown in Appendix B, the emissivity plays as important a role in thermal shock resistance as the physical properties usually considered in thermal shock theory. As an example, the improved thermal shock resistance of molybdenum reinforced alumina ceramics[34], as compared to the alumina itself, can at least in part be attributed to a decrease in emissivity since molybdenum has a considerably lower emissivity than alumina. The presence of the metal phase at the surface has lowered the overall emissivity of the composite

material with the result that in comparative thermal shock tests employing identical temperature levels the thermal shock for the molybdenum reinforced alumina is less severe than the thermal shock for the alumina.

The quantitative correlation between the individual physical properties and the temperature required to nucleate fracture in the zirconium carbide-graphite composites is excellent. The procedure followed to calculate the tensile strength under condition of thermal shock from the bending strength under three-point loading might appear to be not strictly valid as it is based on two theories of strength (See Appendix D). However, although additional work is required to test the method employed, on the basis of the agreement obtained it does appear that it might be applicable to other thermal shock situations as well.

The hypothesis advanced in Appendix D, that fracture of the thermal shock specimen occurs under the influence of the tangential thermal stresses only, is substantiated by the fact that considerably better agreement with experiment is obtained for the temperature required for fracture on the basis of failure under tangential stress than for failure to occur under the radial stress. It does appear that a similar approach might also be employed in other situations of biaxial or triaxial stress states.

One question which immediately arises in an investigation of the thermal shock resistance of heterogeneous materials is on what basis the physical properties for the prediction of the thermal resistance should be selected. Should the physical properties be those of the bulk material (i.e., the overall physical properties), or should the properties of the individual phases be taken into account? From the excellent agreement between theory and experiment in the prediction of the temperature required to initiate fracture in the sphere composed of zirconium carbide containing fifty volume percent graphite, it appears that the physical properties should be selected on the basis of the overall physical properties of the composite. It becomes clear when one realizes that the thermal stresses at any point within the body are due to the interaction of all other points within the body. As a consequence, any point in the body "sees" the material at some distance away as a homogeneous material, with physical properties those of the composite. The magnitude of the stress, therefore, is determined by the bulk properties. The stress can be compared with the bulk strength in order to determine whether fracture will occur. Of course, the distribution of the stress in the composite on a microscopic scale will be extremely complex. As a result, the nucleation of fracture in a composite material may differ considerably from the nucleation of fracture in a single-phase material. This, however, should not affect the criteria of failure that fracture will occur when the bulk stress equals bulk strength.

The recalculation of the results of Crandall and Ging[5] obtaining good agreement with experiment also suggests that extreme care should be taken in interpreting thermal shock results and also in the selection of the values of the

physical properties in predicting the thermal shock behavior of ceramic materials. As shown in Appendix B, for low values of Biot's modulus a spherical thermal shock specimen at the time of maximum stress is still close to the initial temperature of the thermal shock test. This will also be true of small bodies of arbitrary shape subjected to relatively mild thermal shock. For example, in thermal cycling of small modulus of rupture bars between room temperature and a higher temperature Biot's modulus is considerably less than unity. Therefore, thermal shock on heating occurs at room temperature and on cooling at the high temperature. Due to the lower strength and thermal conductivity at the higher temperature, thermal shock on cooling is considerably more severe than thermal shock on heating. A thermal cycling test, therefore, consists principally of a thermal shock test by means of cooling. Due to the differences in temperature dependence of strength and thermal conductivity between materials, the results obtained from a thermal cycling test for the relative thermal shock resistance between two materials cannot be extended to the relative thermal shock resistance of the same materials on heating. A thermal cycling test may be a convenient test to investigate the fatigue strength of materials under condition of thermal shock but does not lend itself to investigate the nucleation of fracture by thermal shock.

Probably the most significant observation made in this investigation is the considerable difference in fracture behavior of the pure carbide body compared to that of the carbide-graphite body. In all cases where fracture occurred, the bodies composed entirely of carbide phase failed catastrophically while the carbide-graphite bodies fractured internally but remained intact.

The material factors which affect the fracture behavior of brittle materials under condition of thermal shock consist of:

(1) The elastic energy stored at fracture, which provides the driving face for crack propagation.

(2) The effective surface energy required to create the new fracture surfaces.

(3) Possible dispersion and attenuation of the stress waves accompanying the propagating crack and of any other stress waves nucleated at the time of fracture.

The total elastic energy stored in a brittle material subjected to thermal shock at the time of fracture will depend on the material properties of the body, on size and shape and on the temperature and stress distribution. Unless simple body geometry is chosen and many simplifying assumptions are made, the calculation of the stored elastic energy becomes mathematically prohibitive.

The general procedure to be followed is to find the temperature distribution within the body at the time of fracture. From this temperature distribution, the distribution of the thermal stresses can be determined. Equating

the maximum tensile strength of the material to the maximum thermal stress, the thermal stresses can then be expressed as a function of strength. From the stress distribution, the elastic energy stored at fracture is then calculated. Following this procedure for a sphere of radius (b), subjected to thermal shock on heating by radiation (See Appendix B), the elastic energy (W) stored at fracture to a good approximation can be calculated to be (See Appendix A):

$$W = \frac{4\pi}{7} \frac{S_t^2 (1-\nu) b^3}{E} \tag{49}$$

where S_t is the tensile strength under condition of thermal shock
ν is Poisson's ratio
E is Young's modulus of elasticity

It can be seen that the elastic energy is proportional to the volume of the sphere, to the square of the tensile strength, to the factor $(1-\nu)$, and inversely to Young's modulus of elasticity. Therefore, the elastic energy stored at fracture is a function of geometry, body size and a material factor (Q) given by:

$$Q = \frac{S_t^2 (1-\nu)}{E} \tag{50}$$

Figure 40 shows the value of (Q) for the system zirconium carbide-graphite as a function of graphite content. As a consequence of the decrease in the elastic energy stored at fracture the impact strength of the composite will also be lowered. This was verified experimentally with a moderate degree of correlation.

Since in thermal shock theory, it is customary to discuss thermal shock resistance in terms of thermal stress or thermal shock resistance parameters, a thermal shock damage resistance parameter" (R^V), the reciprocal of equation (50), is introduced to be employed in the design of brittle material for severe thermal shock situation given by:

$$R^V = \frac{E}{S_t^2 (1-\nu)} \tag{51}$$

Figure 40 shows the dependence of the parameter R^V for the system zirconium carbide-graphite as a function of graphite content. A sharp maximum may be noted in the curve at a volume content of graphite of approximately thirty volume percent. It is of interest to note that the graphite content in "GRB" silicon carbide, developed by the New Products Branch of The Carborundum Company, is of approximately this value.

When fracture occurs, the elastic energy stored at fracture is transformed into various other forms of energy among which are acoustic, kinetic and the effective surface energy (γ_{eff}) required for the creation of the new crack surfaces. The effective surface energy required for crack propagation can consist of one of the following energies(33):

(1) The thermodynamic surface free energy. This will be of the order of 10^3 dynes per cm.

(2) The energy dissipated in anelastic deformation at the tip of the propagating crack will be of the order of 10^4 dynes per cm.

(3) Energy dissipated in plastic deformation of a thin surface layer on the newly formed crack surfaces. This energy for ductile metals may be of the order of 10^5 - 10^6 dynes per cm and may reach a value as high as 10^8 dynes per cm. However, for brittle materials this mechanism of energy dissipation is of little consequence.

(4) Energy dissipated in creating electrical charges on the fresh crack surfaces. This becomes significant only in the case of electrical insulators and may reach a value of 10^4 dynes per cm.

In case of fracture by thermal shock, which takes place non-catastrophically, a major part of the energy stored at fracture must have been absorbed by the propagation of the nucleated cracks. The criterion, therefore, for failure by thermal shock to be non-catastrophic is that the area over which the cracks will propagate calculated from the elastic energy stored at fracture divided by the effective surface energy required for crack propagation is less than the cross-sectional area of the body multiplied by the number of cracks nucleated at the time of fracture. If this condition is not satisfied, additional energy is still available even after the cracks have traversed the body completely. This additional energy will probably be imparted to the fragments in the form of kinetic energy with the result that the body will fracture explosively, scattering the fragments over a wide area. It is of interest to note that the energy required for crack propagation under conditions of thermal shock is supplied by the elastic energy stored in the body only, and is not supplied by any external body force. The energy criteria for crack nucleation and propagation under conditions of thermal shock, therefore, are similar to the energy criteria for crack nucleation and propagation of a body mechanically loaded under conditions of "fixed grips"(53).

By setting the area over which the cracks will propagate, multiplied by the effective surface energy required for crack propagation, equal to the elastic energy stored at fracture, assuming the body to be stress free after

the cracks have propagated, an additional thermal shock damage resistance parameter (R^{VI}) can be derived, given by:

$$R^{VI} = \frac{\gamma_{eff} E}{S_t^2 (1-\nu)} \qquad (52)$$

From the above discussion, it follows that in the selection of materials for severe thermal shock applications where even in the best materials available it is expected that fracture will be nucleated, a material should be selected with high values of the thermal shock damage resistance parameters R^V and R^{VI}. This will require high values of (γ_{eff}), low values of strength, and high values for Young's modulus of elasticity and Poisson's ratio. It may be noted that the requirements for low strength, high Young's modulus of elasticity, and Poisson's ratio for a low degree of damage is directly opposite the requirements of high strength, low Young's modulus of elasticity and low Poisson's ratio necessary to avoid fracture by thermal shock.

For brittle ceramic materials, the value of (γ_{eff}) will be relatively low and will not differ greatly from one material to another. The thermal shock damage resistance factor R^V then becomes of prime importance. One method by which R^V can be increased is by deliberately introducing porosity in the material. Porous materials are often quoted as having good thermal shock resistance (all other factors such as grain size kept constant). Their apparent thermal shock resistance, however, should be attributed to the non-catastrophic nature of fracture rather than to the lack of nucleation of fracture.

For anelastic materials, or those materials possessing some degree of ductility, the thermal shock damage resistance parameter R^{VI} becomes the principal design criterion.

The significant increase in the thermal shock resistance for cycling from room temperature to 2200°F of molybdenum fiber reinforced alumina[34] with respect to the pure alumina, can in part be attributed to a substantial increase in the value of γ_{eff}. Due to the plastic deformation accompanying crack propagation through the metal phase, insufficient elastic energy is available for fracture to take place catastrophically.

The considerable change in fracture behavior of the zirconium carbide on addition of the dispersed phase of graphite can also be attributed to a change in the thermal shock damage resistance factors R^V and R^{VI}. Due to the decrease in the elastic energy stored at fracture with graphite content, the factor R^V can be increased by a factor of two or three. However, since an appreciable difference in the fracture behavior is effected by a relatively small volume fraction graphite, it appears that the effective surface energy required for crack propagation also must make a considerable contribution. The effective

surface energy for crack propagation in graphite, therefore, must be considerably higher than for zirconium carbide. Humenik and Whalen[35] report a surface energy for zirconium carbide of 800 + 250 dynes per centimeter. These same investigators report a surface energy of graphite of 1590 dynes per centimeter or nearly twice the value for zirconium carbide. Another mechanism of energy dissipation in crack propagation is probably the considerable degree of anelasticity displayed by graphite[36], and also due to possible plastic deformation within each individual graphite grain.

The effect of the elastic energy available for crack propagation and the effective surface energy required for crack propagation will explain many observations of the relative difference in fracture behavior of brittle materials. The limited observations on the system alumina-zirconia, however, suggest that another possible mechanism also may be operative. From the mechanical property data in Table No. XXIV, it is clear that no great change occurs in the elastic energy stored at fracture. In addition, alumina and zirconia are both brittle materials. Their values of the effective surface energy required for crack propagation will be relatively low and will not differ appreciably. The change in fracture behavior, therefore, cannot be explained on the basis of the thermal shock damage resistance parameters R^{V} and R^{VI}.

A possible explanation is offered by the fact that the material systems under investigation are composed of materials with different elastic properties. The presence of a dispersed phase of a material with low values of elastic moduli contained within a continuous matrix of a material of high elastic modulus introduces elastic discontinuities within the body. These elastic discontinuities give rise to scattering and dispersion of elastic waves propagating through the body. Therefore, any stress field accompanying the propagating crack and any shock waves nucleated at the time of fracture will be attenuated rapidly. The propagating crack, therefore, will be retarded. Less kinetic energy is imparted to the segments on either side of the crack with the result that the damage will be reduced appreciably. The problem then becomes one of the effect of velocity of crack propagation on the "degree of damage."

Semi-quantitative measurements were made of the attenuation of ultrasonic sound waves traveling through the carbide-graphite bodies. Sound waves with frequency of one megacycle per second appeared to travel through the composites unhindered. At five megacycles per second, however, the attenuation increased rapidly with graphite content. However, too little is known of crack propagation even in single-phase materials to allow a quantitative treatment of the subject. Considerable work, however, was done on the attenuation of sound waves in heterogeneous systems[37], which showed that the attenuation for a given frequency is a function of the relative differences in elastic properties and of the particle size. With additional knowledge of crack propagation, the particle size of the dispersed phase may be selected to maximize the attenuation.

In any material all three possible mechanisms discussed above will probably be operative. It is unfortunate that the results of the thermal shock tests on two-inch diameter graphite spheres proved to be negative. Since the elastic energy stored in graphite is of approximately the same value as for zirconium carbide, observations on the fracture behavior of the graphite would establish the relative importance of the elastic energy stored at fracture. Apparently no observations have appeared in the literature of the thermal shock behavior of graphite interpreted in terms of the "degree of damage" resulting on thermal shock. Additional work is necessary to separate the contribution of each mechanism.

A favorite theory often met in discussions of crack propagation is that pores or other discontinuities within the body can act as crack arresters thereby reducing the degree of damage. A close look at this hypothesis will reveal that it will be quite valid for two-dimensional bodies,such as a plate which contains a hole. However, for three-dimensional bodies containing isolated pores the cracks will simply travel around the pore. Due to the stress concentration effect in the vicinity of the pore, the crack may even be accelerated. In a three-dimensional body a discontinuity can only arrest a crack if it is continuous throughout the body and lies in the plane of the propagating crack. This is illustrated by the ductile behavior of single crystals of magnesium oxides investigated by Johnston et al[38].

In summary, it can be concluded that for the design of brittle materials for application of severe thermal shock where fracture cannot be avoided, the proper selection of a suitable material should be based on a low elastic energy stored at fracture, high effective surface energy required for crack propagation, and possible high attenuation for ultrasonic waves.

One additional aspect to be considered in the design for thermal shock is that, regardless of the material, a particular geometry or structure can be selected which minimizes the total elastic energy contained in the structure due to the presence of thermal stresses. This approach will also reduce the damage upon failure by thermal shock with the result that the structure will retain its shape and for many applications will still be in a serviceable condition even after thermal shock failure.

F. Conclusions

Material factors affecting the thermal shock behavior of an elastically heterogeneous system were investigated using the system zirconium carbide-graphite as a model system. On the basis of the experimental results the following principal conclusions can be drawn:

1. The thermal shock behavior of a two-phase system composed of a high Young's modulus of elasticity continuous phase containing a low Young's modulus dispersed phase is characterized by a "low degree of damage." This low degree of damage is due to a decrease in the elastic energy stored at fracture, a possible increase in the effective surface energy required for crack propagation and possibly dispersion of stress waves accompanying the propagating crack at the elastic discontinuities which exist at the boundaries between the two phases.

   Suitable "thermal shock damage resistance parameters" were derived which establish the design criteria for the selection of materials for application of severe thermal shock where even in the most thermal shock resistant materials it is expected that fracture will occur. As a consequence of the decrease in elastic energy stored at fracture, the presence of the low Young's modulus dispersed phase also lowers impact resistance.

2. The effect of the dispersed phase with low Young's modulus of elasticity on the material properties which affect the nucleation of thermal stress fracture is to decrease strength and Young's modulus of elasticity. The coefficient of thermal expansion and Poisson's ratio to a first approximation are independent of volume content of the dispersed phase. The simultaneous decrease in strength and Young's modulus of elasticity, however, occurs in such a manner that at a sufficiently high volume fraction dispersed phase the strain at fracture (i.e., extensibility) is improved considerably.

   The effect of the low Young's modulus dispersed phase is also to increase the effective homogeneity which considerably decreases the scatter in experimental data for strength. This also reduces the dependence of strength on body size.

3. The relative change in thermal conductivity and thermal diffusivity will depend on the properties of the individual phases. For the system zirconium carbide-graphite the effect of the graphite is to increase thermal conductivity, as well as thermal diffusivity.

4. Emissivity (absorptivity) was introduced as a variable affecting thermal shock resistance. For a composite body, emissivity will be a function of the emissivities of the components and surface condition.

   A quantitative theory for thermal shock for heating by thermal radiation was developed. Excellent agreement between theory and experiment was found.

5. A procedure was developed by which the tensile strength in a sphere subjected to thermal shock on heating can be computed from the bending strength of a rectangular bar subjected to three-point loading. It was hypothesized that fracture would be nucleated by the tangential stress system rather than the radial stress system. Agreement between the experimental values of the temperature required to nucleate fracture is considerably better on the basis of the probability of fracture by the tangential stress system than by the radial stress system.

6. The predictions of Crandall and Ging[5] for the thermal shock behavior of alumina spheres were recalculated. Excellent agreement was found with experiments for both thermal shock by heating and by cooling.

G. Recommendations

On the basis of the observations made in this investigation, the following recommendations are made for future work:

1. In order to obtain further qualitative and quantitative understanding of the "degree of damage" to be incurred by thermal shock, additional work is suggested on the fracture behavior of single-phase and multi-phase systems.

2. Theoretical and experimental work is suggested on the dynamics of crack propagation through multi-phase materials.

3. Further experimental work is suggested on the elastic moduli of other two-phase and other multi-phase systems, to compare the results obtained with theoretical and semi-empirical equations in the literature.

4. Considerable work is suggested to investigate the effect of emissivity (absorptivity) on the thermal shock resistance of brittle materials. The effect of surface condition and methods of lowering emissivity can be investigated.

REFERENCES:

(1) Shulze, C. E., et al, "Development and Evaluation of Materials for High Temperature Applications," WADC-TR-59-10 (March, 1959). See also U. S. Patents No. 2,888,355, 2,854,736 and 2,872,327.

(2) Shaffer, P. T. B., Hasselman, D. P. H., Chaberski, A. Z., "Factors Affecting Thermal Shock Resistance of Polyphase Ceramic Bodies," The Carborundum Company, WADD-TR-60-749, February 1961.

(3) Dewey, Jane M., "The Elastic Constants of Materials Loaded with Non-Rigid Fillers," J.Appl. Physics, 18, 578 (1949).

(4) Goodier, J. H., "Concentration of Stress Around Spherical and Cylindrical Inclusions and Flaws," J. Appl. Mech., 1, 39-44 (1933).

(5) Crandall, W. B. and Ging, J., "Thermal Shock Analysis of Spherical Shapes," J. Amer. Ceram. Soc., 38, 44 (1955).

(6) Hasselman, D. P. H., "Tables for the Computation of the Shear and Young's Modulus of Elasticity from the Resonant Frequencies of Rectangular Prisms," The Carborundum Company, Marketing Development Department (1962).

(7) Shaffer, P. T. B., "Compact Apparatus for High Temperature Modulus of Rupture Measurements," Rev. Sci. Inst., 32, 794 (1961).

(8) Francl, J. and Kingery, W. D., "Thermal Conductivity: IV, Apparatus for Determining Thermal Conductivity by a Comparative Method," J. Amer. Ceram. Soc., 37, 80 (1954).

(9) Heikes, R. R., and Ure, R. W., Jr., "Thermoelectricity," Interscience Publishers (1961), page 288.

(10) Carslaw, H. S. and Jeager, J. C., "Conduction of Heat in Solids," Oxford, at the Clarendon Press (1959), page 239.

(11) "Handbook of Chemistry and Physics," 36th Ed., Chemical Rubber Publishing Company (1954-55), page 2692.

(12) Hashin, Z., "The Elastic Moduli of Heterogeneous Materials," J. Appl. Mech., (To be published).

(13) Spriggs, R. M. and Vasilos, T., "Effect of Grain Size and Porosity on Transverse Bend Strength and Elastic Modulus of Hot Pressed Alumina and Magnesia," presented at the Sixty-Third Annual Meeting, The American Ceramic Society, Toronto, 1961.

(14) Chang, D. H., "Elastic and Anelastic Properties of Fine-Grained Polycrystalline Alumina at Elevated Temperatures," M.S. Thesis, College of Ceramics, Alfred University (1961).

(15) Lang, S. M., "Properties of High-Temperature Ceramics and Cermets - Elasticity and Density at Room Temperature," NBS Monograph 6, 1960.

(16) Paul, B., "Prediction of Elastic Constants of Multiphase Materials," Trans. A.I.M.E., 218, 37-41 (1960).

(17) Schwarzkopf, P. and Kieffer, R., "Cemented Carbides," page 138. MacMillan (1960).

(18) Noronov, F. F. and Balashov, D. B., "The Adiabatic Moduli of Elasticity in Sintered Tungsten Carbide Cutting Alloys," The Physics of Metals and Metallography, 9, 127 (1960).

(19) Nishimatsui, C. and Gurland, J., Trans. Amer. Soc. Metals, 52, 469 (1960).

(20) Lardner, E. and McGregor, J., J. Inst. Metals, 80, 369 (1951-52).

(21) Köster, W. and Rauschner, W., Z. Metallkunde, 39, 111 (1948).

(22) MacKenzie, J. K., "The Elastic Constants of a Solid Containing Spherical Holes," Proc. Phys. Soc. (London), B63, 2-11 (1950).

(23) Coble, R. L., "Effect of Microstructure on the Mechanical Properties of Ceramic Materials," Ceramic Engineering Processes, John Wiley and Sons, New York, 1957, (11 213-218).

(24) Hall, A. R., and Watt, W., "The Bend Strength of Sintered Zirconium Carbide," Technical Note No. MET. 137, Royal Aircraft Establishment, Farnborough, Hants, Dec. 1950.

(25) Weibull, W., "Statistical Theory of Strength of Materials," Ing. Vetenskap-Akad. Hand., 151, (1939).

(26) "Preliminary Report on the Thermodynamic Properties of Selected Light-Element Compounds," NBS Report 6645, January 1960.

(27) Mezaki, R., "Heat Contents of Inorganic Substances at High Temperature," Thesis, University of Wisconsin, Department of Chemistry, 1961.

(28) Sieber, Z. Tech. Phys., 130-135 (1951).

(29) McAdams, "Transmission of Heat," 3rd Ed., McGraw Hill, 1954, page 62.

(30) Boronin, N. I., Gorodetskit, V. S., and Levchuk, V. V., Ognenpory, 24, 272-76 (1959).

(31) Mrozowski, et al, University of Buffalo Progress Report No. 13, Sept. 30, 1961.

(32) Kingery, W. D., "Factors Affecting Thermal Stress Resistance of Ceramic Materials," J. Amer. Ceram. Soc., 38, 3 (1955).

(33) Gilman, J. J., "Fracture," Edited by B. L. Averbach, et al, Wiley (1959), page 193.

(34) Tinklepaugh, G. R., "Metal Reinforcement and Cladding of Cermets and Ceramics," "Cermets", edited by Tinklepaugh, G. R. and Crandall, W. B., Reinhold, 1960 (page 170).

(35) Humenik, K. Jr., and Whalen, T. J., "Physicochemical Aspects of Cermets," ibid, page 6.

(36) Mrozowski, S., et al, "Investigation of Elastic and Thermal Properties of Carbon-Base Bodies," WADC TR-58-360, Part I, December 1958.

(37) Einspruch, N. G., Witterholt, E. J. and Truell, R., J. Appl. Phys., 31, 806 (1960).

(38) Johnston, T. L., Stokes, R. J., and Lee, C. H., "The Relationship Between Plastic Flow and the Fracture Mechanism in Magnesium Oxide Single Crystals," Fourth Technical Report, Feb. 1959, Honeywell Research Center, Hoskins, Minnesota.

(39) Timoshenko, S., and Goodier, J. N., "Theory of Elasticity," 2nd Ed., McGraw Hill (1951), page 148.

(40) Heilman, R. H., "Surface Heat Transmission," Mech. Eng., 51, 355 (1929).

(41) McAdams, W. H., "Heat Transmission," 3rd Ed., McGraw Hill (1954), pp. 55 and 62.

(42) Boley, B. A., and Weiner, G. H., "Theory of Thermal Stresses," John Wiley (1960), Chapter 9.

(43) Hottel, H. C., "Radiant Heat Transmission," Mech. Eng., 52, 699 (1930).

(44) Crandall, W. B., Private Communication.

(45) Goldsmith, A., Waterman, T. E., and Hirscham, H. J., "Handbook of Thermophysical Properties of Solid Materials," MacMillan, New York (1961), Volume 3, page 35.

(46) Powell, R. W., Proc. Phys. Soc., 46, 659 (1934). See also Metals Handbook, 8th Ed., Am. Soc. for Metals, page 1209.

(47) Cody, C. D., Abeles, B., and Beers, P. S., "Thermal Diffusivity of Armco Iron," Trans. A.I.M.E., 221, 25 (1961).

(48) Heisler, M. P., "Temperature Charts for Induction and Constant Temperature Heating," Trans. A.I.M.E., 69, 227-236 (1947).

(49) Salmassy, O.K., Bodine, E. G., Duckworth, W. H., and Manning, G.K., "Behavior of Brittle-State Materials," WADC-TR-53-50, Parts I and II (June 1955).

(50) Davidenkov, N. N., Stavrogin, A. N., and Petrova, N. A., "Strength Criteria in Brittle Fracture," Doklady Akad. Nauk., SSSR, 99, 73-75 (1954).

(51) Scarborough, G. B., "Numerical Mathematical Analysis," Oxford (1950) pp. 463-9.

(52) Moore, E. H., No title, Bull. Amer. Math. Soc., 26 (1920).

(53) Bueckner, H. F., "The Propagation of Cracks and the Energy of Elastic Deformation," Trans. of A.S.M.E., 80, 1225 (1958).

TABLE NO. I

Table for the Calculation of Thermal Diffusivity From the Transient Temperature at the Center of a Sphere

(Values of N/2 for Values of $a\alpha_1$ from 0 to π)

$a\alpha_1$	0	1	2	3	4	5	6	7	8	9
.0	-	.4935	.4984	.5000	.5000	.5001	.5001	.5002	.5003	.5004
.1	.5005	.5006	.5007	.5008	.5010	.5011	.5013	.5014	.5016	.5018
.2	.5020	.5022	.5024	.5026	.5029	.5031	.5034	.5037	.5039	.5042
.3	.5045	.5048	.5051	.5054	.5058	.5062	.5065	.5069	.5073	.5077
.4	.5081	.5085	.5089	.5093	.5098	.5102	.5107	.5112	.5116	.5121
.5	.5126	.5132	.5137	.5142	.5148	.5153	.5159	.5165	.5171	.5177
.6	.5183	.5189	.5196	.5202	.5209	.5215	.5222	.5229	.5236	.5243
.7	.5250	.5288	.5265	.5273	.5281	.5288	.5296	.5304	.5313	.5321
.8	.5329	.5338	.5346	.5355	.5364	.5373	.5382	.5391	.5401	.5410
.9	.5420	.5429	.5439	.5449	.5459	.5470	.5480	.5490	.5501	.5512
1.0	.5524	.5533	.5545	.5556	.5567	.5579	.5590	.5602	.5614	.5626
1.1	.5638	.5650	.5662	.5675	.5688	.5700	.5713	.5726	.5740	.5753
1.2	.5766	.5780	.5794	.5807	.5821	.5836	.5850	.5864	.5879	.5894
1.3	.5908	.5923	.5939	.5954	.5969	.5985	.6001	.6016	.6032	.6049
1.4	.6065	.6081	.6098	.6115	.6131	.6149	.6166	.6183	.6201	.6218
1.5	.6236	.6254	.6272	.6290	.6309	.6327	.6346	.6365	.6384	.6403
1.6	.6422	.6442	.6461	.6481	.6501	.6521	.6541	.6562	.6582	.6603
1.7	.6624	.6645	.6666	.6687	.6709	.6731	.6752	.6774	.6797	.6819
1.8	.6841	.6864	.6887	.6910	.6933	.6956	.6979	.7003	.7027	.7050
1.9	.7074	.7098	.7123	.7147	.7172	.7197	.7221	.7247	.7272	.7297

TABLE NO. I (cont'd)

Table for the Calculation of Thermal Diffusivity From the Transient Temperature at the Center of a Sphere

(Values of N/2 for Values of $a\alpha_1$ from 0 to π)

$a\alpha_1$	0	1	2	3	4	5	6	7	8	9
2.0	.7323	.7348	.7374	.7400	.7426	.7452	.7478	.7505	.7531	.7558
2.1	.7585	.7612	.7639	.7666	.7694	.7721	.7749	.7776	.7804	.7832
2.2	.7860	.7888	.7916	.7945	.7973	.8002	.8030	.8060	.8088	.8116
2.3	.8145	.8174	.8203	.8232	.8262	.8291	.8320	.8349	.8379	.8408
2.4	.8437	.8467	.8496	.8525	.8555	.8584	.8614	.8643	.8672	.8702
2.5	.8731	.8760	.8789	.8818	.8847	.8876	.8905	.8934	.8962	.8991
2.6	.9019	.9047	.9076	.9104	.9131	.9159	.9186	.9213	.9240	.9267
2.7	.9294	.9320	.9346	.9372	.9397	.9422	.9447	.9472	.9496	.9519
2.8	.9543	.9566	.9580	.9611	.9633	.9654	.9675	.9695	.9715	.9734
2.9	.9753	.9772	.9789	.9807	.9823	.9839	.9854	.9869	.9883	.9896
3.0	.9908	.9921	.9932	.9942	.9952	.9961	.9968	.9976	.9982	.9987
3.1	.9992	.9995	.9998	.9999	.9999					

TABLE NO. II

Volume Analysis and Bulk Density

Composite	Zirconium Carbide (vol. %)	Graphite (vol. %)	Porosity (%)	Bulk Density (g/cc)
OA	95.6	0	4.4	6.40
OB	91.2	0	8.8	6.11
5A	91.8	5.8	2.4	6.26
10A	88.0	9.8	2.2	6.09
10B	86.5	10.2	3.3	6.00
15A	77.8	14.1	8.1	5.48
15B	77.3	14.0	8.7	5.45
20A*	73.6	16.0	9.6	5.29
20B**	77.5	18.6	3.9	5.60
25A	64.5	24.6	10.9	4.79
25B	74.6	25.4	~0.0	5.46
30A	61.5	22.2	16.3	4.55
30B	70.2	26.3	3.5	5.20
35A	65.6	34.4	~0.0	5.16
35B	65.2	34.3	0.5	5.03
40A	51.3	40.8	7.9	4.23
40B**	58.9	41.1	~0.0	4.83
45A	56.4	43.3	0.3	4.61
50A	46.6	49.0	4.4	4.06
55A	50.2	46.2	3.6	4.25
60A	43.0	57.0	~0.0	3.97

* Due to lack of definition between individual phases, volume analysis unreliable.

** Graphite particle size 100-140 mesh. All others 70-100 mesh.

TABLE NO. III

Coefficient of Thermal Expansion Perpendicular to Hot Pressing Direction $^{o}C^{-1}$ (x 10^{6})

Composite	Mean Coefficient of Expansion from 25°C to						
	200°C	400°C	600°C	800°C	1000°C	1200°C	1350°C
OB	5.73	6.55	6.94	7.16	7.33	7.45	7.49
10A	5.85	6.42	6.82	7.05	7.26	7.35	7.37
20A	5.65	6.43	6.89	7.08	7.26	7.37	7.41
30A	5.64	6.37	6.89	7.21	7.40	7.48	7.51
40A	5.63	6.46	6.86	7.13	7.29	7.42	7.46
55A	5.46	6.27	6.76	6.98	7.14	7.23	7.24
60A	5.46	6.15	6.57	6.84	7.04	7.11	7.11

TABLE NO. IV

Coefficient of Thermal Expansion Parallel to Hot Pressing Direction $^{o}C^{-1}$ (x 10^{6})

Composite	Mean Coefficient of Expansion from 25°C to						
	200°C	400°C	600°C	800°C	1000°C	1200°C	1350°C
40A	5.94	6.53	6.98	7.21	7.34	7.43	7.47
60A	5.92	6.56	6.96	7.15	7.25	7.14	6.94

TABLE NO. V

Young's Modulus of Elasticity

Composite	Young's Modulus Perpendicular to Hot Pressing Direction psi (x 10^{-6})	Young's Modulus Parallel to Hot Pressing Direction psi (x 10^{-6})
OA	57.57	56.92
OB	44.76*	-
5A	52.61	51.55
10A	48.80	47.78
10B	46.40	46.28
15A	34.33	-
15B	34.60	31.89
20A	33.29	-
20B	36.77	32.82
25A	19.90	20.68*
25B	33.72	29.56
30A	17.38	14.27
30B	28.91	24.76
35A	25.83	21.72
35B	25.53	21.39
40A	13.16	-
40B	21.54	17.78
45A	18.10	14.30
50A	13.00	9.98
55A	13.30	9.60
60A	11.28	7.49

* These values are considered unreliable.

TABLE NO. VI

Shear Modulus of Elasticity* and Poisson's Ratio

Composite	Shear Modulus psi (x 10^{-6})	Poisson's Ratio
OA	24.66	0.167
5A	22.52	0.168
10B	19.79	0.170
15A	14.64	0.180
20A	14.39	0.166
25A	8.54	0.165
30A	7.33	0.186
40A	5.53	0.185

*Bars cut perpendicular to hot pressing direction.

TABLE NO. VII

Additional Young's Modulus of Elasticity Values for Zirconium Carbide as a Function of Porosity

Composite	Porosity (%)	Young's Modulus of Elasticity psi (x 10^{-6})
OC	3.4	59.52
OD	3.5	58.75
OE	9.0	49.39
OF	15.1	39.00

TABLE NO. VIII

Calculated and Observed Values of Young's Modulus of Elasticity for the System Zirconium Carbide-Graphite-Porosity Perpendicular to Hot Pressing Direction

Composite	Calculated by Hashin's Equation psi (x 10^{-6})	Calculated by Modified Hashin Equation psi (x 10^{-6})	Observed psi (x 10^{-6})
OA	57.60	57.60	57.57
OB	48.83	48.83	-
OC	59.90	59.90	59.52
OD	59.67	59.67	58.75
OE	48.49	48.49	49.39
OF	38.52	38.52	39.00
5A	52.43	52.14	52.61
10A	47.11	46.49	48.80
10B	44.80	43.81	46.40
15A	34.29	31.88	34.33
15B	33.71	31.17	34.60
20B	34.96	33.22	36.77
25A	23.89	19.70	19.90
25B	33.14	33.14	33.72
30A	21.45	16.50	17.38
30B	28.90	27.87	28.91
35A	26.15	26.15	25.83
35B	25.75	25.43	25.53
40A	17.08	12.91	13.16
40B	21.83	21.83	21.54
45A	20.34	20.20	18.10
50A	15.22	12.31	13.00

TABLE NO. IX

Calculated and Observed Values of Young's Modulus of Elasticity for the System Zirconium Carbide-Graphite-Porosity Parallel to Hot Pressing Direction

Composite	Calculated by Hashin's Equation psi (x 10^{-6})	Calculated by Modified Hashin Equation psi (x 10^{-6})	Observed psi (x 10^{-6})
OA	57.60	57.60	56.92
OB	48.83	48.83	-
OC	59.90	59.90	59.52
OD	59.67	59.67	58.75
OE	48.49	48.49	49.39
OF	38.52	38.52	39.00
5A	50.01	49.68	51.55
10A	43.81	42.21	47.78
10B	41.61	40.63	46.28
15A	31.42	29.10	-
15B	30.93	28.47	31.89
20B	31.23	29.65	32.82
25A	21.15	13.26	-
25B	28.70	28.70	29.65
30A	19.29	14.74	14.27
30B	25.13	23.62	24.76
35A	22.08	22.08	21.72
35B	21.82	21.50	21.39
40A	14.51	11.03	-
40B	18.23	18.23	17.78
45A	16.95	16.83	14.30
50A	12.69	10.35	9.98

TABLE NO. X

Modulus of Rupture at Room Temperature
Perpendicular to Hot Pressing Direction

Composite	Number of Samples	Modulus of Rupture (psi)	Coefficient of Variation (%)
OA	6	24,330	24.6
OB	4	15,390	5.8
5A	12	13,720	5.0
10A	10	15,640	6.3
10B	8	17,810	13.5
15A	12	10,980	7.1
15B	11	11,920	4.9
20A	9	14,410	8.0
20B	13	13,680	5.0
25A	7	7,670	3.8
25B	12	11,910	6.8
30A	5	7,430	6.6
30B	12	11,010	4.8
35A	10	7,290	4.7
35B	11	10,490	4.6
40A	5	6,400	6.7
40B	11	10,110	5.0
45A	5	7,520	7.2
50A	11	7,240	8.9
55A	9	7,200	7.9
60A	10	8,830	6.1

TABLE NO. XI

Modulus of Rupture at Room Temperature Parallel to Hot Pressing Direction

Composite	Number of Samples	Modulus of Rupture (psi)	Coefficient of Variation (%)
OA	7	23,700	19.9
OB	-	-	-
5A	11	12,600	13.6
10A	-	-	-
10B	-	-	-
15A	-	-	-
15B	9	10,760	5.7
20A	-	-	-
20B	12	11,870	7.9
25A	9	7,500	4.6
25B	13	10,520	6.8
30A	10	5,480	6.1
30B	12	9,170	6.5
35A	10	6,410	6.1
35B	12	8,910	3.6
40A	-	-	-
40B	12	8,620	4.7
45A	5	6,970	6.3
50A	6	6,060	5.9
55A	10	5,540	7.4
60A	10	6,570	6.4

TABLE NO. XII

Modulus of Rupture at Higher Temperatures*

Composite	Temperature (°C)	Modulus of Rupture (psi)	Number of Specimens
OA**	800	24,960	1
	1000	16,760	1
	1200	31,760	1
	1400	26,020	1
	1600	25,320	1
	1800	23,500	1
	2000	17,600	1
OB	1250	8,300	1
	1500	3,800	1
	1750	5,140	1
	2000	2,345	3
10A	880	23,100	1
	1000	19,470	3
	1150	10,300	1
	1250	5,170	2
	1750	5,970	2
	2000	5,170	1
20A	1000	16,400	1
	1250	11,250	2
	1500	10,760	2
	1750	9,250	1
	2000	4,050	1
25A	1000	8,550	1
	1500	5,430	1
	2000	3,375	1
30A	1000	7,250	1
	1500	6,200	1
	2000	4,580	1
40A	1000	8,380	1
	1250	6,850	1
	1500	6,770	1
	2000	5,230	1

* All bars cut perpendicular to hot pressing direction.
** Data obtained since WADD 60-749, Part I.

TABLE NO. XII (cont'd)

Modulus of Rupture at Higher Temperatures*

Composite	Temperature (°C)	Modulus of Rupture (psi)	Number of Specimens
40B**	800	10,550	1
	1000	7,840	1
	1200	7,770	1
	1400	8,200	1
	1600	9,530	1
	1800	8,690	1
	2000	7,290	1
50A	1000	12,525	1
	1500	8,070	1
	2000	4,550	1

* All bars cut perpendicular to hot pressing direction.
** Data obtained since WADD 60-749, Part I.

TABLE NO. XIII

Effect of Volume Under Stress on Modulus of Rupture*

Composite	Modulus of Rupture Volume Under Stress (in. ^{3}) 2-1/2 x 1/2 x 1/4	Modulus of Rupture Volume Under Stress (in. ^{3}) 3/4 x 1/4 x 1/7	Homogeneity Factor (m)
OA	24,330	46,000	~ 4
50A	7,240	9,020	~ 11

* Bars cut perpendicular to hot pressing direction.

TABLE NO. XIV

Calculated Strain at Fracture

Composite	Strain at Fracture* ($\times 10^4$) Perpendicular to Hot Pressing Direction	Strain at Fracture* ($\times 10^4$) Parallel to Hot Pressing Direction
OA	4.22	4.14
OB	3.44	-
5A	2.61	2.45
10A	3.20	-
10B	3.84	-
15A	3.20	-
15B	3.45	3.37
20A	4.32	-
20B	3.72	3.61
25A	3.85	3.62
25B	3.54	3.56
30A	4.28	3.85
30B	3.81	3.70
35A	2.82	2.94
35B	4.11	4.16
40A	4.87	-
40B	4.70	4.85
45A	4.15	4.87
50A	5.57	6.08
55A	5.42	5.76
60A	7.83	8.78

* Same coefficients of variation as for modulus of rupture.

TABLE NO. XV

Elastic Energy Per Unit Volume Stored at Fracture (lb. in. $^{-2}$)

Composite	Perpendicular to Hot Pressing Direction	Parallel to Hot Pressing Direction
OA	5.13	4.91
OB	2.65	-
5A	1.79	1.54
10A	2.50	-
10B	3.42	-
15A	1.76	-
15B	2.06	1.81
20A	3.11	-
20B	2.54	2.14
25A	1.48	1.36
25B	2.11	1.87
30A	1.59	1.05
30B	2.10	1.70
35A	1.03	0.94
35B	2.16	1.85
40A	1.56	-
40B	2.38	2.09
45A	1.56	1.70
50A	2.02	1.84
55A	1.95	1.60
60A	3.46	2.88
Graphite*	18.8	7.50

* Based on extrapolated values of modulus of rupture.

TABLE NO. XVI

Relative Impact Resistance*

Composite	Relative Impact Resistance*	Relative Energy Stored at Fracture
OB	1.00	1.00
10B	1.12	1.29
20A	0.69	1.17
25A	0.56	0.56
30A	0.62	0.60
40A	0.62	0.59
50A	1.01	0.76

* Bars cut perpendicular to hot pressing direction.

TABLE NO. XVII

Thermal Diffusivity ($cm^2 \cdot sec^{-1}$)

Graphite (vol. %)	25°C	200°C	275°C	335°C
0	0.153	0.120	0.096	0.087
10	0.193	0.139	0.107	0.098
20	0.217	0.143	0.115	0.105
30	0.292	0.152	0.126	0.103
40	0.318	0.162	0.140	0.118
50	0.325	0.167	0.138	0.119

TABLE NO. XVIII

Thermal Conductivity
(cal. deg. $^{-1}$ cm. $^{-1}$ sec. $^{-1}$)

Graphite (vol. %)	Porosity (%)	As Measured		Corrected for Porosity	
		50°C	150°C	50°C	150°C
0	10.4	0.0878	.062	0.098	.069
10	8.3	0.111	.079	0.121	.087
20	8.8	0.129	.094	0.142	.104
30	4.3	0.148	.088	0.155	.109
40	10.0	0.143	.117	0.158	.130
50	6.6	0.124	.123	0.133	.132
60	8.7	0.173	.124	0.189	.136

TABLE NO. XIX

Thermal Conductivity Calculated from Thermal Diffusivity (cal. deg. $^{-1}$ cm. $^{-1}$ sec. $^{-1}$)

Graphite (vol. %)	25°C	200°C	275°C	335°C
0	0.094	0.088	0.072	0.068
10	0.112	0.099	0.079	0.076
20	0.119	0.099	0.083	0.079
30	0.125	0.102	0.089	0.077
40	0.154	0.106	0.097	0.086
50	0.147	0.106	0.093	0.086

TABLE NO. XX

Total Normal Absorptivity at Room Temperature
For Incandescent Radiation
(Tungsten Filament)

Composite	Absorptivity
OA	0.594
OB	0.661
5A	0.602
10A	0.679
10B	0.698
15A	0.802
15B	0.755
20A	0.811
20B	0.698
25A	0.887
25B	0.736
30A	0.858
30B	0.755
35A	0.892
35B	0.811
40A	0.896
40B	0.830
45A	0.830
50A	0.924
55A	0.934
60A	0.934

TABLE NO. XXI

Observed Temperature Required to Initiate Fracture in Two-Inch Diameter Spheres (T_{max})

Material	T_{max} (^{o}K)
Zirconium carbide	1725
Zirconium carbide (blackened surface)	1500
Zirconium carbide (plus 50 vol. % graphite)	1900

TABLE NO. XXII

Calculation of Temperature Required to Initiate Fracture (T_{max})

Physical Properties	Zirconium Carbide (blackened surface)	Zirconium Carbide (unblackened)	Zirconium Carbide (+ 50 vol. % graphite)
Strength (S_{tb}) measured in bending (psi)	24,000	24,000	7,240
Homogeneity factor (m)	~4	~4	~11
Strength (S_{ts}) calculated for condition of thermal shock:			
Fracture due to radial stress	8,060	8,060	4,520
Fracture due to tangential stress	14,950	14,950	4,960
Poisson's ratio (ν)	0.17	0.17	0.17
Thermal conductivity (k) (cal. deg.$^{-1}$ cm.$^{-1}$ sec.$^{-1}$)	0.100	0.100	0.166
Coefficient of thermal expansion (α) $^{o}C^{-1}$	5.8×10^{-6}	5.8×10^{-6}	5.8×10^{-6}
Young's modulus of elasticity (E) psi	57.6×10^{6}	57.6×10^{6}	13.00×10^{6}
Emissivity of specimen (ϵ_1)	1.00	0.59	0.92
Emissivity of enclosure (ϵ_2)	0.95	0.95	0.95
Radius (b) cm	2.54	2.54	2.54
Temperature required for fracture (T_{max}) ^{o}K			
Fracture due to radial stress	1320	1500	1920
Fracture due to tangential stress	1545	1750	1965
Observed	1500	1725	1900

TABLE NO. XXIII

Mechanical Properties of the System Silicon Carbide-Graphite
(Room temperature)

Graphite* (vol. %)	Young's Modulus psi (x 10^{-6})	Modulus of Rupture (psi)	Strain at Fracture (x 10^{4})	Elastic Energy Per Unit Volume Stored at Fracture (lb. in^{-2})
3.6	56.29	24,500	4.35	5.33
9.5	50.23	19,900	3.92	3.94
16.8	45.38	16,710	3.69	3.08
19.4	37.53	13,410	4.35	2.40
29.7	33.36	13,910	3.69	2.90
32.4	27.70	12,830	4.64	2.95
34.5	25.71	11,570	4.50	2.59

* Calculated from bulk density, assuming graphite density equal to 1.70 g/cc and silicon carbide density 3.02 g/cc.

TABLE NO. XXIV

Mechanical Properties of Al_2O_3-ZrO_2 Composites

Zirconia (wt. %)	Porosity (%)	Modulus of Rupture (psi)	Young's Modulus of Elasticity (psi (x 10^{-6}))	Strain at Fracture (x 10^4)	Elastic Energy Stored at Fracture
0*	2.85	19,500	51.6	3.78	3.68
10*	7.0	10,100	29.4	3.44	1.73
15*	1.5	13,960	30.8	4.53	3.16
20*	7.0	9,200	24.6	3.75	1.72
25*	9.8	13,000	26.1	4.98	3.24
30*	2.0	9,850	21.4	4.60	2.27
0**	0	21,940	53.19	4.13	4.53
9.8**	0	14,250	26.74	5.33	3.80

* Hot pressed.
** Fused. Obtained from Electro Minerals Division, The Carborundum Company.

TABLE NO. XXV

Table to Illustrate Proposed Equation for the Porosity Dependence of Young's Modulus of Elasticity of Polycrystalline Ceramics on the Basis of Published Data for Alumina

Reference	No. of Data	Method of Fabrication	Measurement Technique***	Porosity+ Range (%)	Zero Porosity Modulus	Constant A	Mean Error Between Calculated and Observed Values (%)
Lang[15]	9	C. P. *	E_{fe}	2.13-16.42	60.21	3.95	0.63
Lang[15]	9	C. P.	E_{fw}	2.13-16.42	60.37	3.97	0.58
Lang[15]	7	C. P.	E_1	4.09-16.42	61.29	4.16	0.64
Chung, et al.[14]	13	H. P. **	E_{fw}	0.30- 4.32	59.54	4.07	0.38

* Cold pressed and sintered.
** Hot pressed.
*** Measurement technique: E_{fe} = edgewise flexural resonant frequency
E_{fw} = flatwise flexural resonant technique
E_1 = longitudinal resonant technique
\+ Theoretical density taken as 3.987 g/cc.

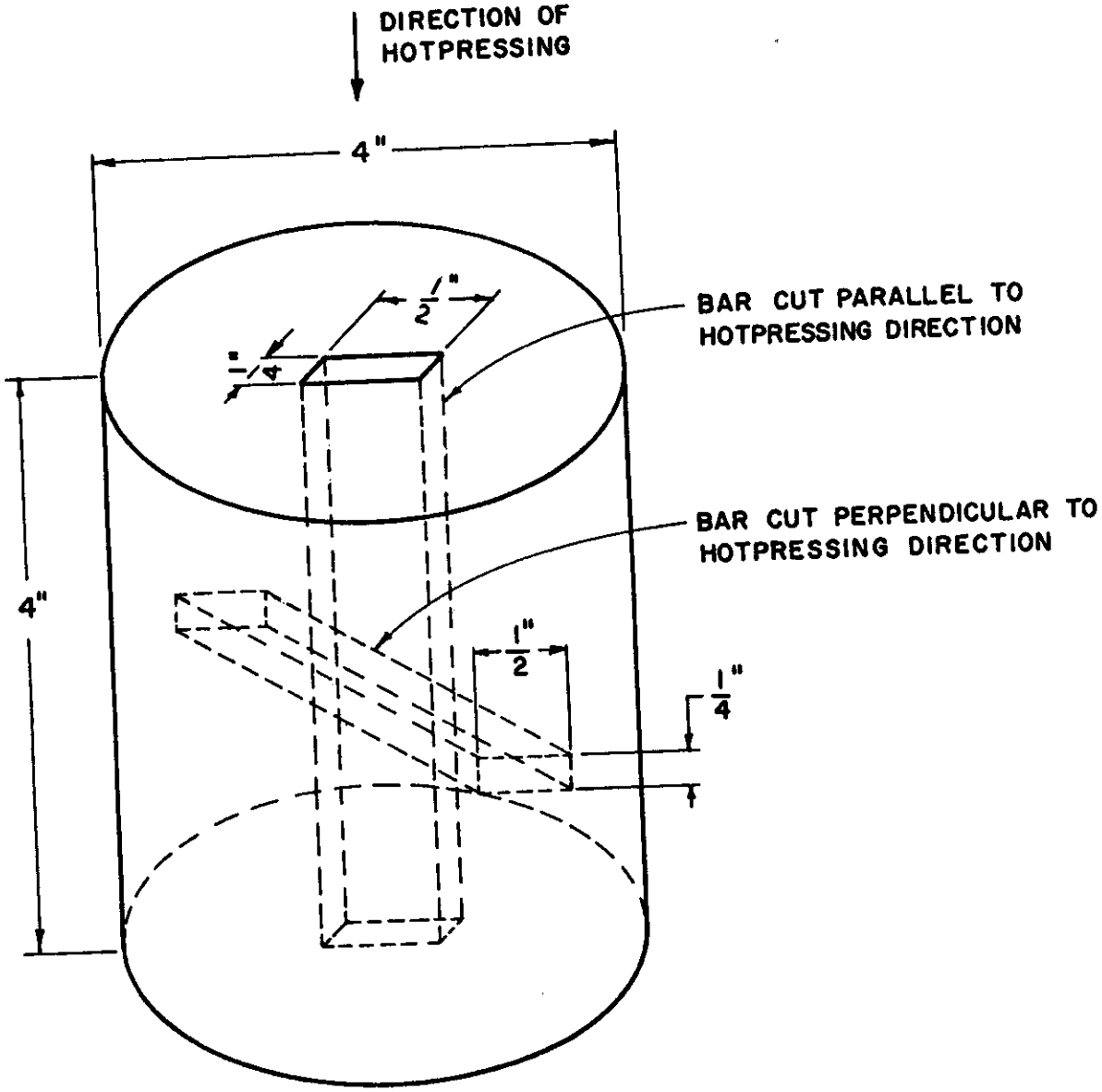

Figure 1 - Orientation of Test Specimens Cut from Hot Pressed Composite With Respect to Hot Pressing Direction.

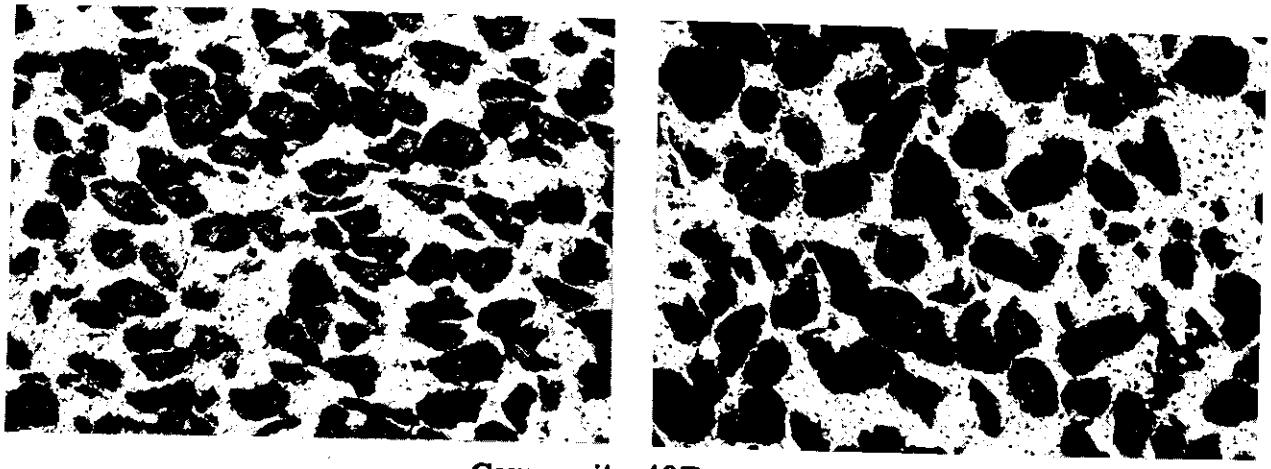

Composite 40B

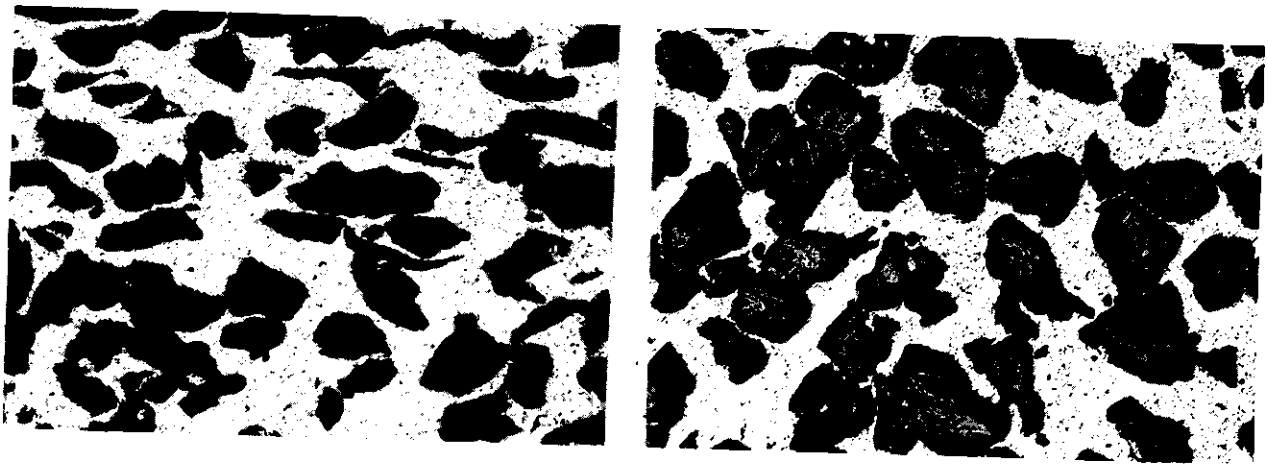

Composite 45A

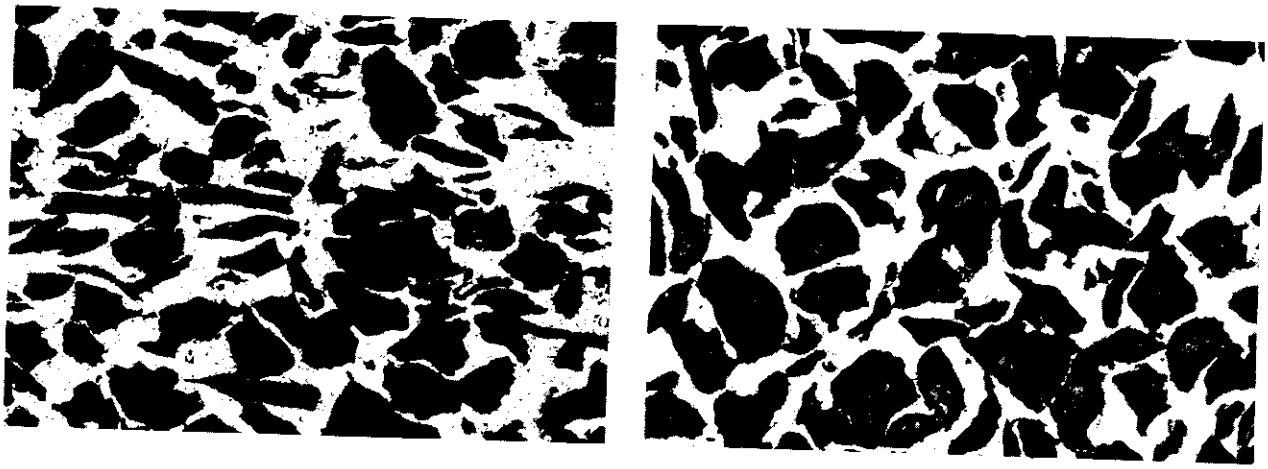

Composite 60A

Figure 2 - Photomicrographs of Polished Sections of Zirconium Carbide-Graphite Composites Showing Anisotropy (X100)
Left: Viewed Perpendicular to Hot Pressing Direction.
Right: Viewed Parallel to Hot Pressing Direction

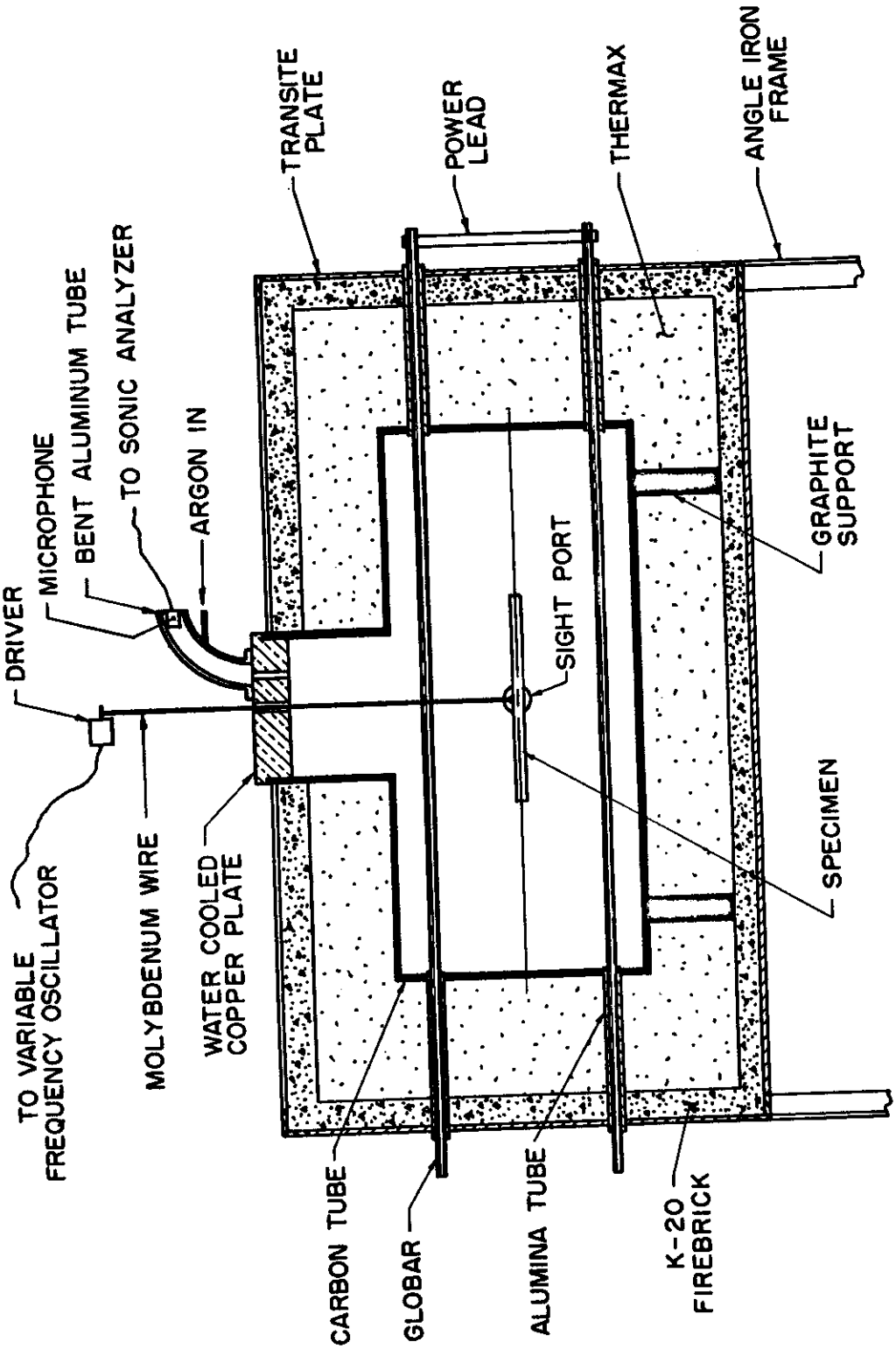

Figure 3 - Furnace for Measuring Young's Modulus of Elasticity at High Temperatures.

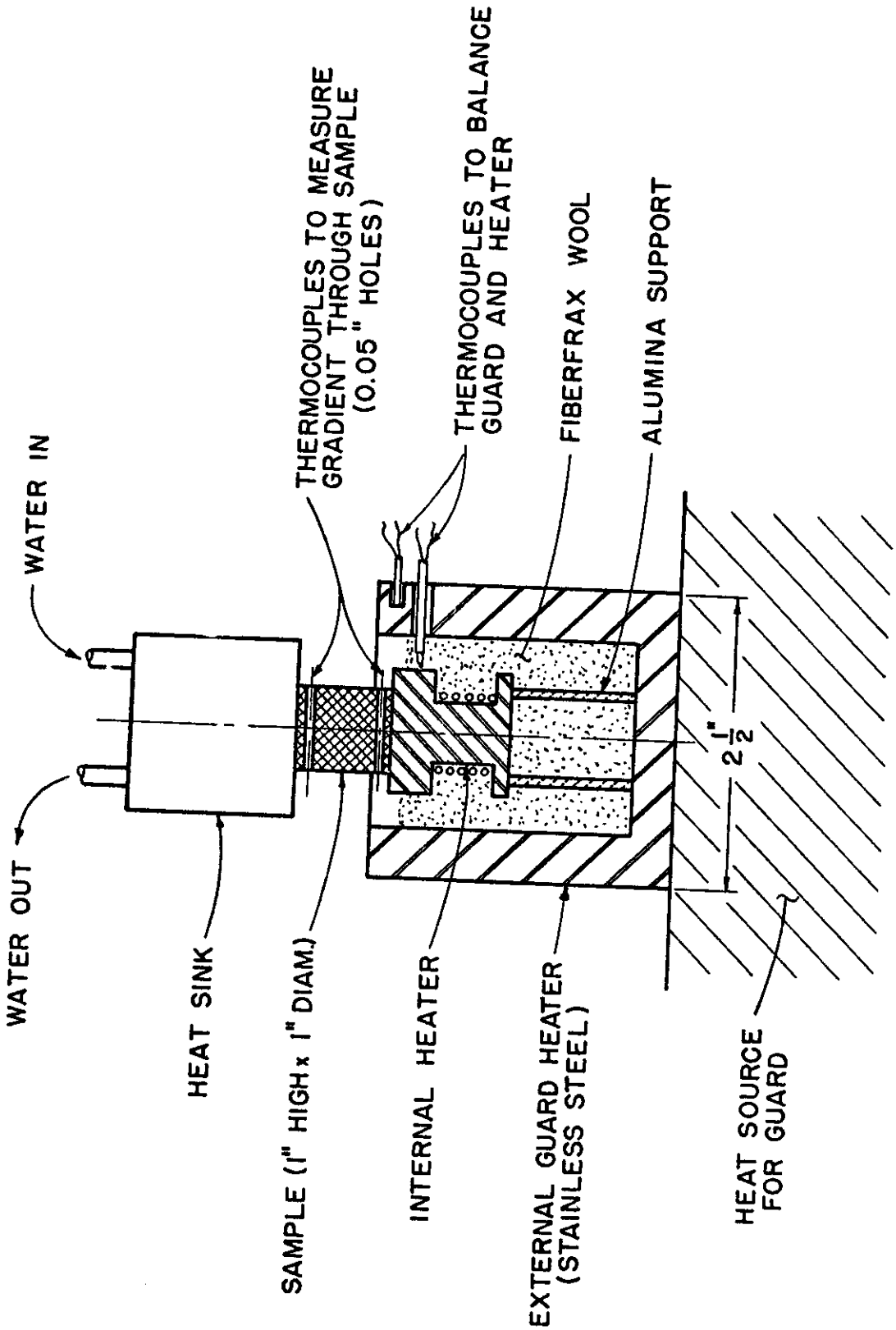

Figure 4 - Apparatus for Measuring Thermal Conductivity by Absolute Method.

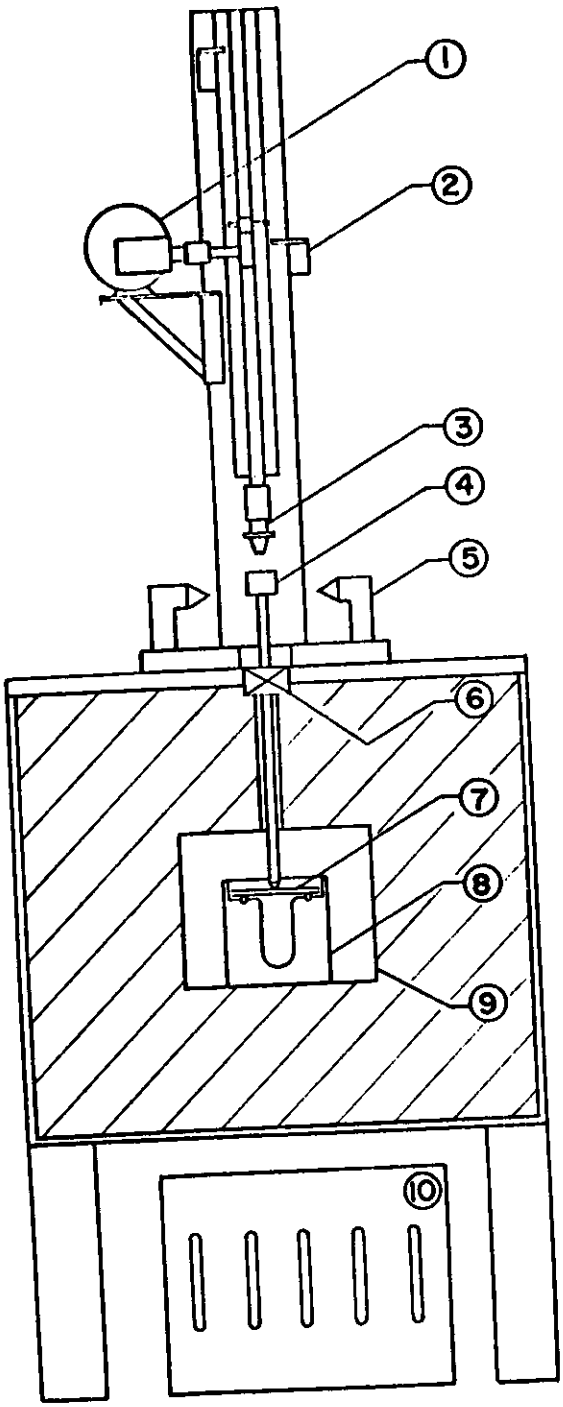

1. Return Mechanism
2. Limit Switch
3. Magnet Pickup
4. Plunger
5. Photo Cell (electric eye)
6. Linear Ballbearing Bushing
7. Specimen
8. Specimen Mount
9. Furnace Pot
10. Time Interval Meter

Figure 5 - Apparatus for Measuring Impact Resistance.

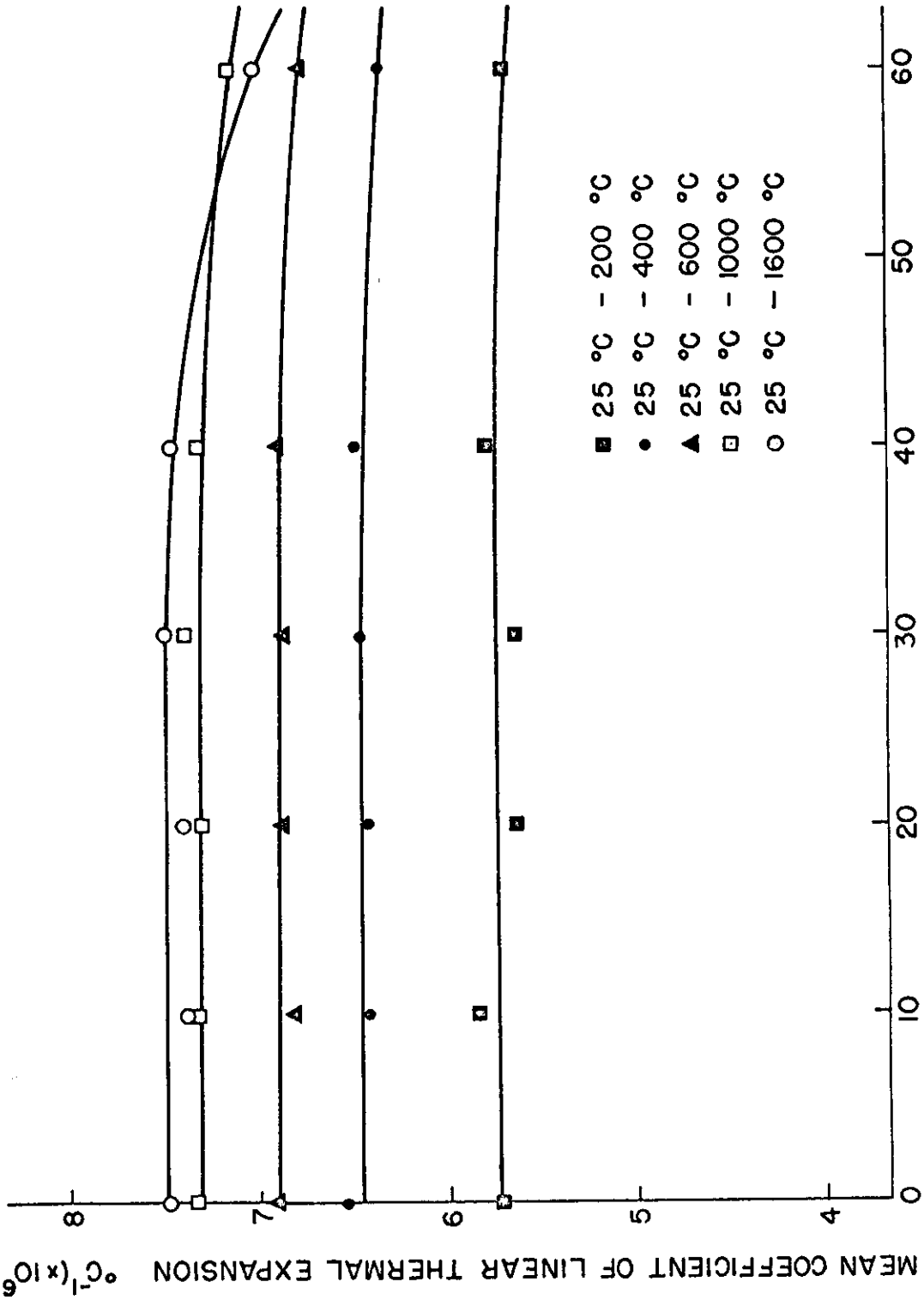

Figure 6 - Coefficient of Thermal Expansion.

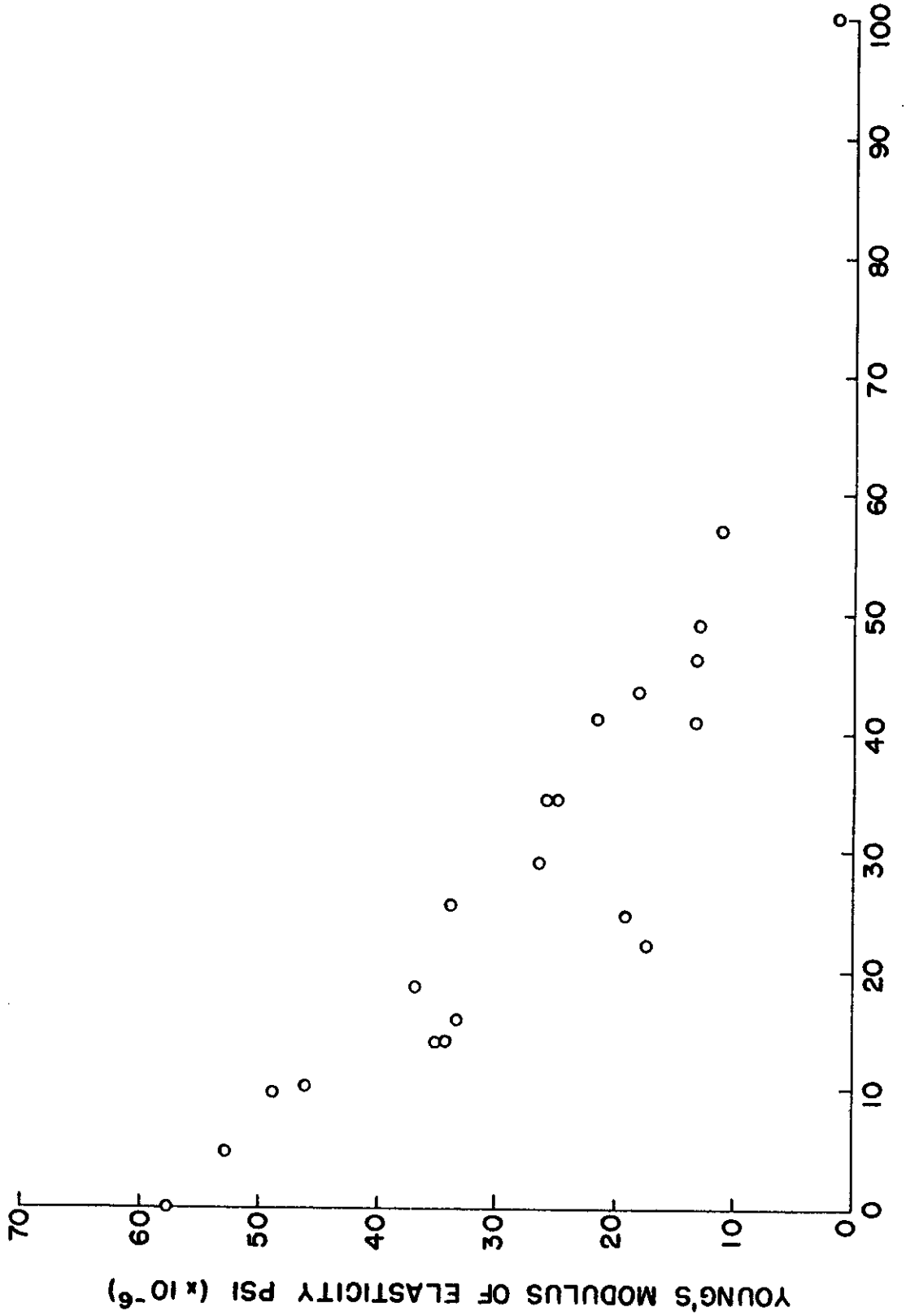

Figure 7 - Young's Modulus of Elasticity Perpendicular to Hot Pressing Direction as a Function of Volume Content Graphite.

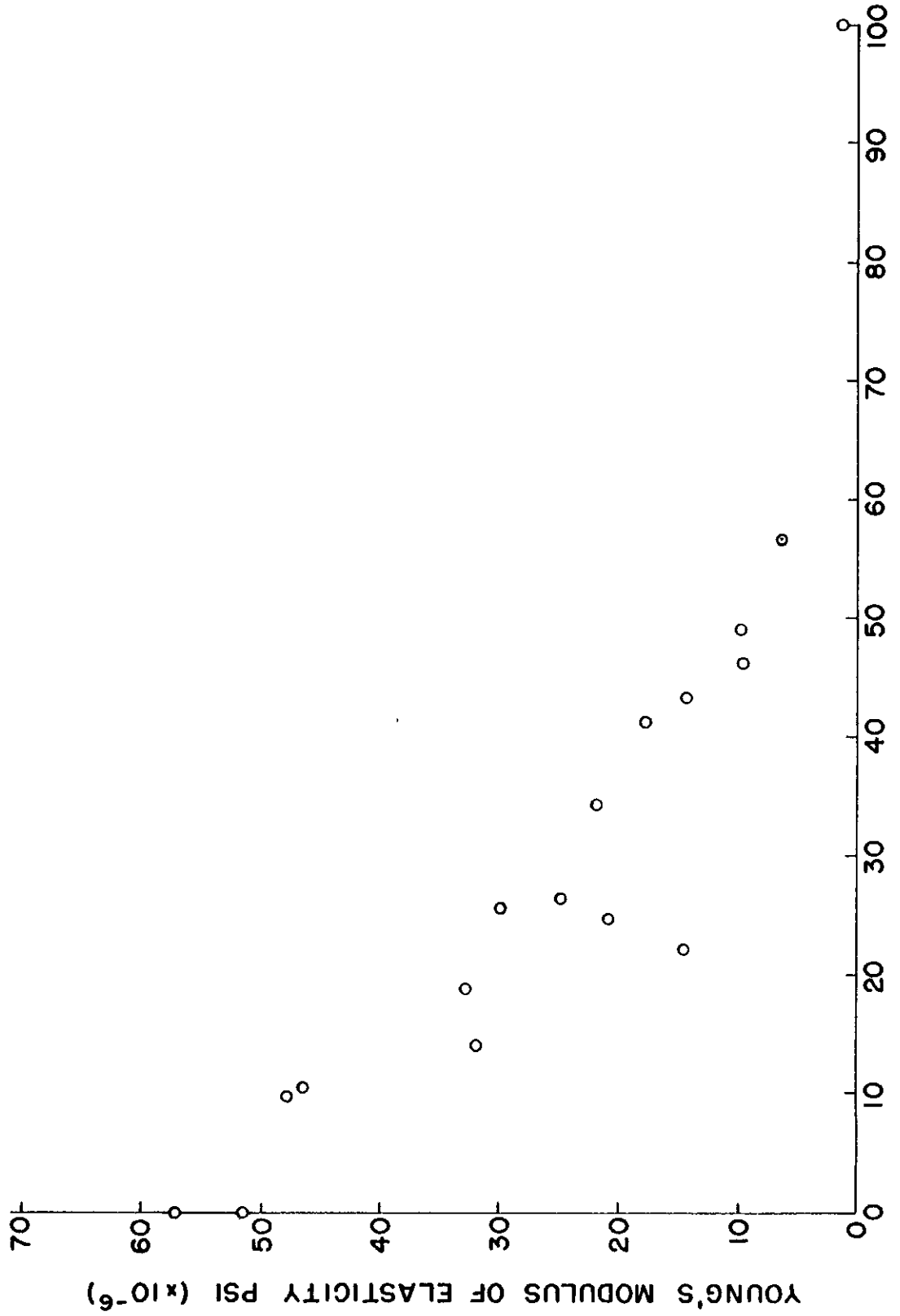

Figure 8 - Young's Modulus of Elasticity Parallel to the Hot Pressing Direction as a Function of Volume Content Graphite.

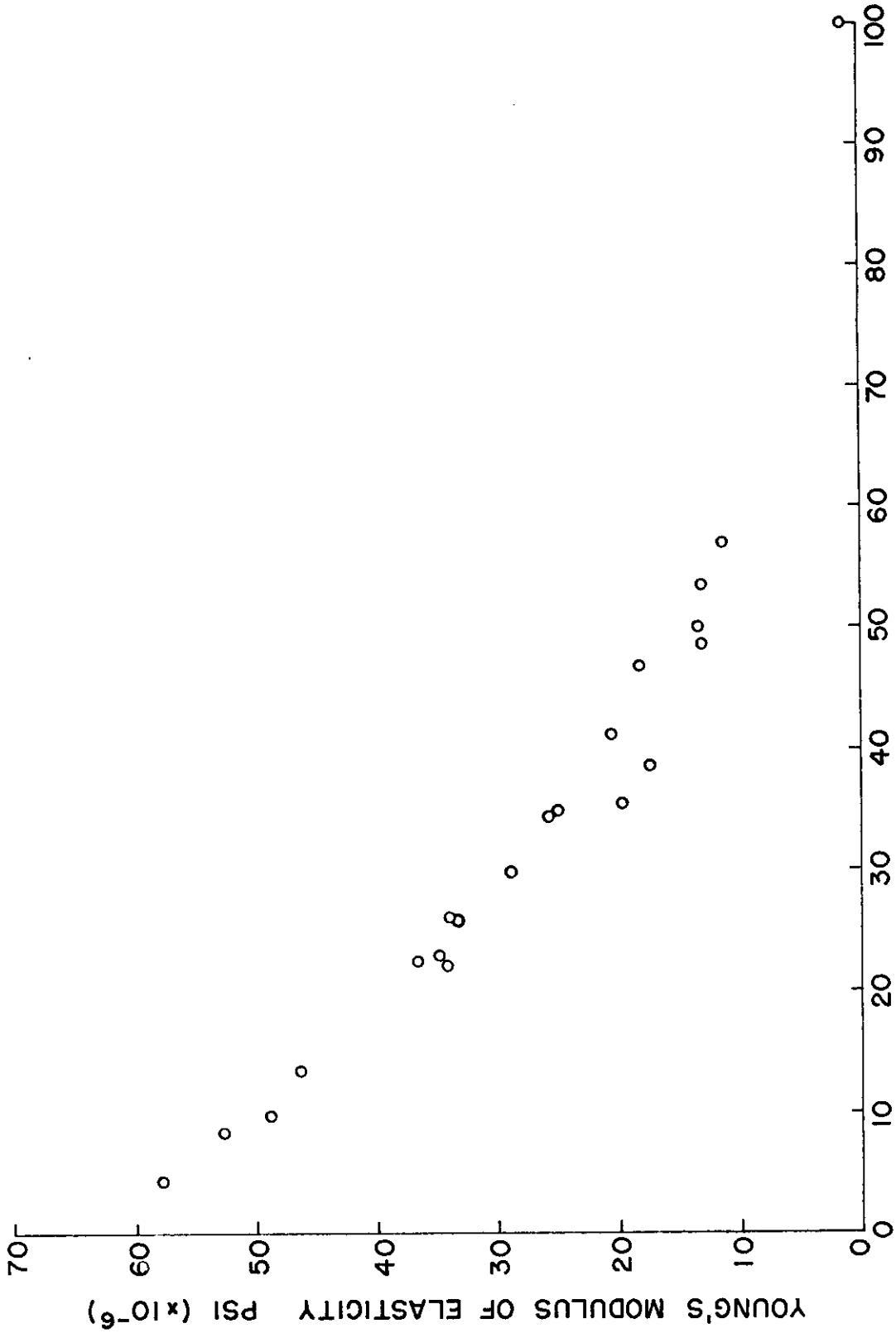

Figure 9 - Young's Modulus of Elasticity Perpendicular to the Hot Pressing Direction as a Function of Volume Content Graphite Plus Porosity.

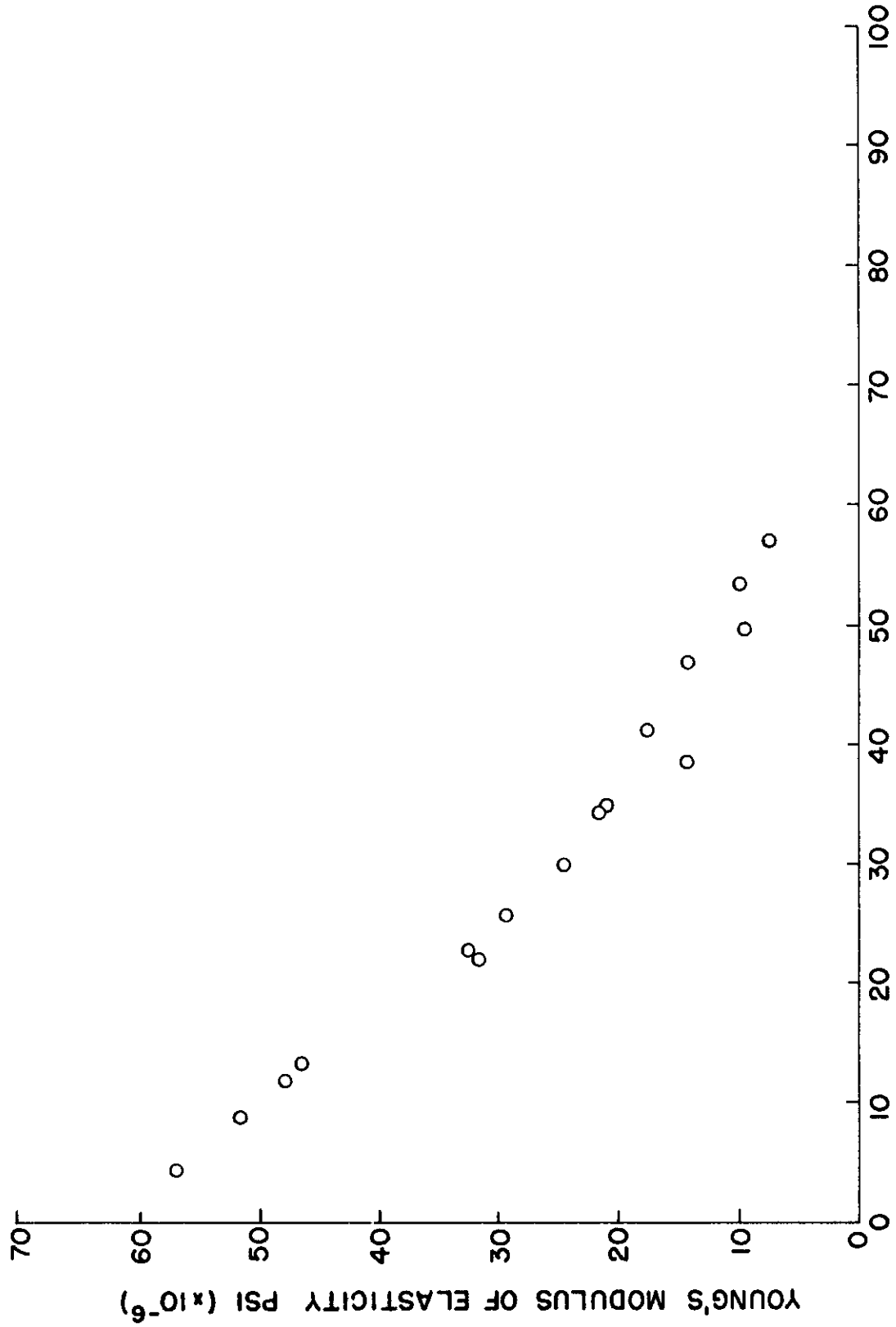

Figure 10 - Young's Modulus of Elasticity Parallel to the Hot Pressing Direction as a Function of Volume Content Graphite Plus Porosity.

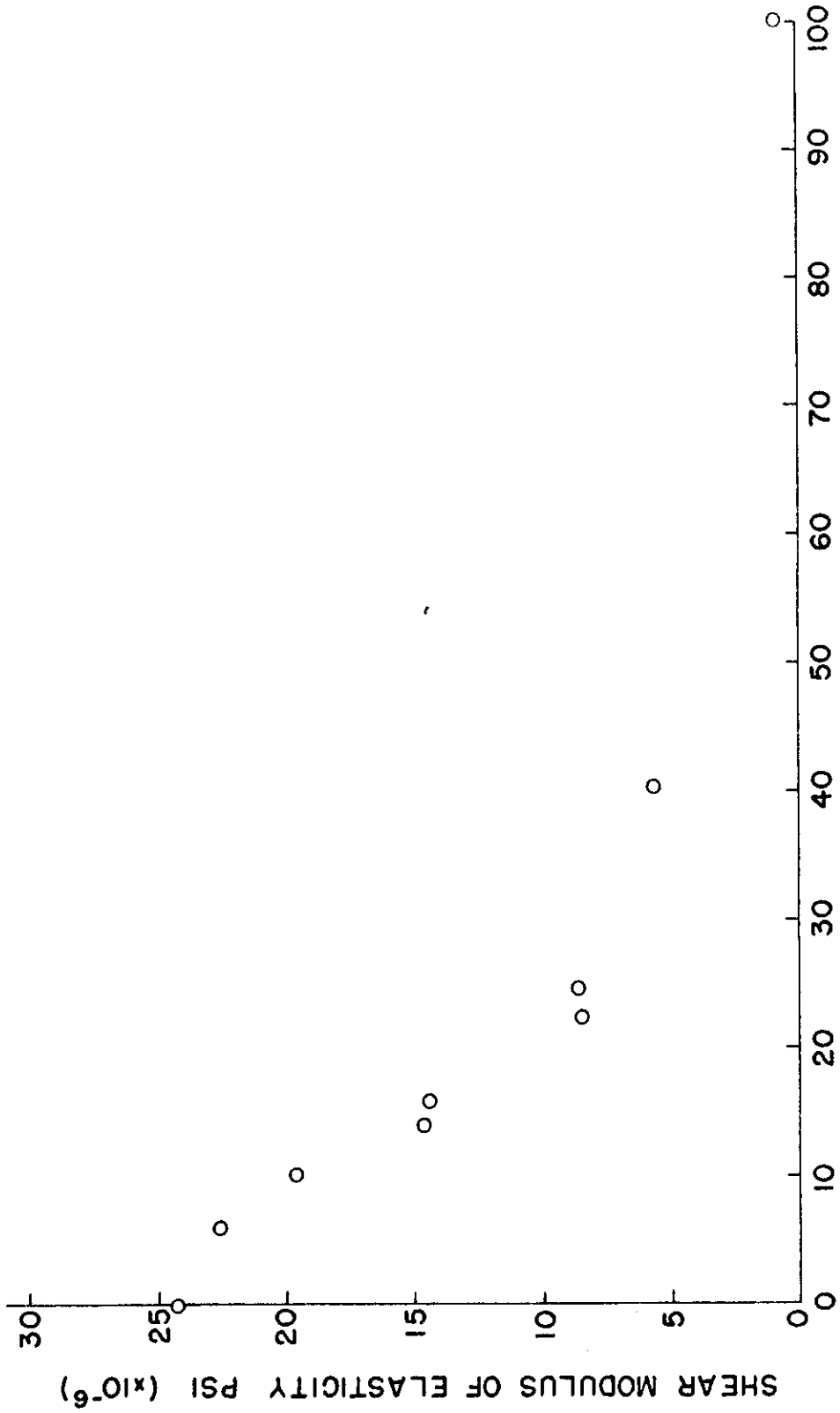

Figure 11 - Shear Modulus of Elasticity as a Function of Volume Content Graphite.

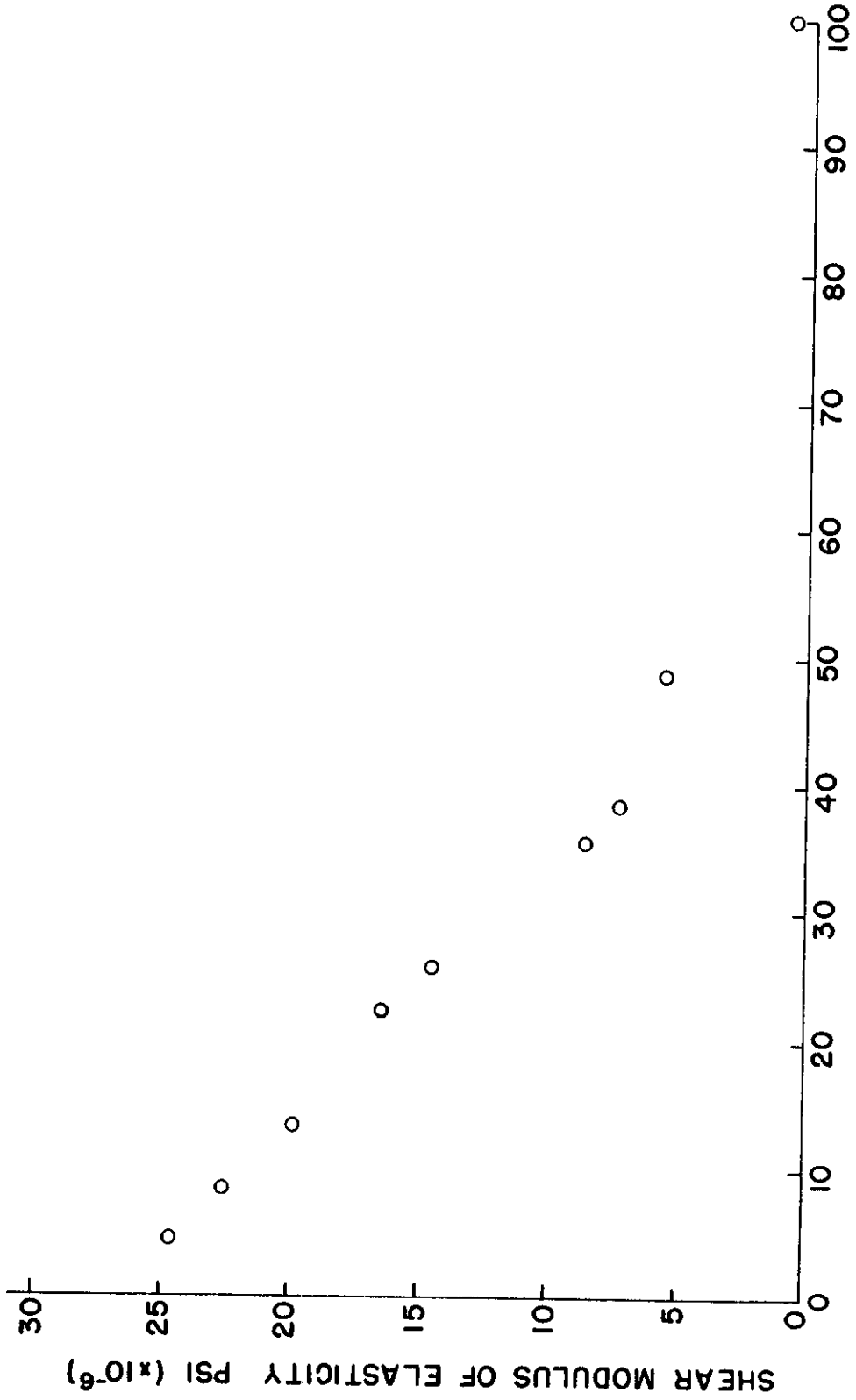

Figure 12 - Shear Modulus of Elasticity as a Function of Volume Content Graphite Plus Porosity.

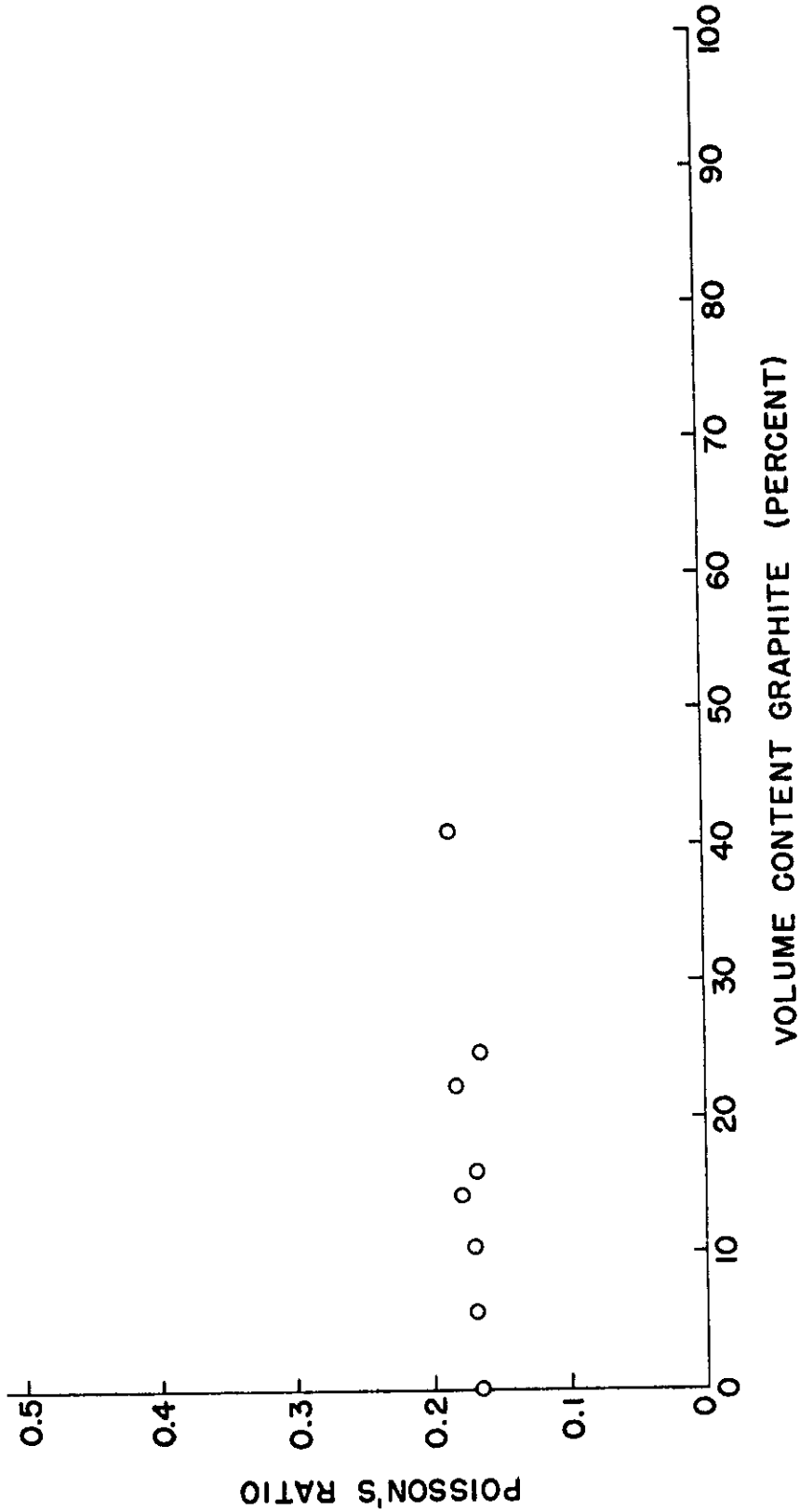

Figure 13 - Poisson's Ratio

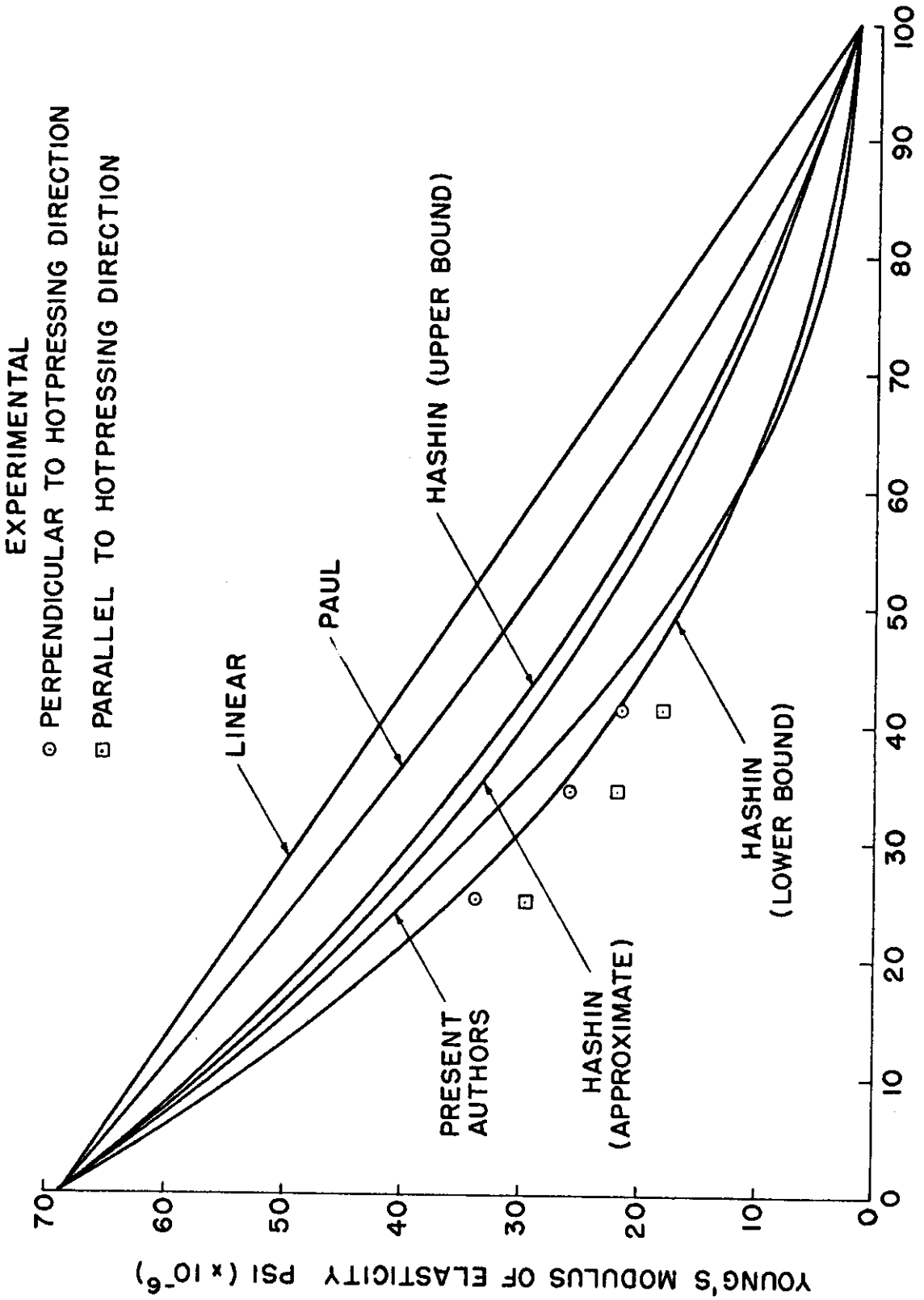

Figure 14 - Experimental Values for Young's Modulus of Elasticity of Zirconium Carbide-Graphite Compared to Various Equations from the Literature.

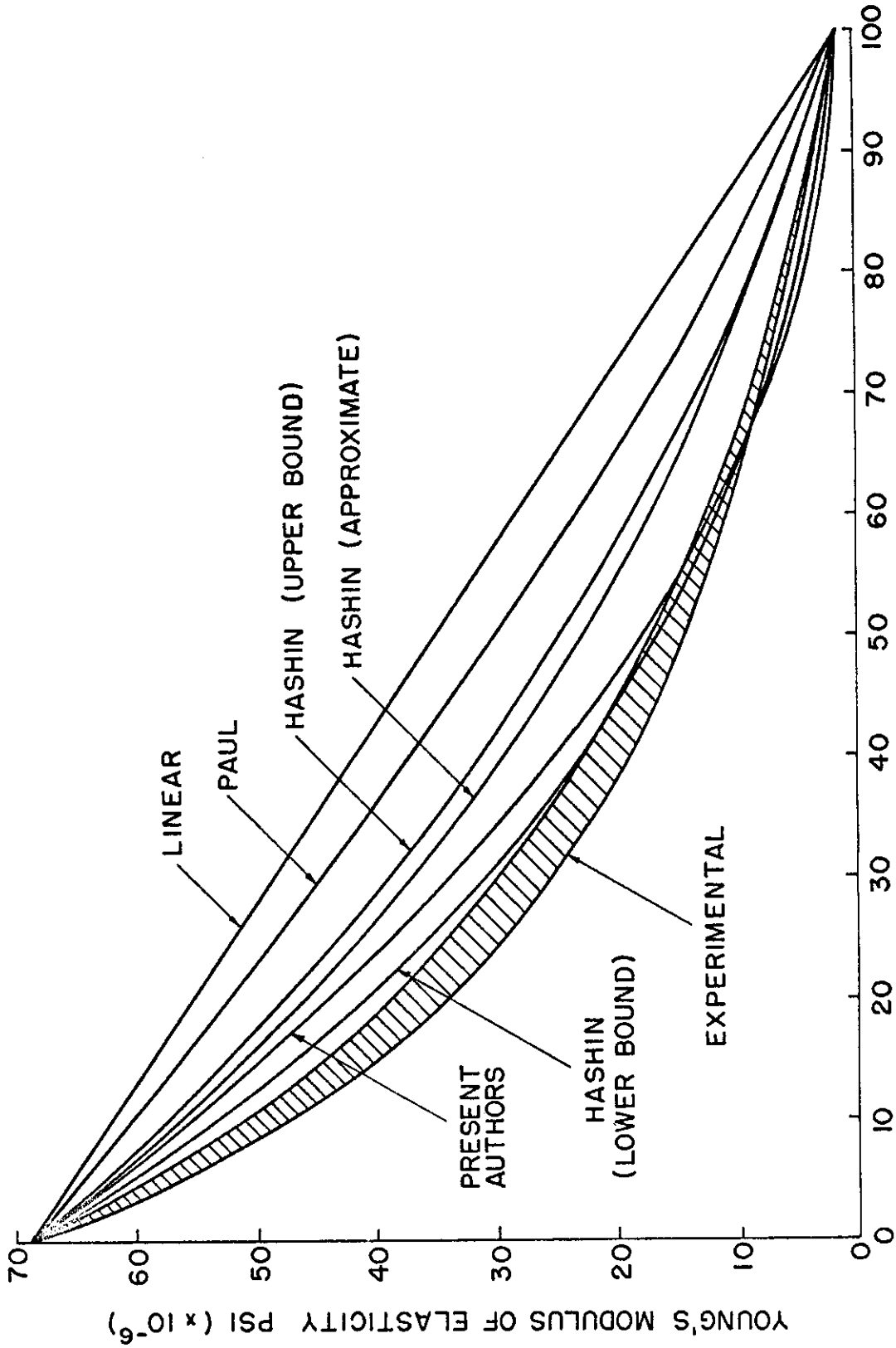

Figure 15 - Calculated Curves of the Experimental Values of Young's Modulus of Elasticity of Zirconium Carbide-Graphite Compared to Various Equations from the Literature.

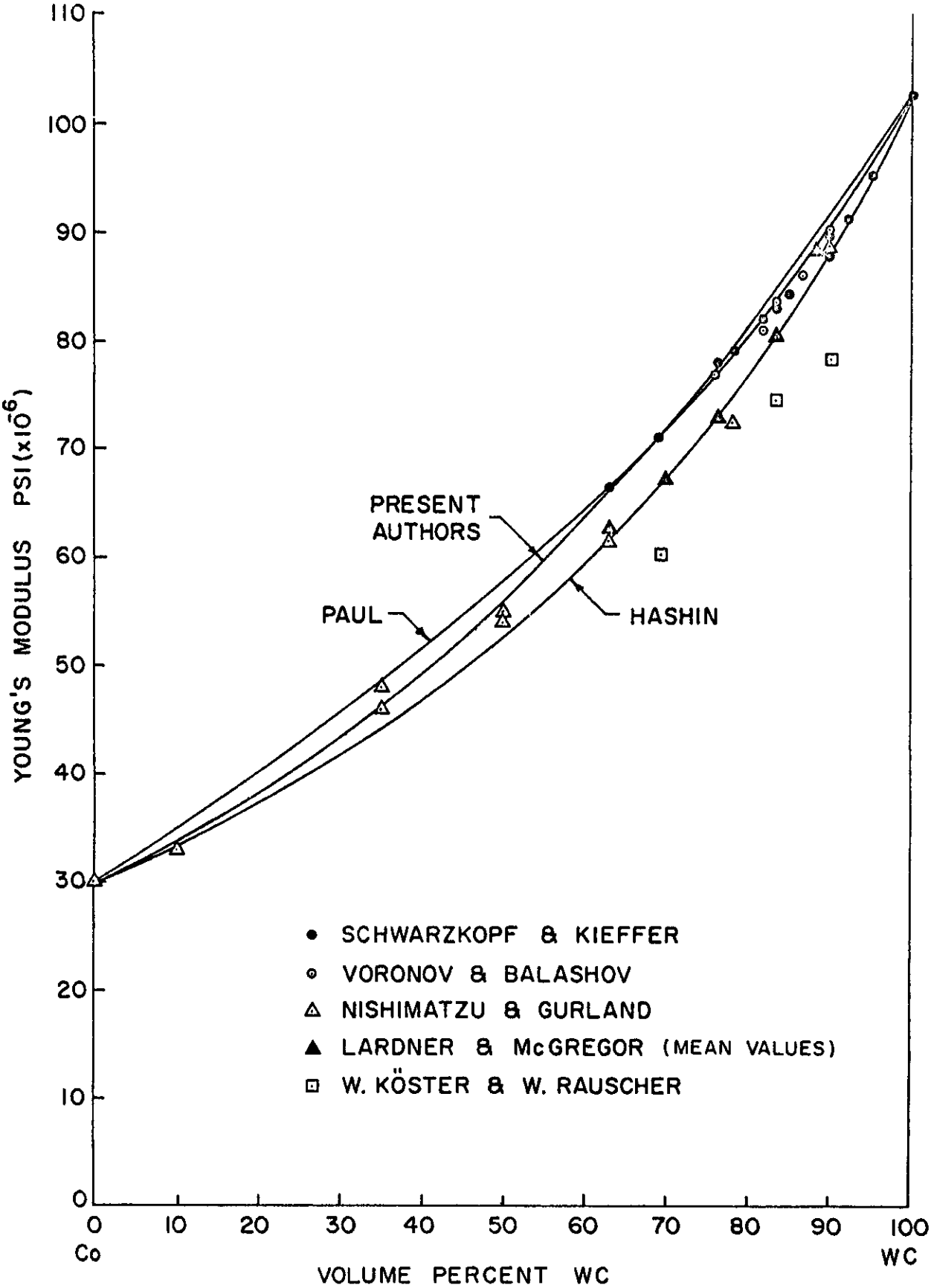

Figure 16 - Experimental Data of the System WC-Co Compared to Various Equations from the Literature.

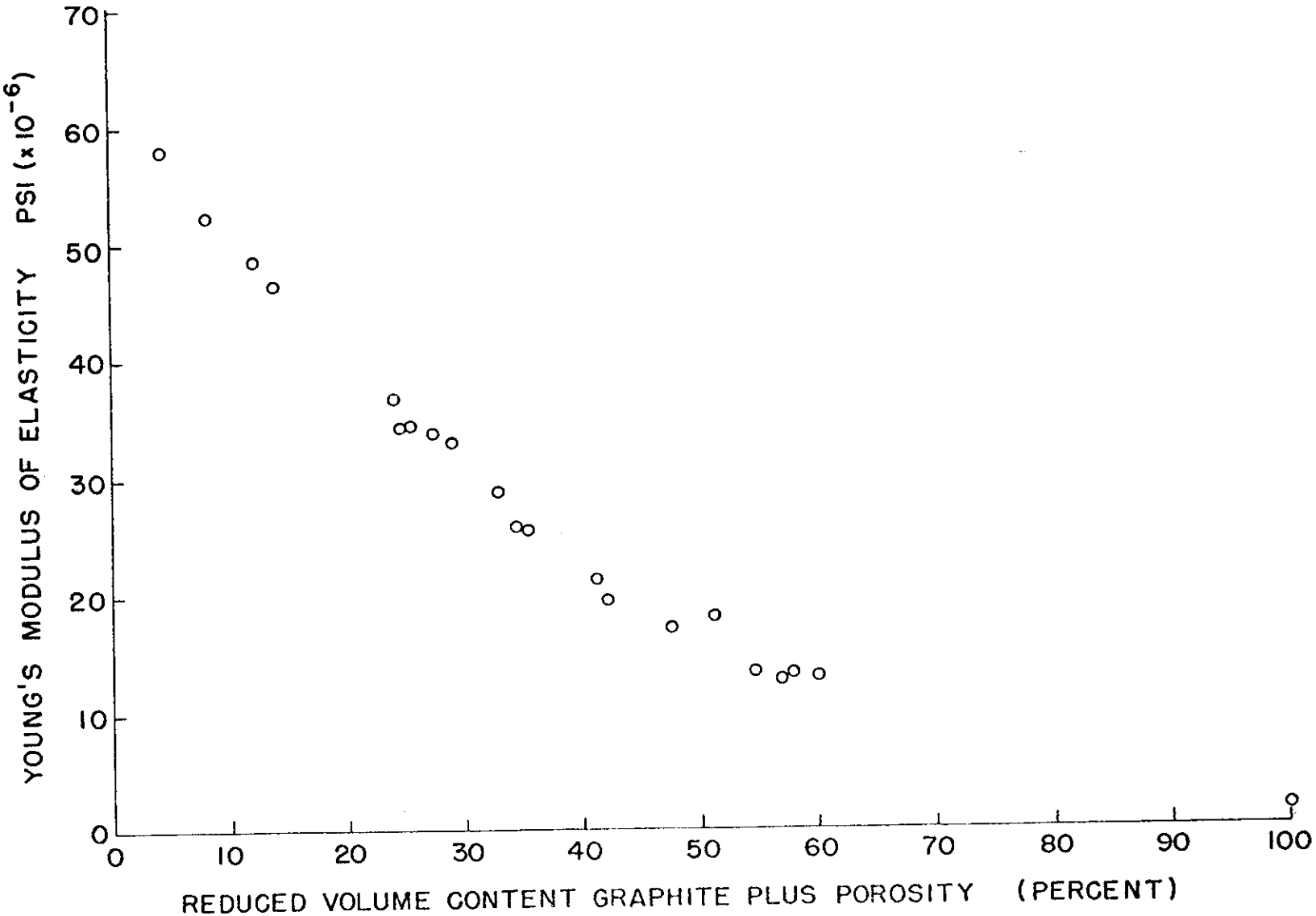

Figure 17 - Young's Modulus of Elasticity Perpendicular to the Hot Pressing Direction as a Function of Reduced Volume Content Graphite Plus Porosity.

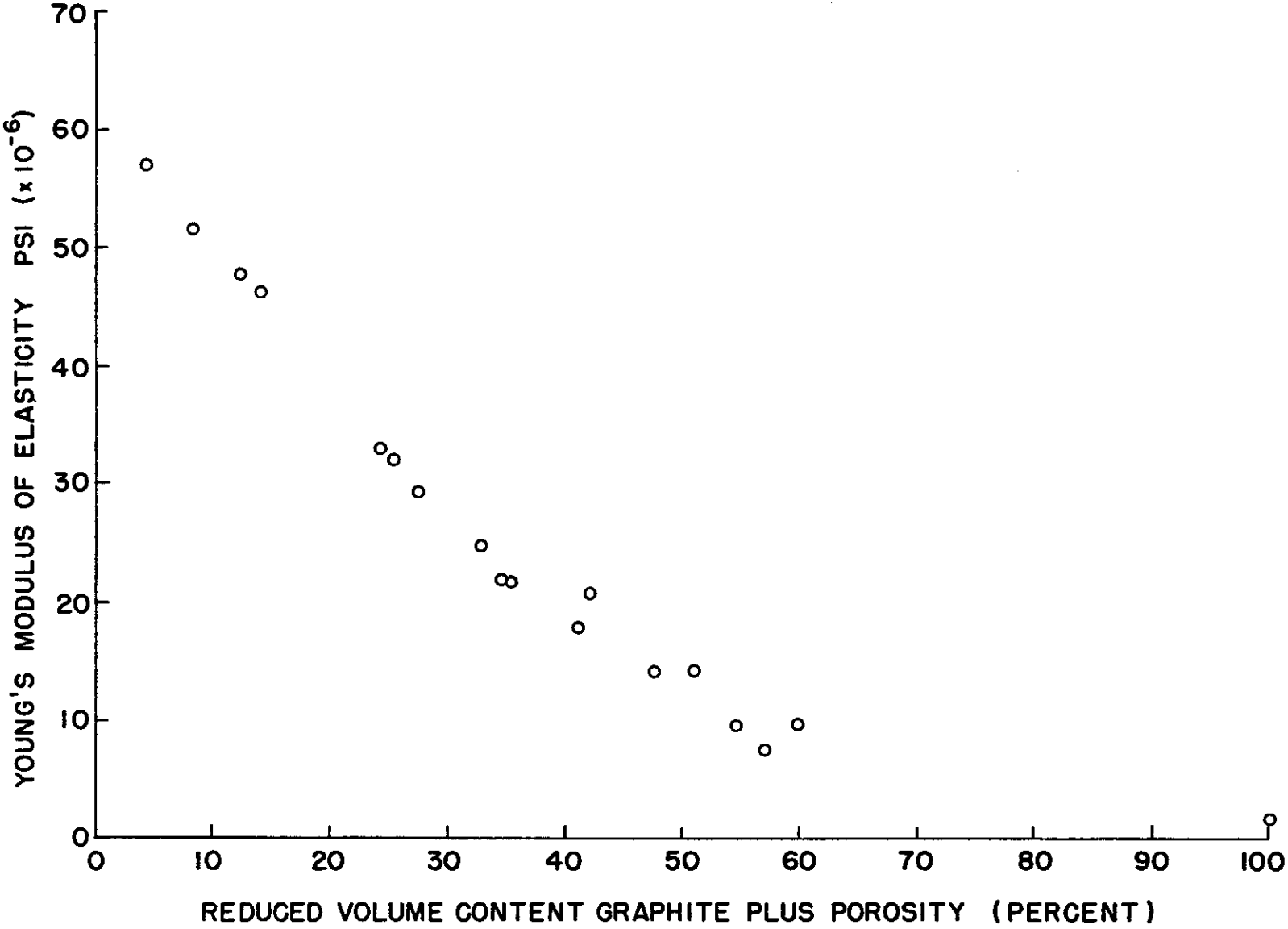

Figure 18 - Young's Modulus of Elasticity Parallel to the Hot Pressing Direction as a Function of Reduced Volume Content Graphite Plus Porosity.

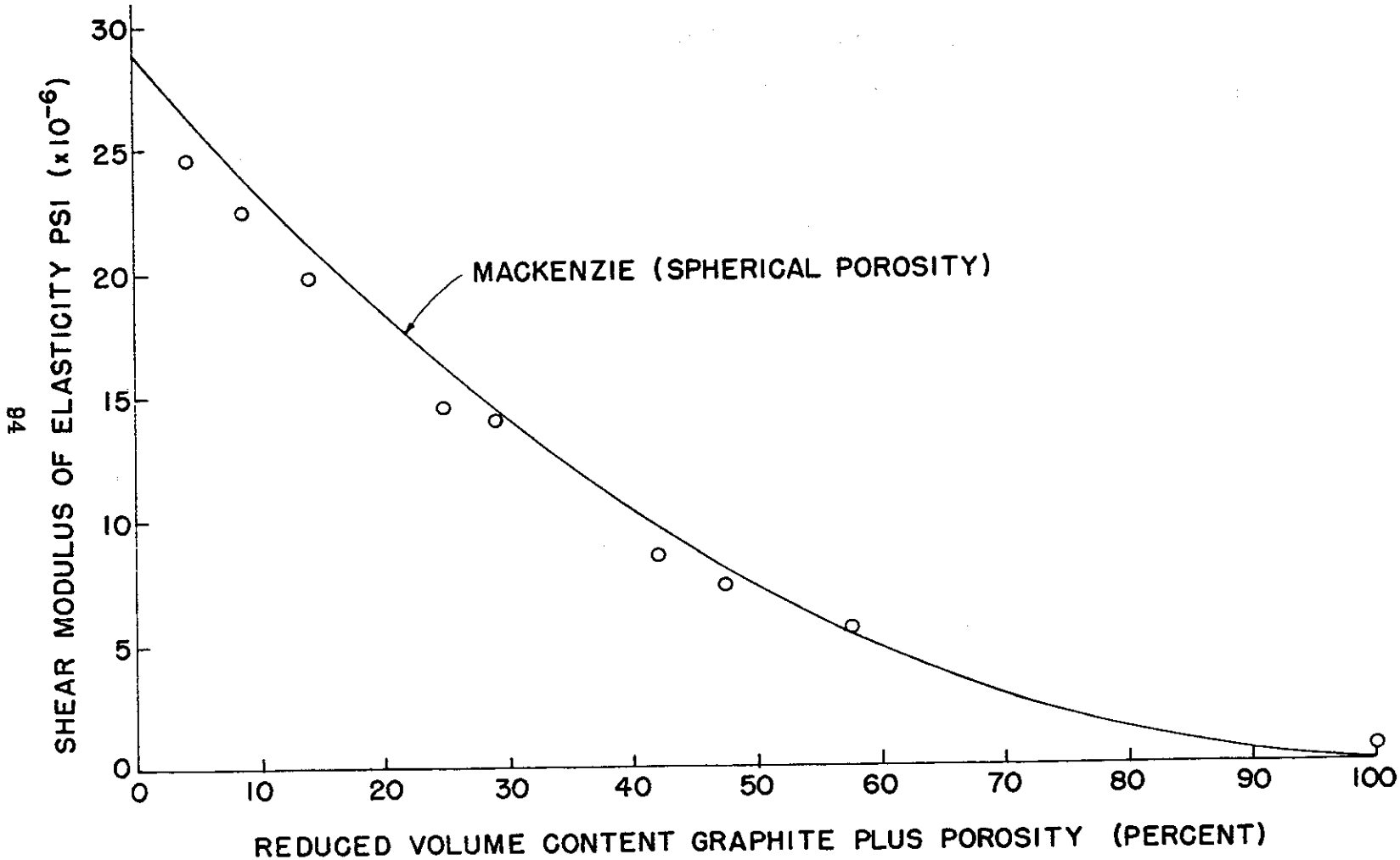

Figure 19 - Shear Modulus of Elasticity as a Function of Reduced Volume Content Graphite Plus Porosity.

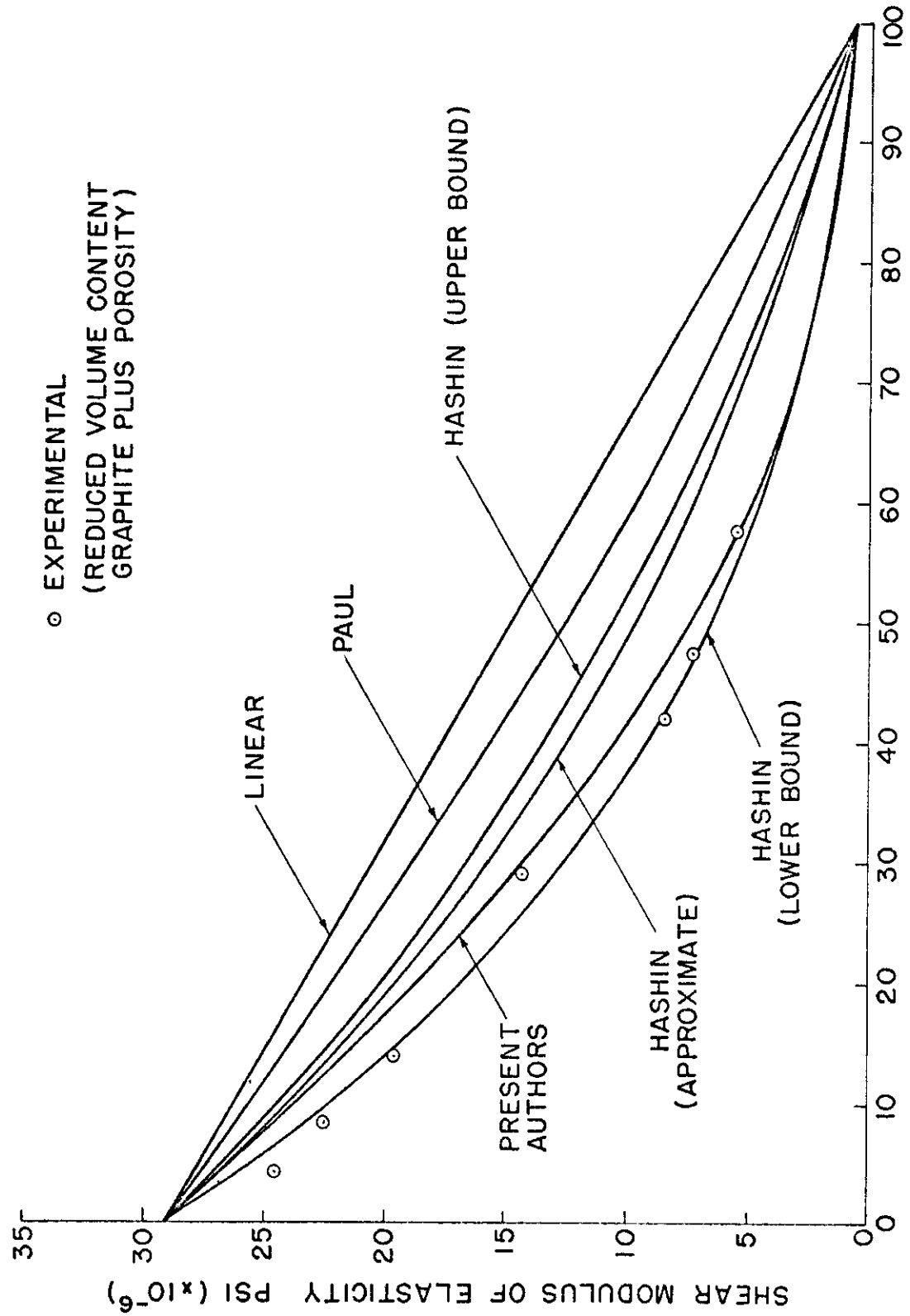

Figure 20 - Calculated Curves of the Shear Modulus of Elasticity of the System Zirconium Carbide-Graphite.

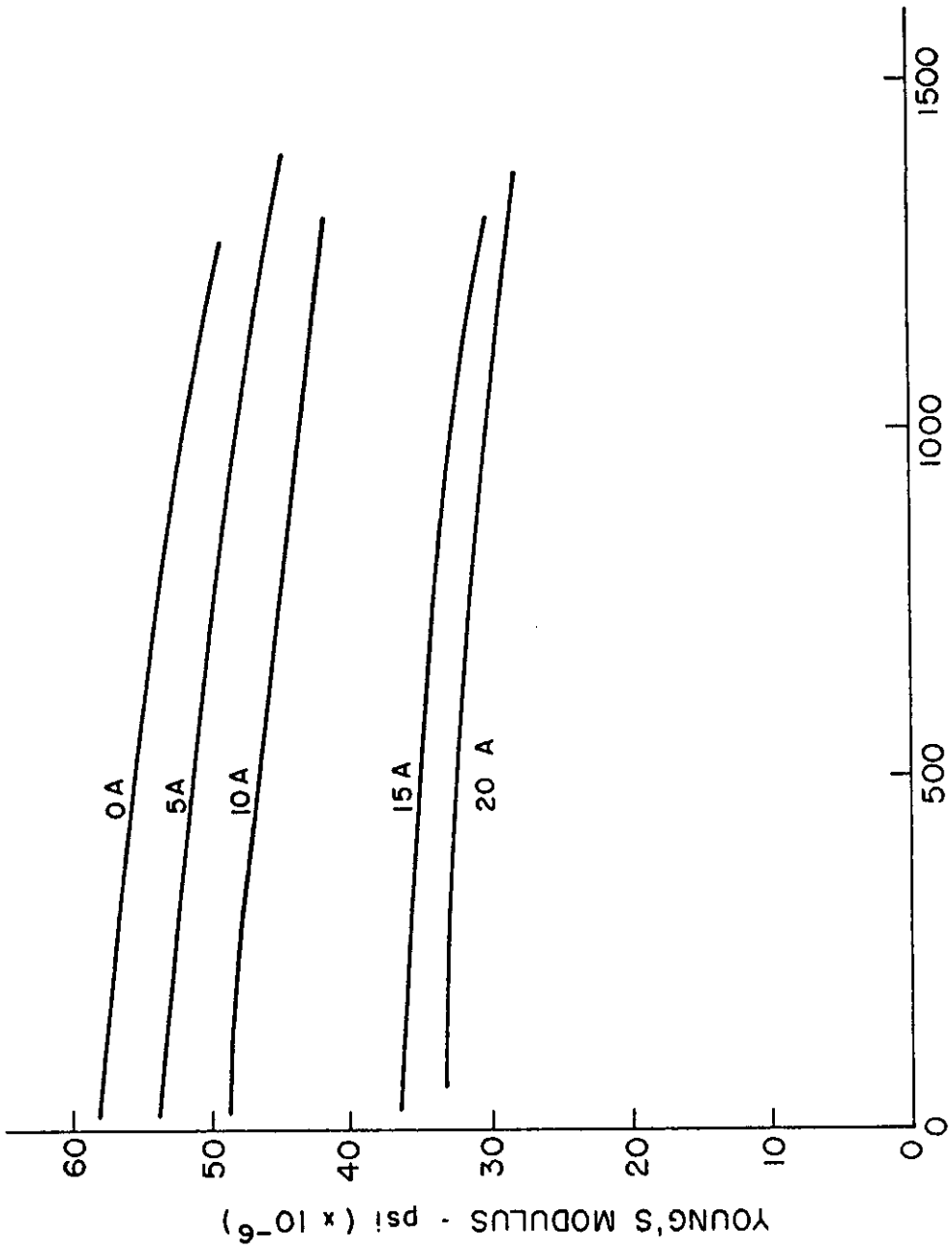

Figure 21 - Young's Modulus of Elasticity as a Function of Temperature. (The numbers on the curves refer to the composite).

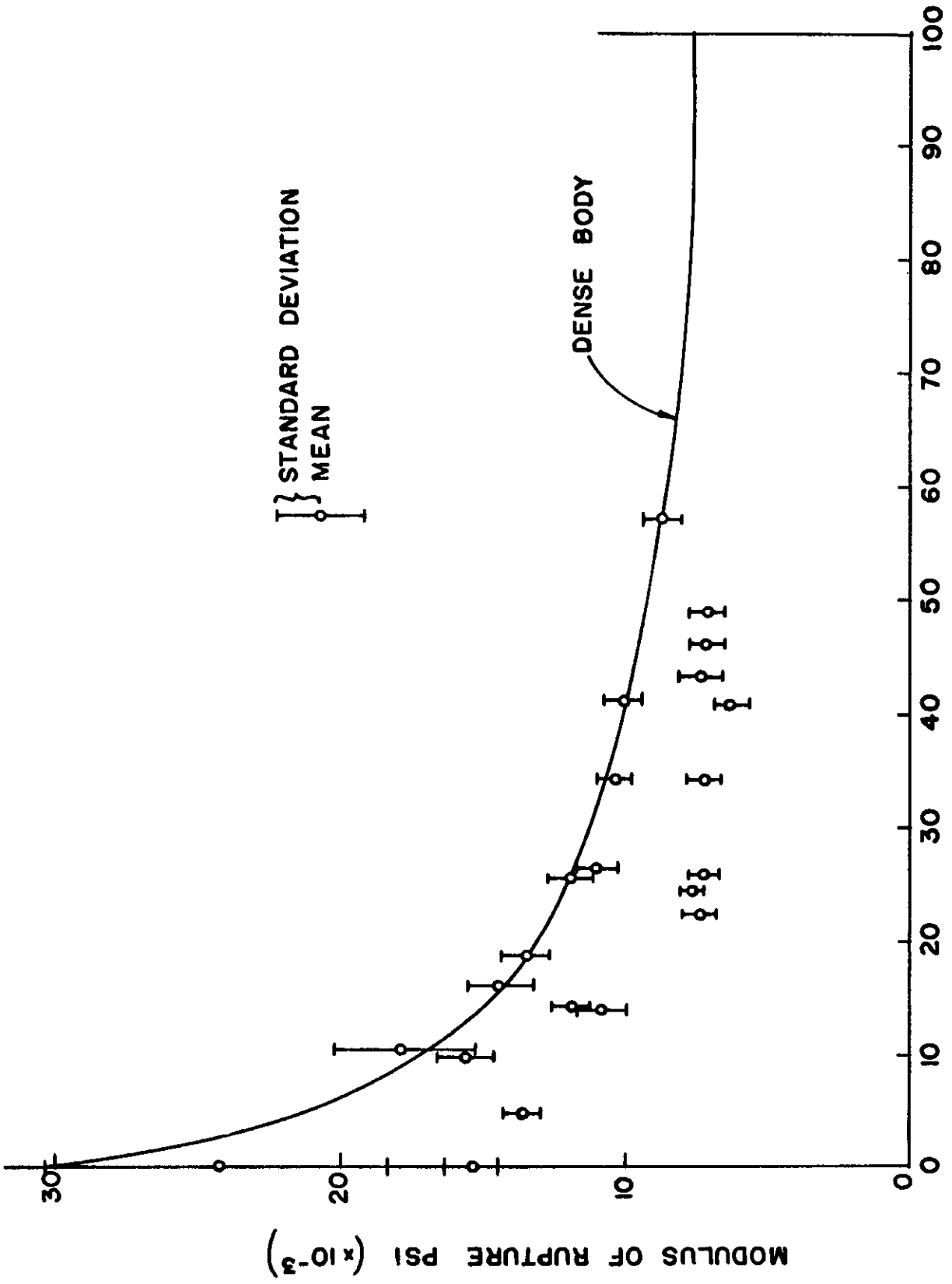

Figure 22 - Modulus of Rupture at Room Temperature Perpendicular to the Hot Pressing Direction as a Function of Volume Content Graphite.

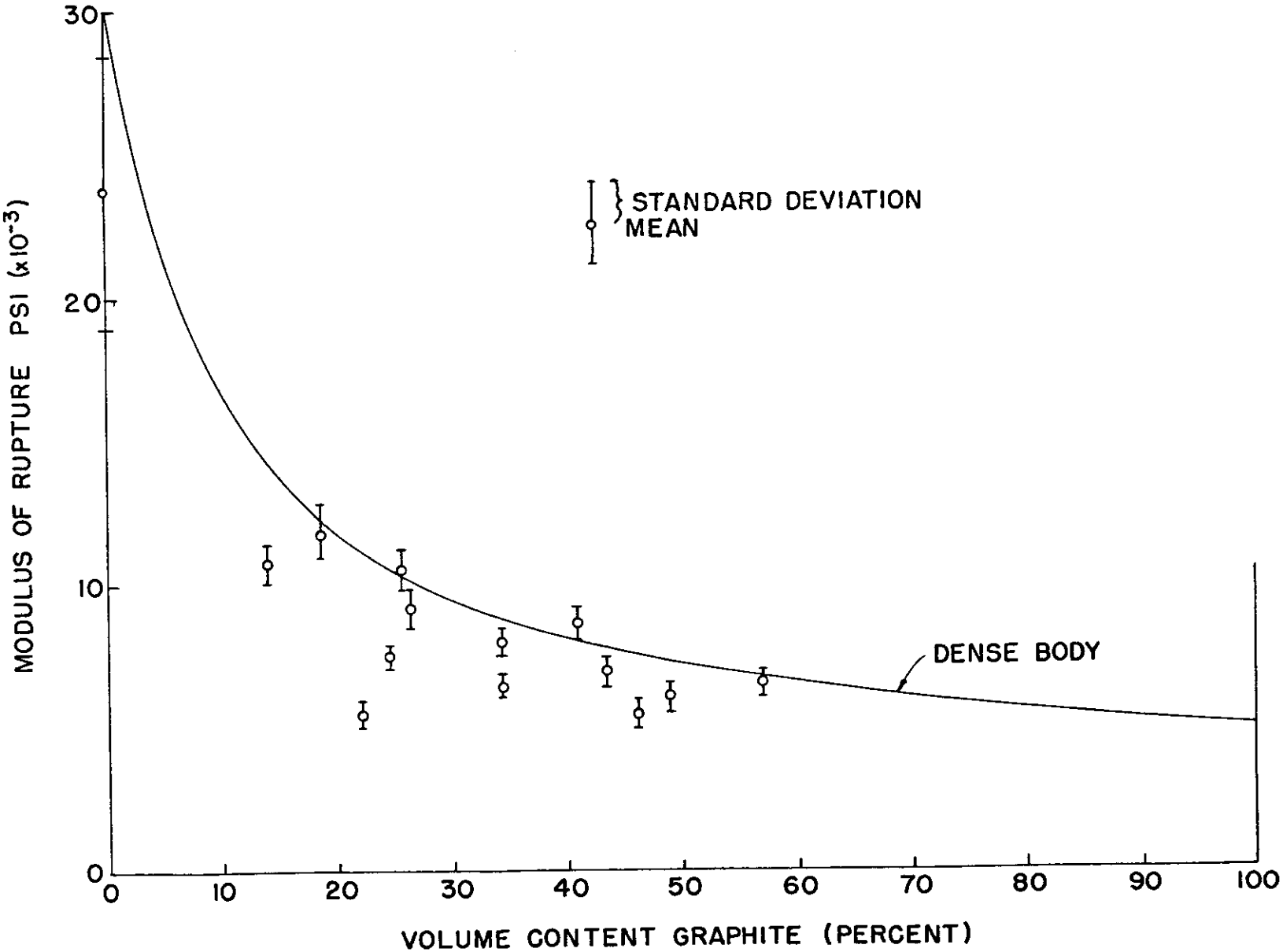

Figure 23 - Modulus of Rupture at Room Temperature Parallel to the Hot Pressing Direction as a Function of Volume Content Graphite.

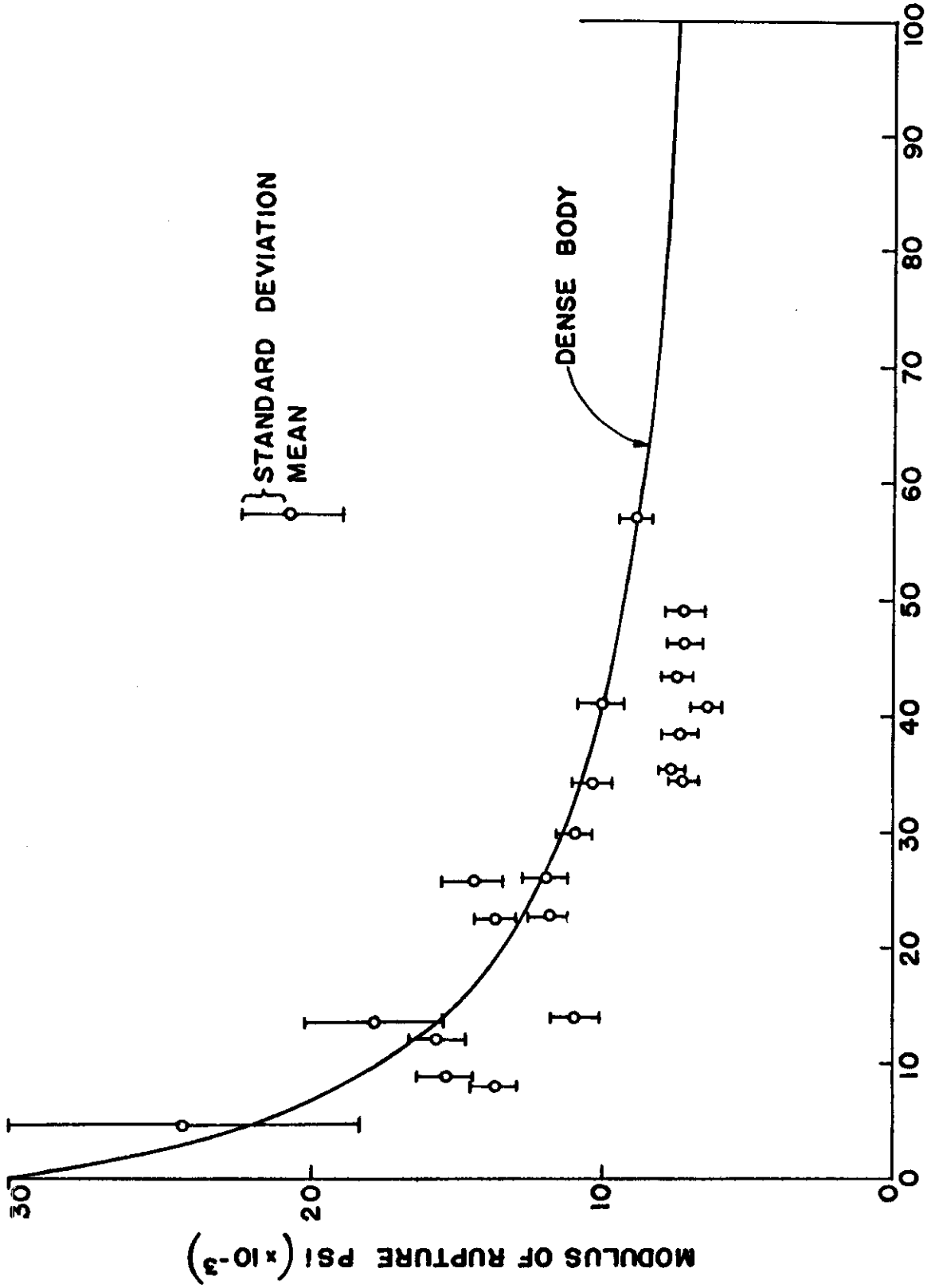

Figure 24 - Modulus of Rupture at Room Temperature Perpendicular to the Hot Pressing Direction as a Function of Volume Content Graphite Plus Porosity.

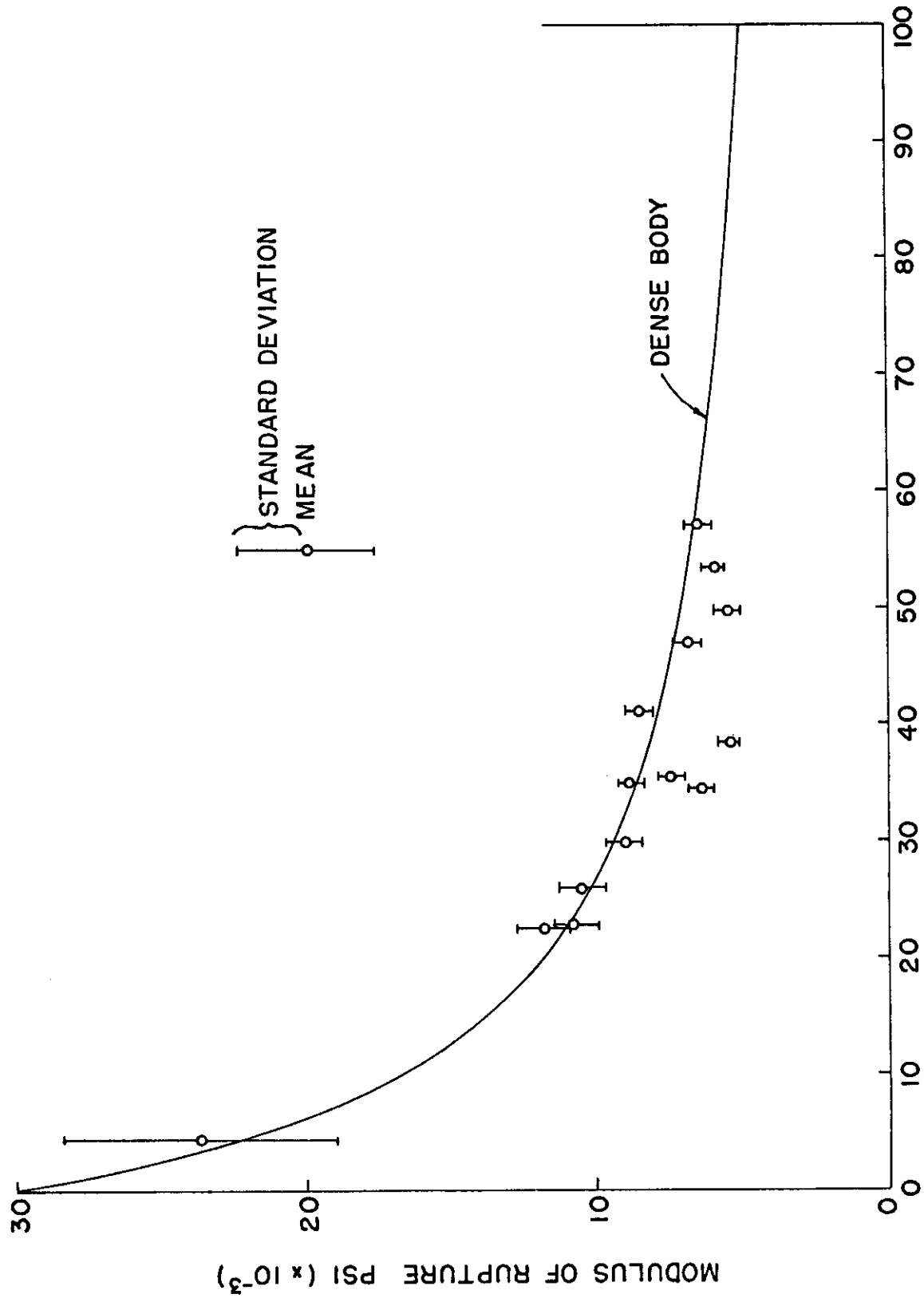

Figure 25 - Modulus of Rupture at Room Temperature Parallel to the Hot Pressing Direction as a Function of Volume Content Graphite Plus Porosity.

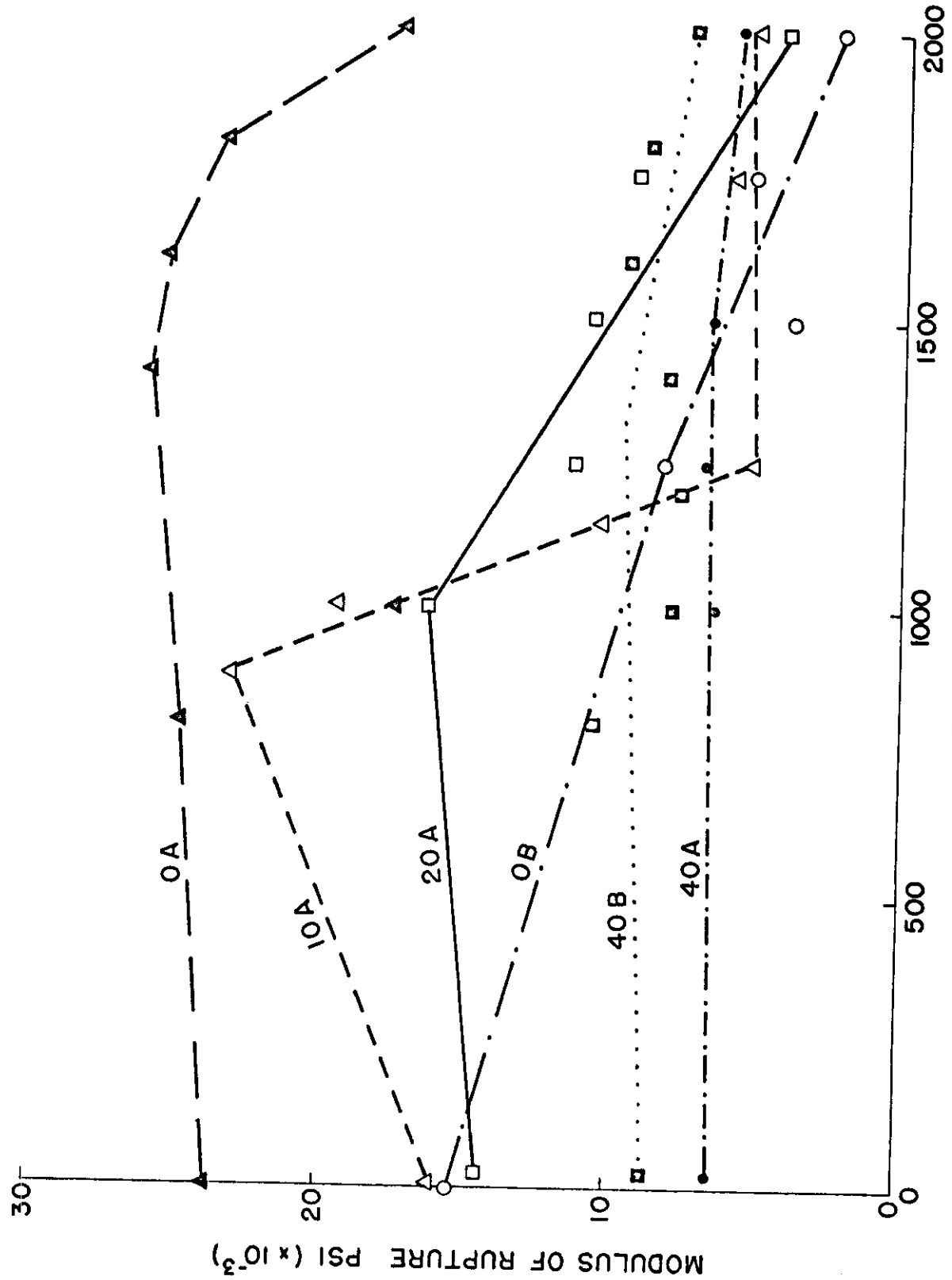

Figure 26 - Modulus of Rupture at Higher Temperature. (The numbers on the curve refer to the composite).

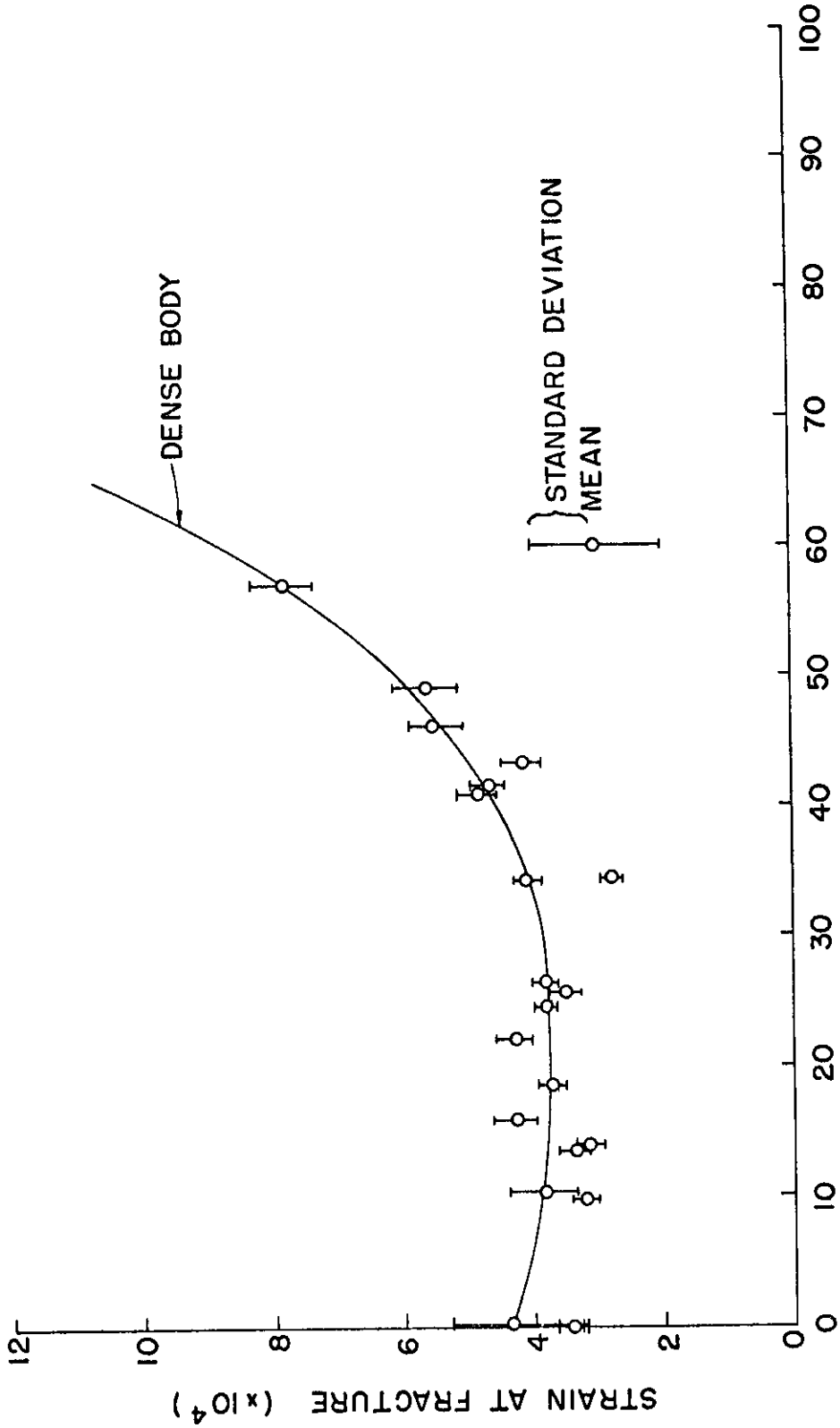

Figure 27 - Strain at Fracture at Room Temperature Perpendicular to the Hot Pressing Direction as a Function of Volume Content Graphite.

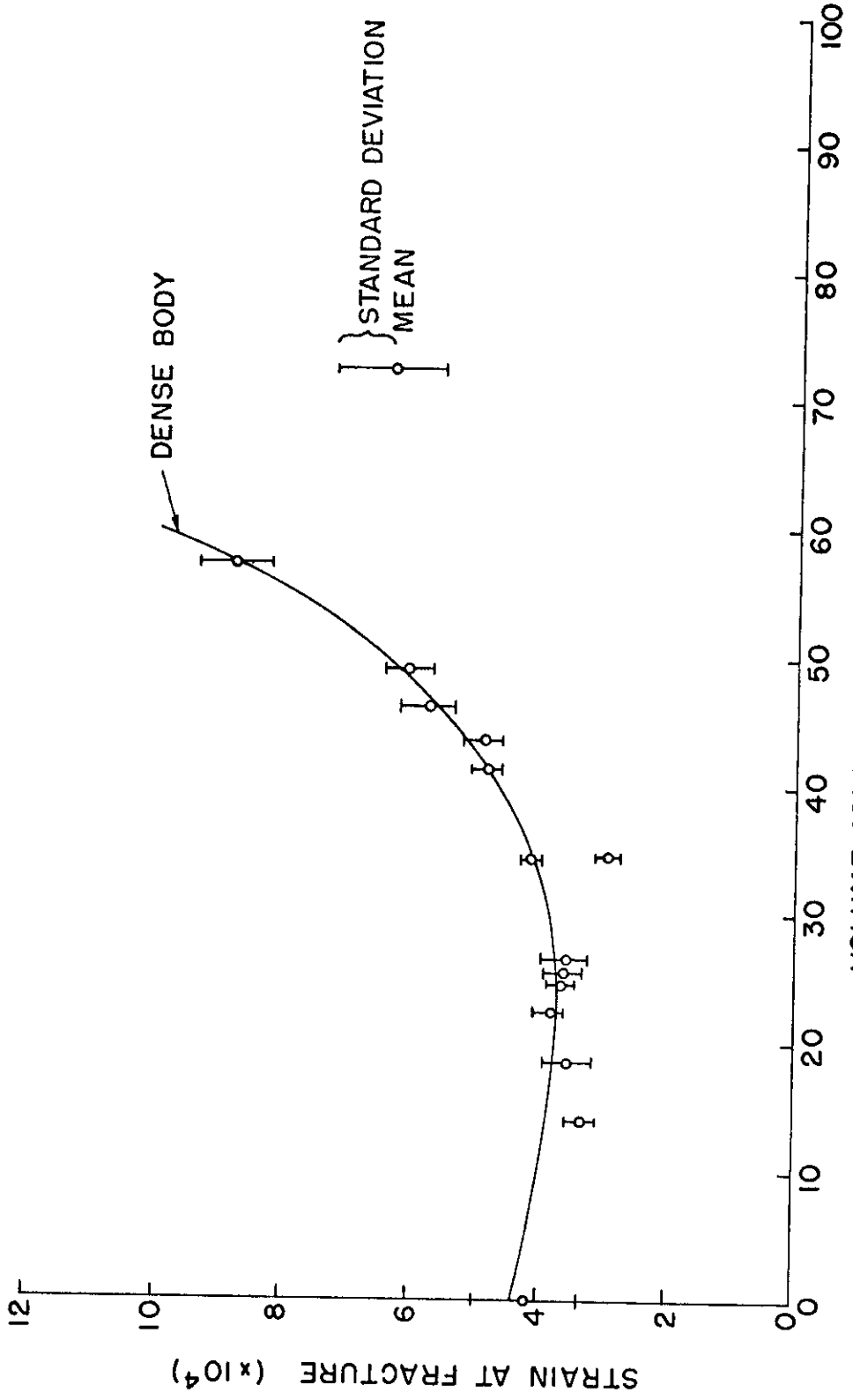

Figure 28 - Strain at Fracture at Room Temperature Parallel to the Hot Pressing Direction as a Function of Volume Content Graphite.

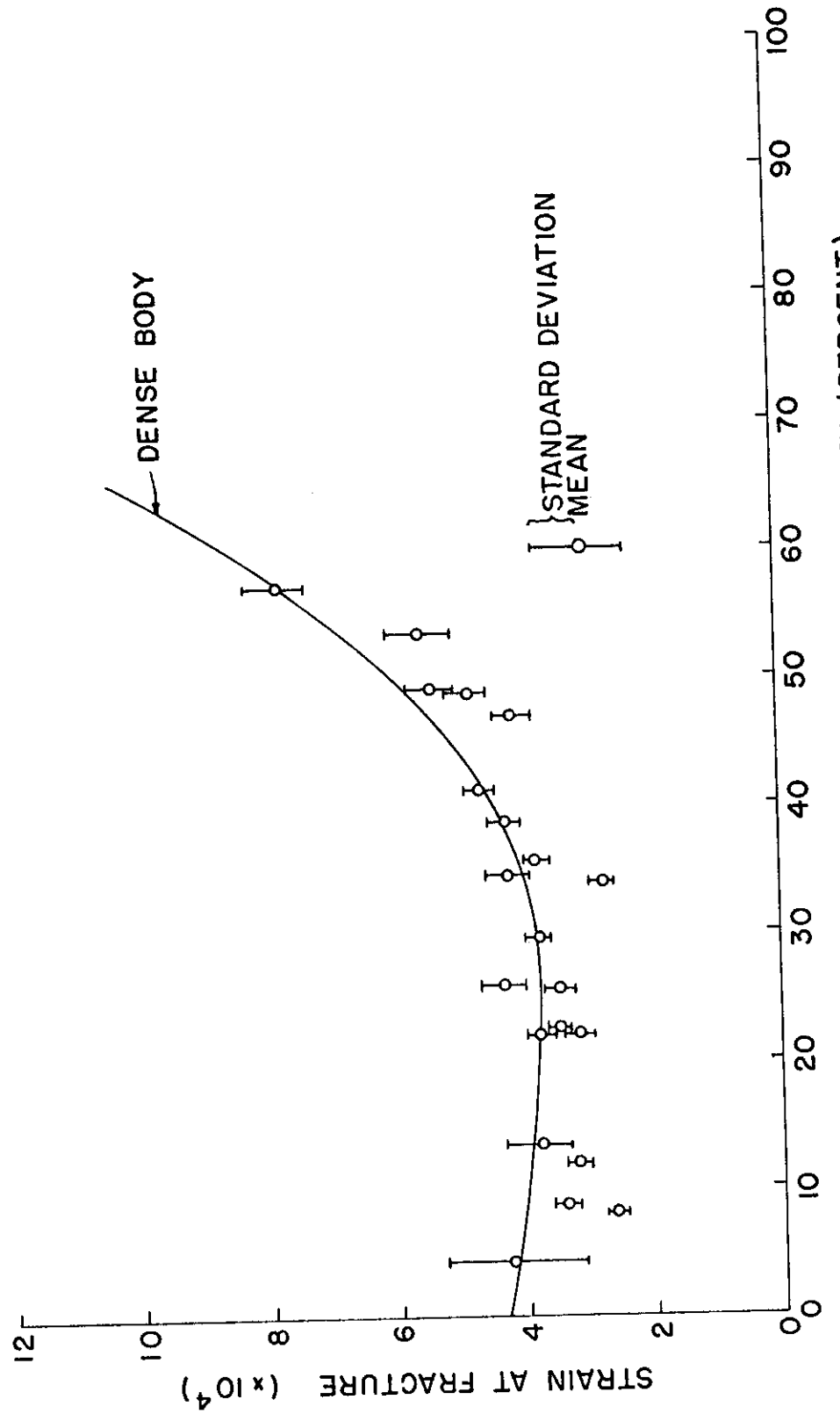

Figure 29 - Strain at Fracture at Room Temperature Perpendicular to the Hot Pressing Direction as a Function of Volume Content Graphite Plus Porosity.

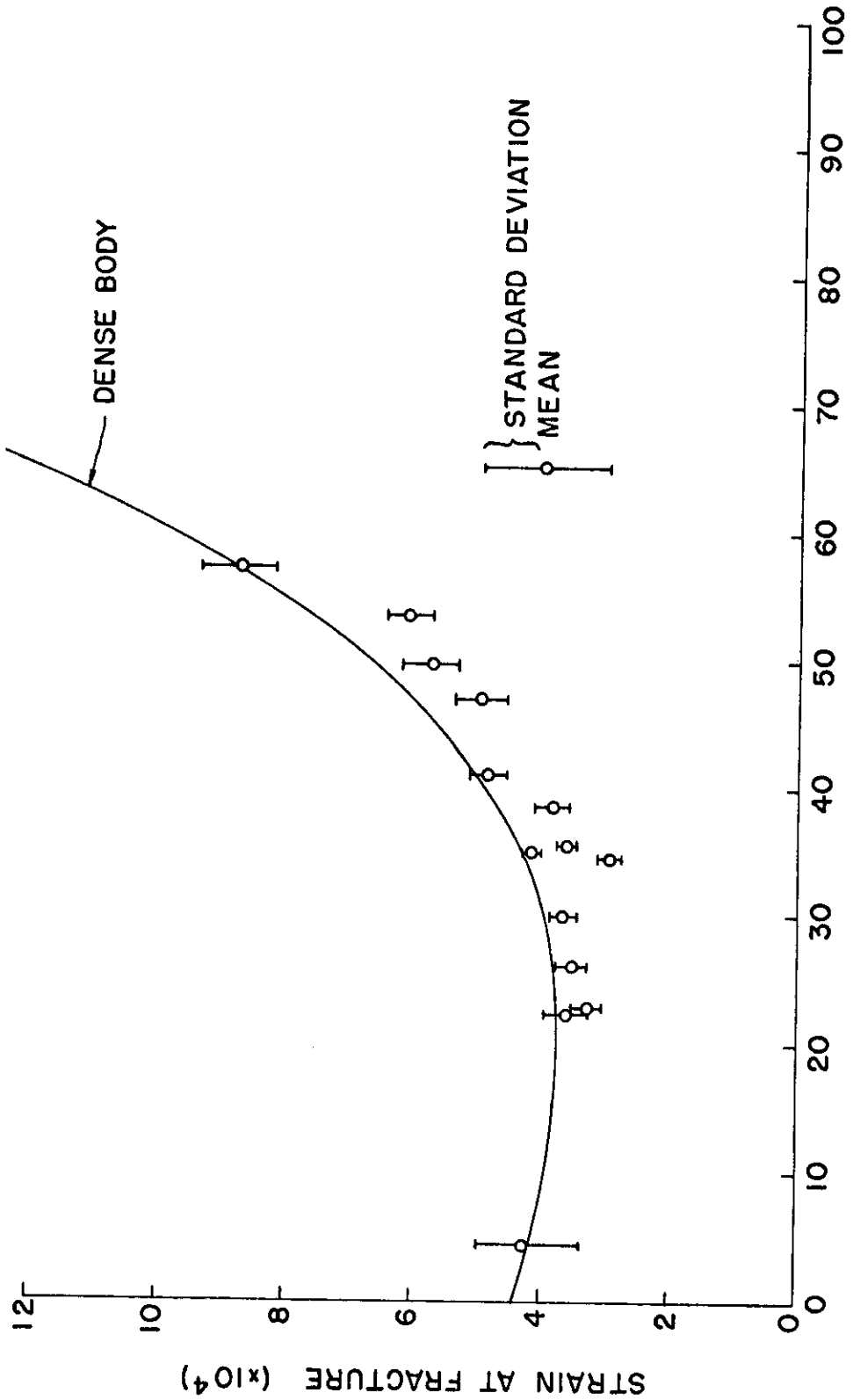

Figure 30 - Strain at Fracture at Room Temperature Parallel to the Hot Pressing Direction as a Function of Volume Content Graphite Plus Porosity.

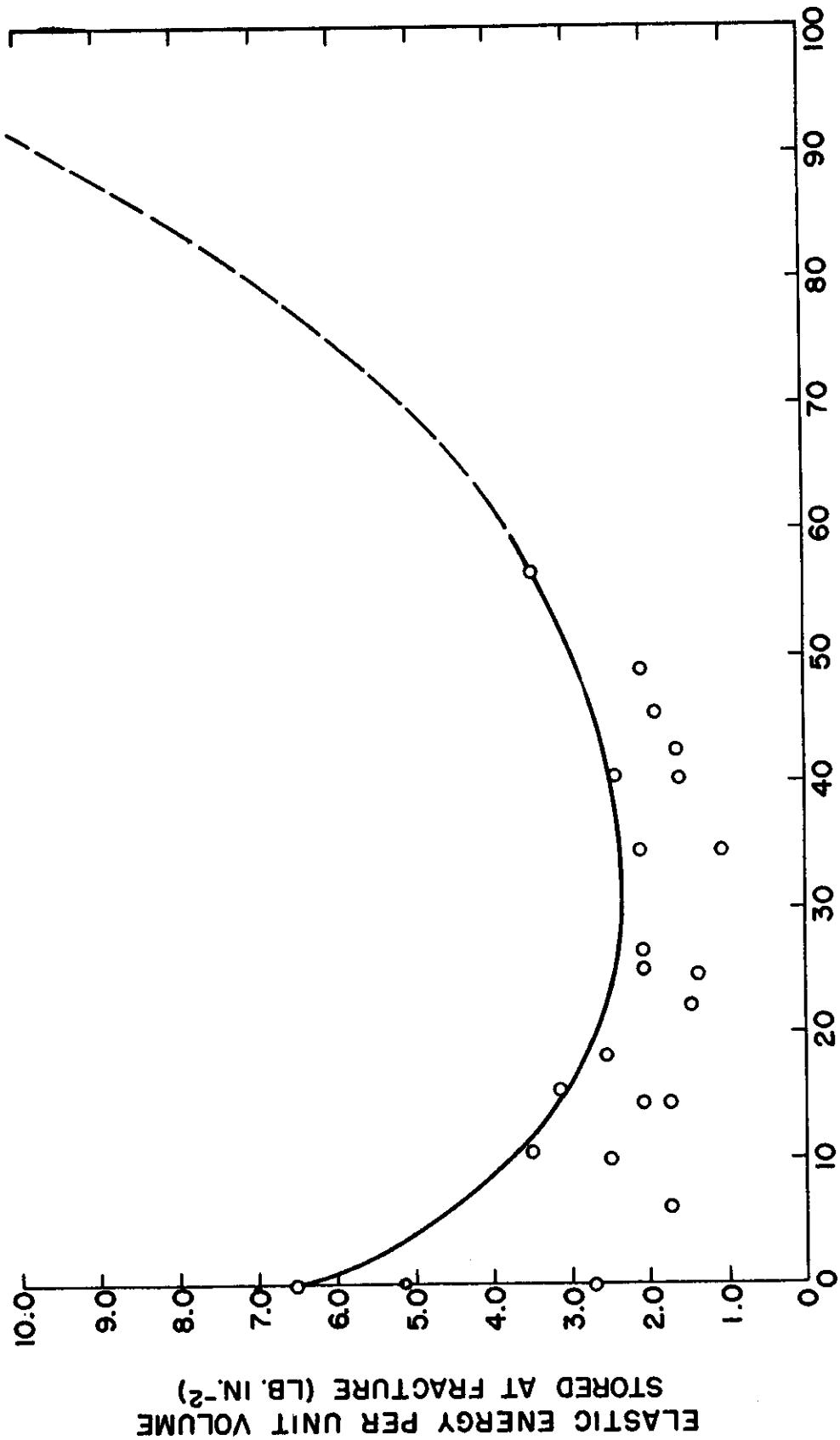

Figure 31 - Elastic Energy Stored at Fracture Perpendicular to the Hot Pressing Direction.

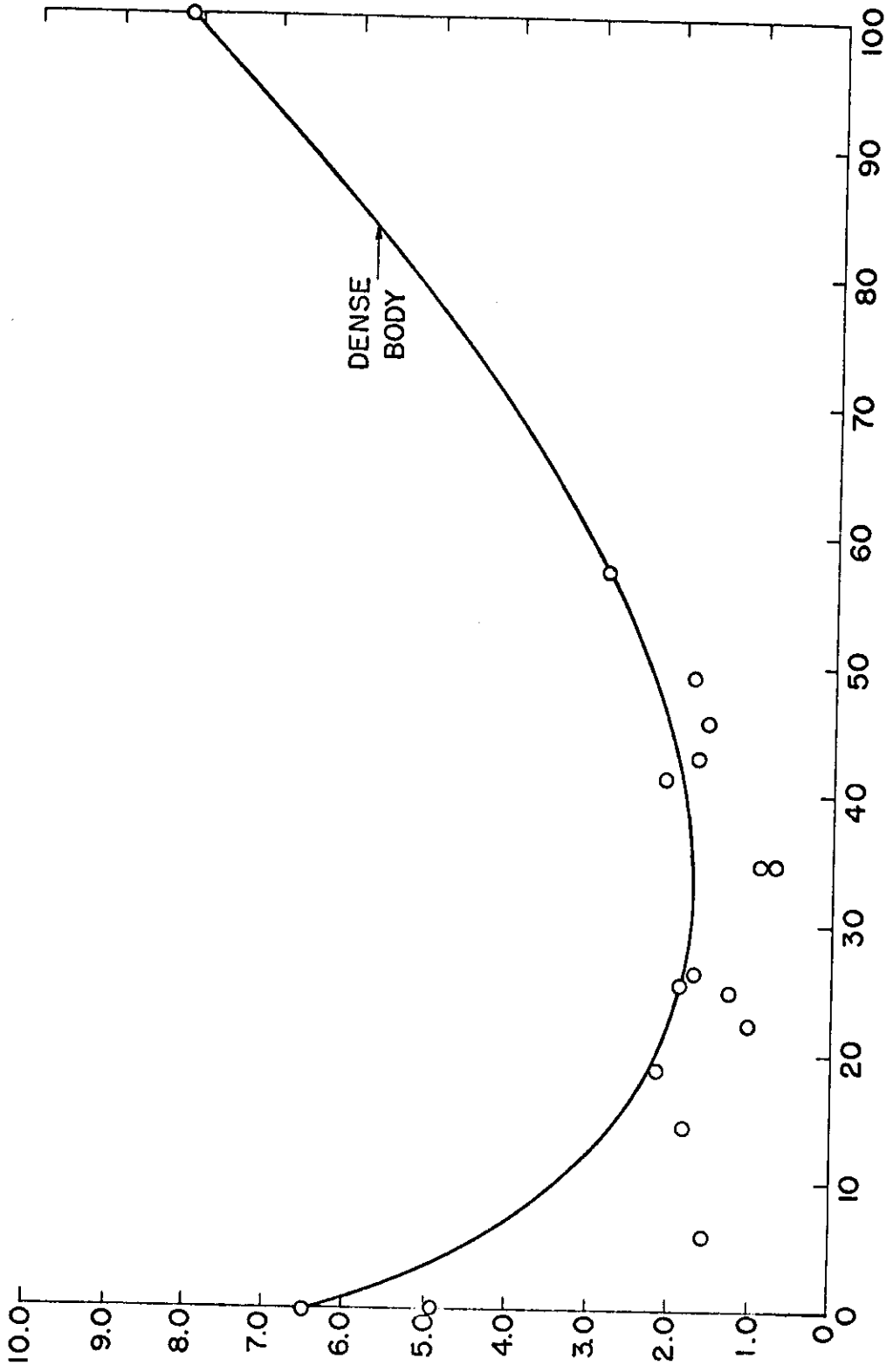

Figure 32 - Elastic Energy Stored at Fracture Parallel to the Hot Pressing Direction.

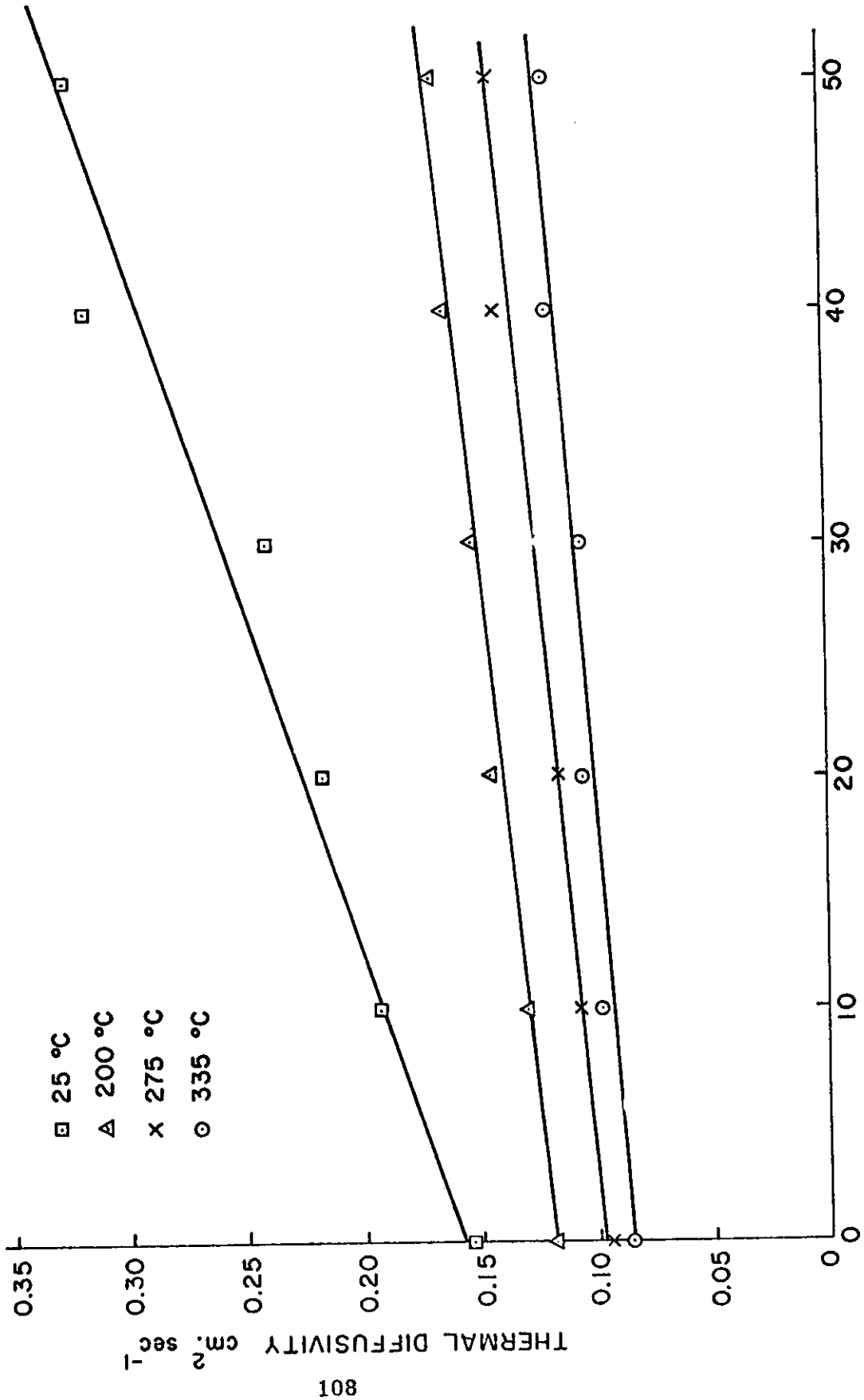

Figure 33 - Thermal diffusivity as a Function of Volume Content Graphite and Temperature.

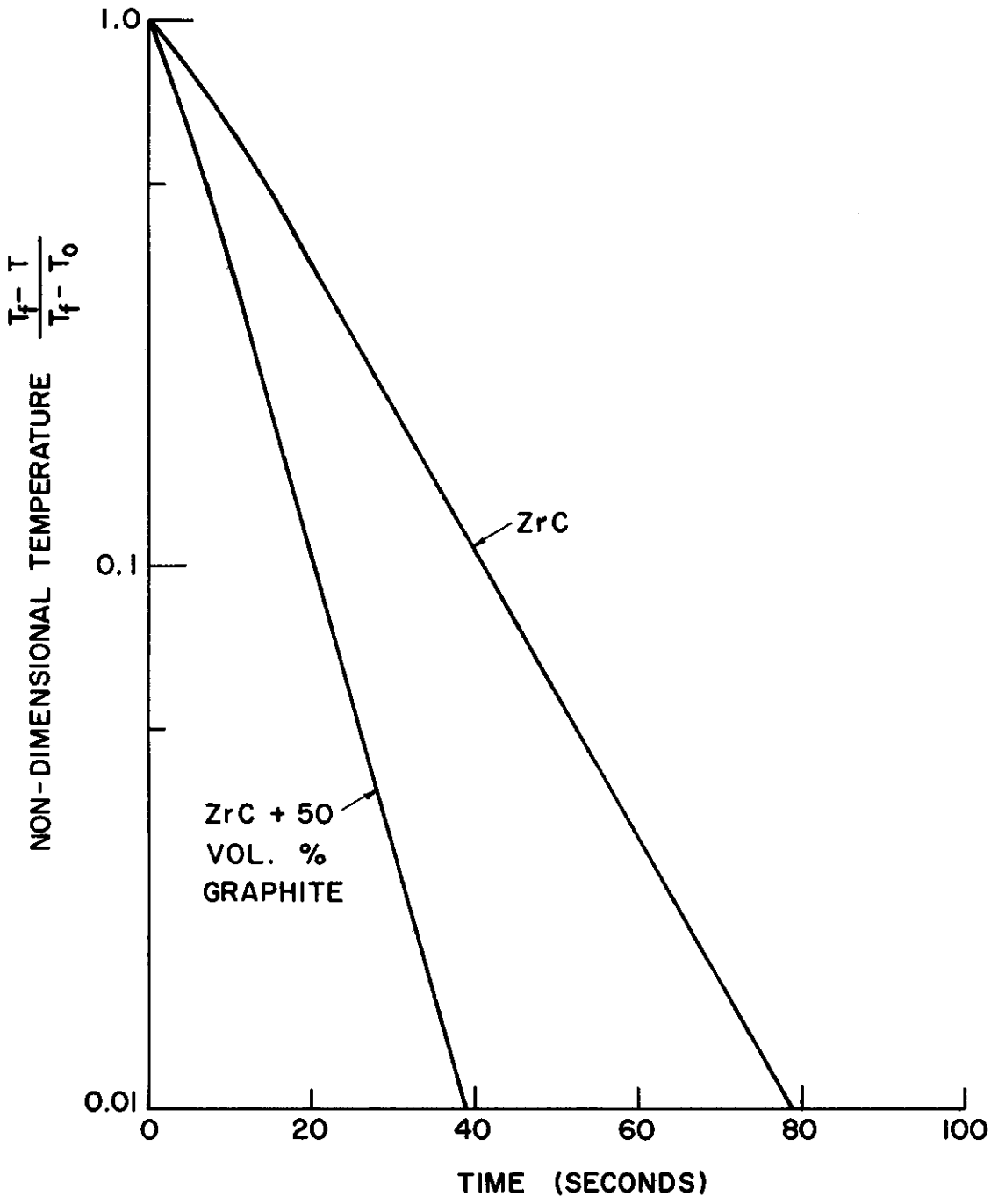

Figure 34 - Transient Temperature at Center of Composite Spheres.

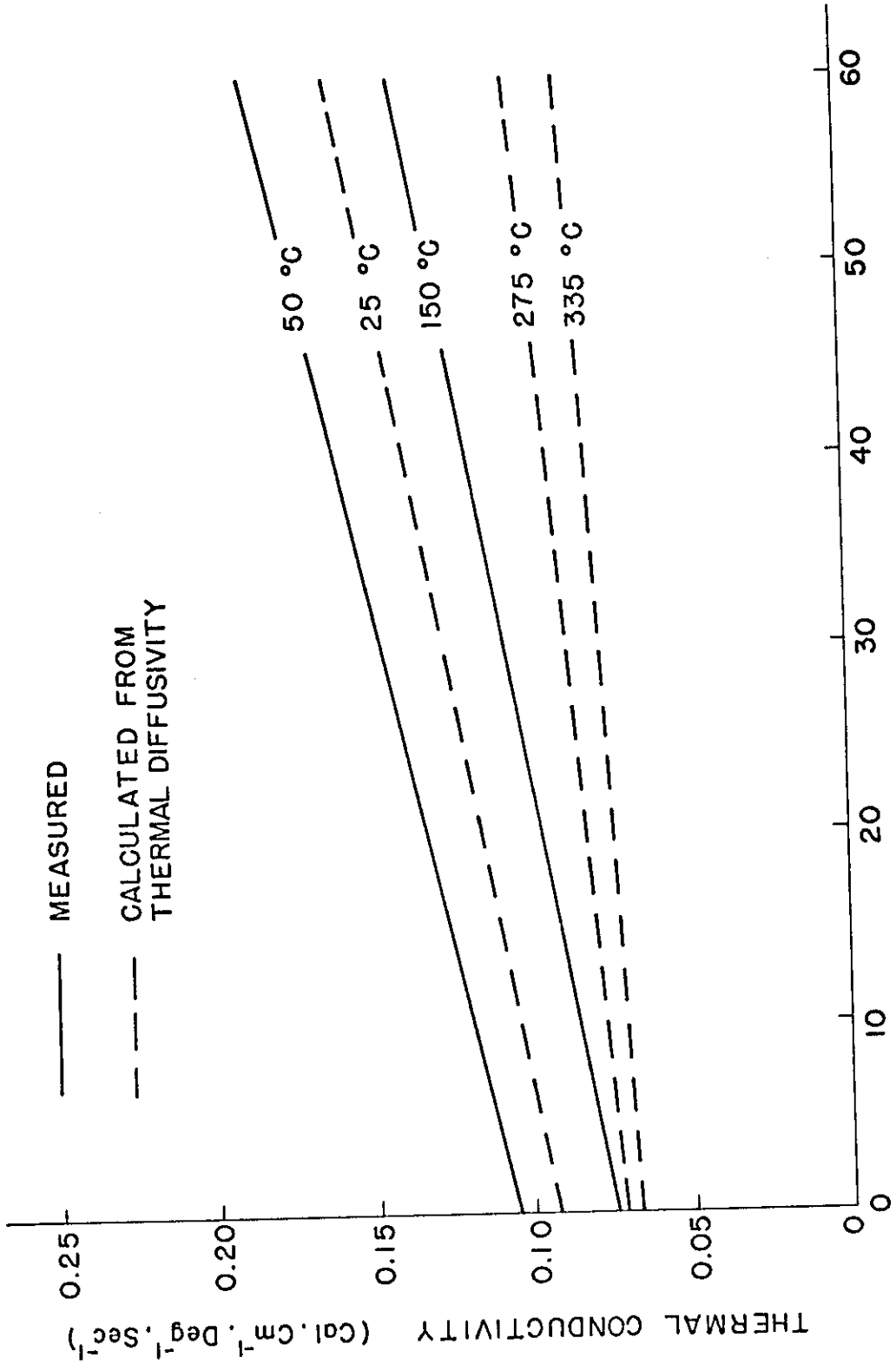

Figure 35 - Thermal Conductivity.

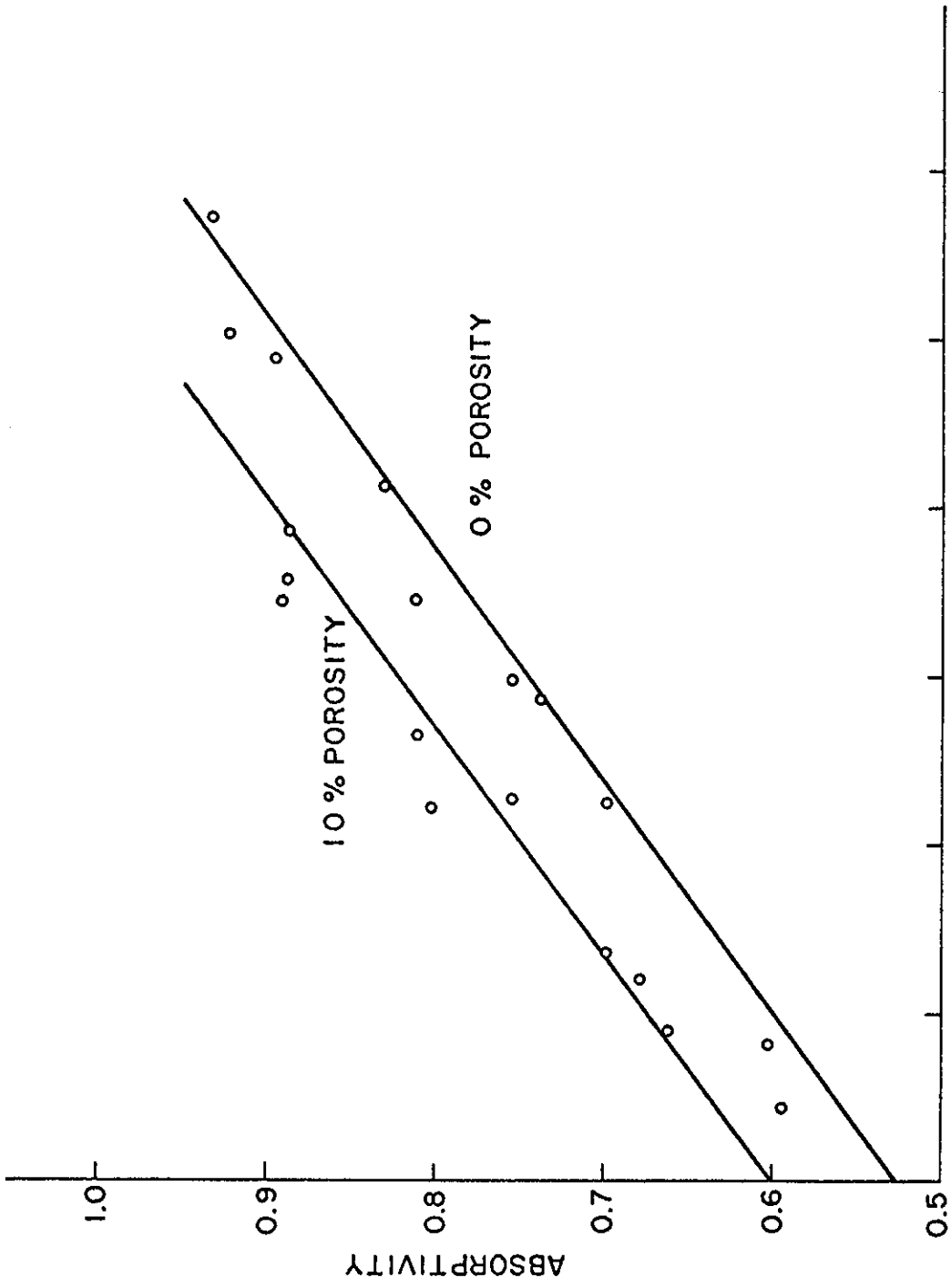

Figure 36 - Total Normal Absorptivity at Room Temperature for Incandescent Radiation.

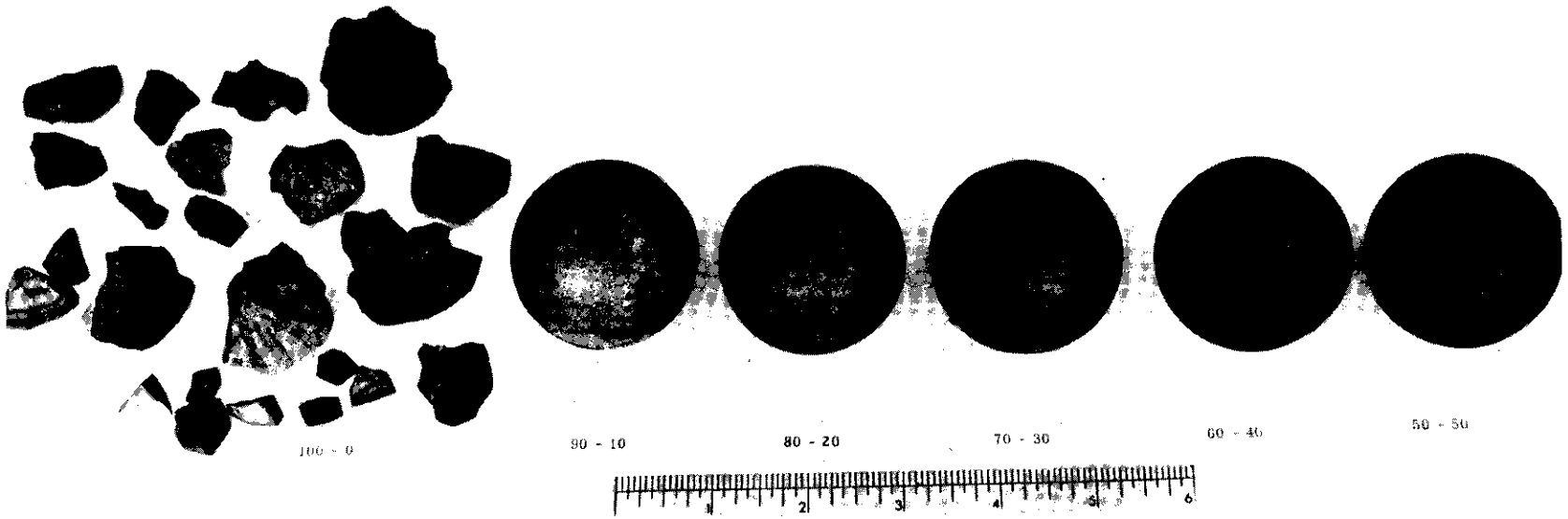

Figure 37 - Spheres of Zirconium Carbide-Graphite Subjected to Thermal Shock at 2000°C. Markers indicate volume percent.

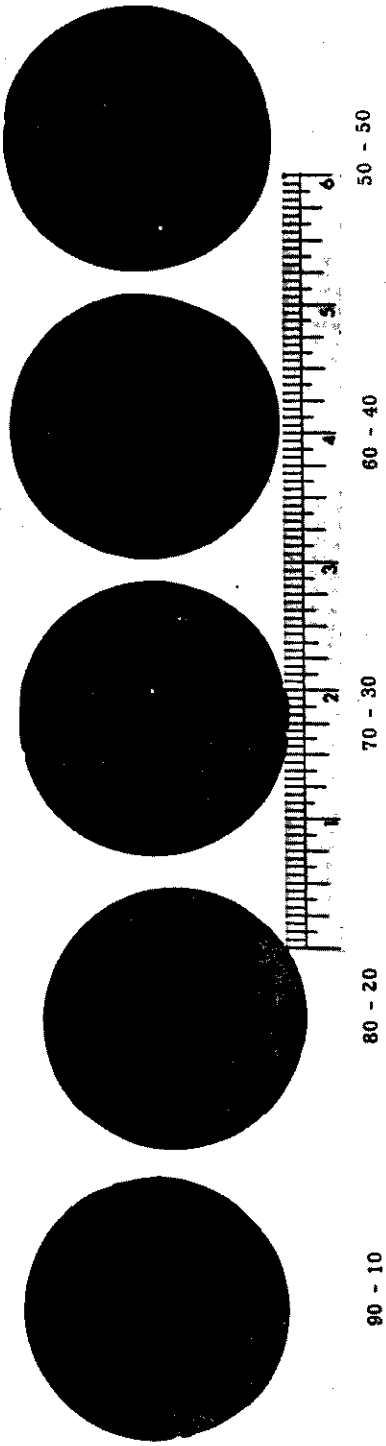

Figure 38 - Spheres of Zirconium Carbide-Graphite From Figure 37 Dissected to Show Internal Fracture.

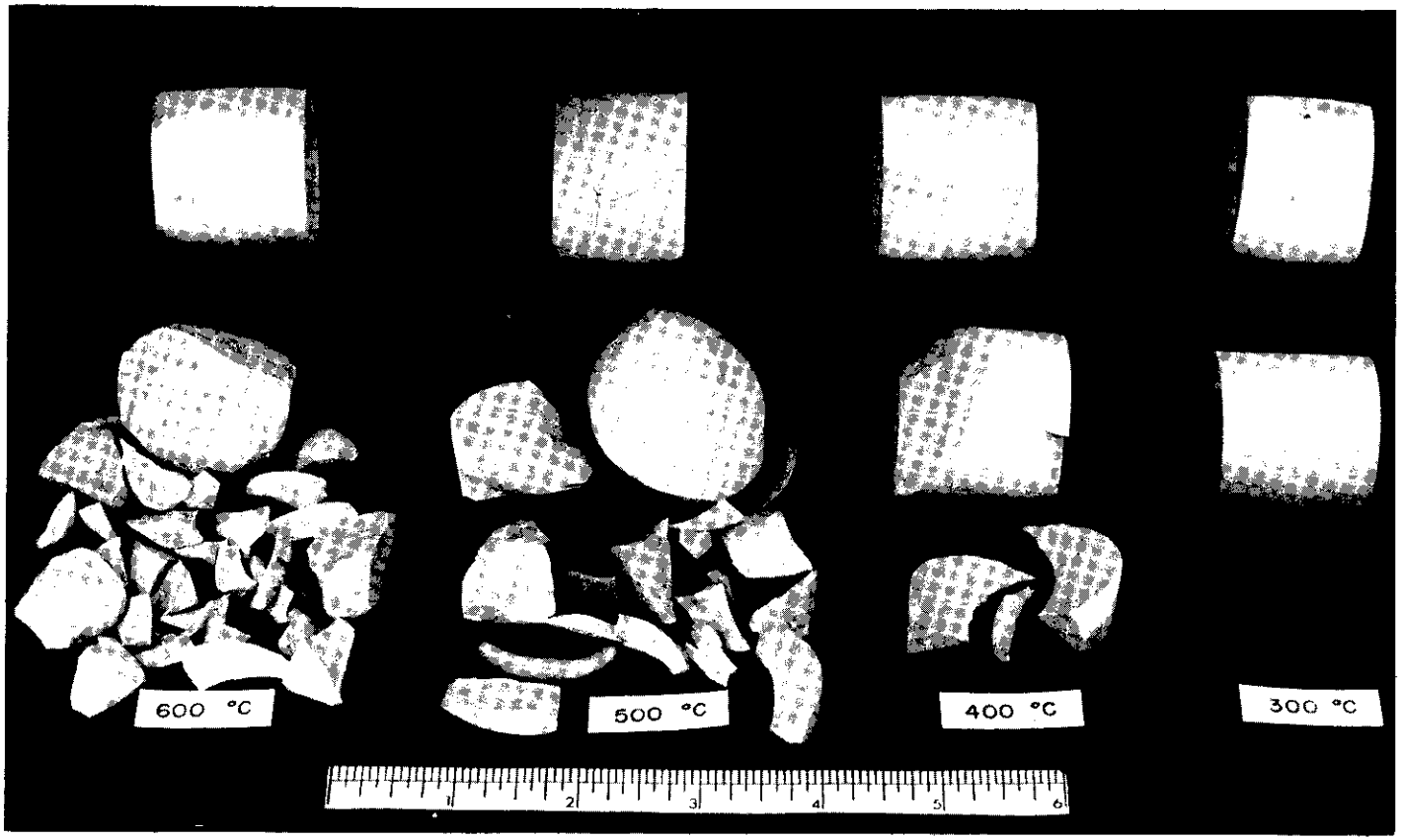

Figure 39 - Cylinders of Alumina (front row) and Alumina Plus Twenty-Five Weight Percent Zirconia Subjected to Thermal Shock in Salt Bath. (Markers indicate temperature of salt bath).

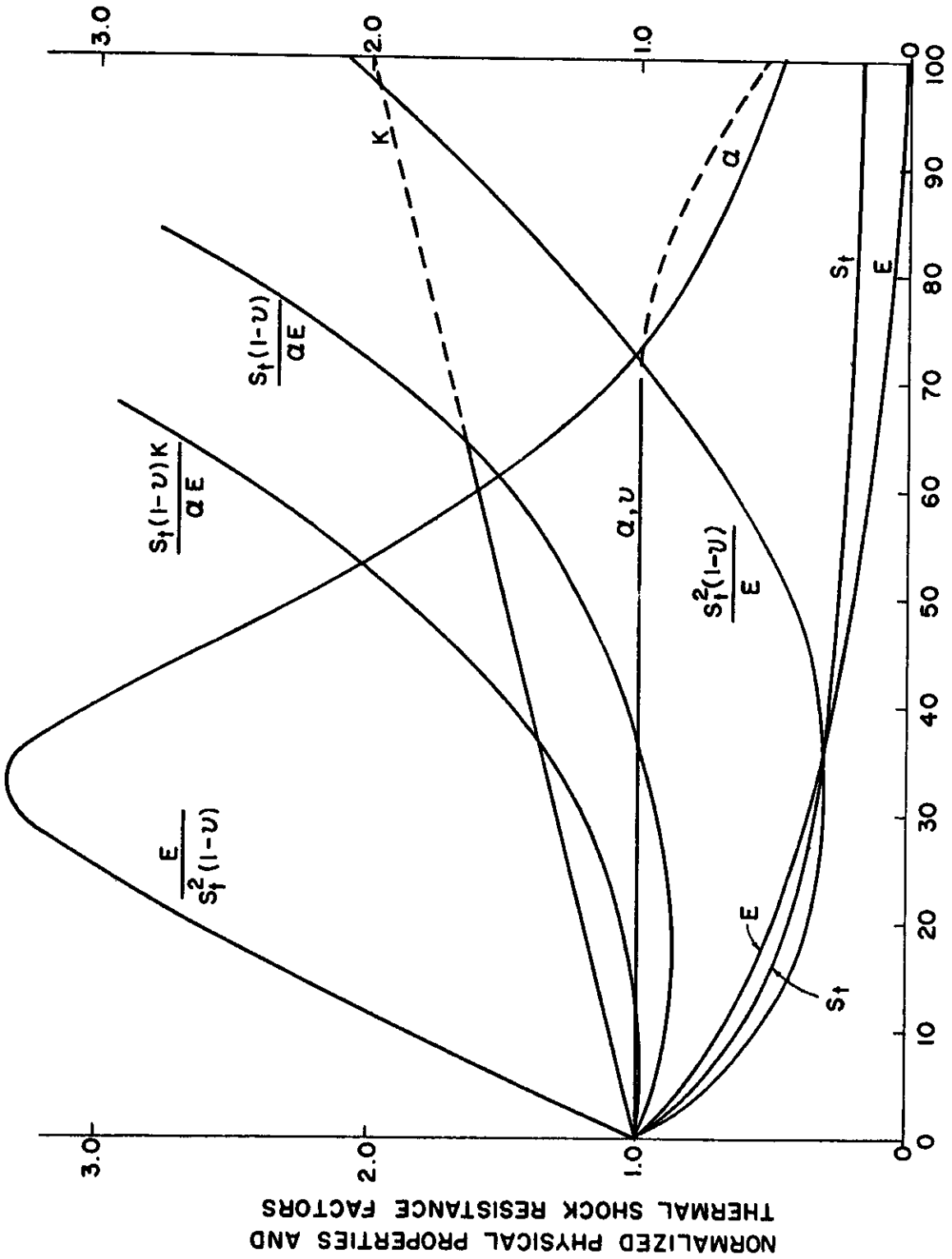

Figure 40 - Normalized Physical Properties and Thermal Shock Resistance Factors.

APPENDIX A

CALCULATION OF ELASTIC ENERGY STORED AT FRACTURE IN A SPHERE SUBJECTED TO THERMAL SHOCK ON HEATING AT A CONSTANT HEAT FLUX

The radial (σ_r) and tangential stresses (σ_θ) at the time of fracture in a sphere subjected to thermal shock on heating at a constant heat flux can, to a good approximation, be given by (See Appendix B):

$$\sigma_r = \frac{2 \alpha E}{5 (1-\upsilon)} \quad \frac{qb}{k} \left[1 - \frac{r^2}{b^2} \right] \tag{53}$$

and

$$\sigma_\theta = \frac{2}{5} \quad \frac{\alpha E}{(1-\upsilon)} \quad \frac{qb}{k} \left[1 - \frac{2r^2}{b^2} \right] \tag{54}$$

where
- α = coefficient of thermal expansion
- E = Young's modulus of elasticity
- υ = Poisson's ratio
- q = heat flux
- b = sphere radius
- k = thermal conductivity
- r = radial coordinate

Assuming fracture to occur under tension, the maximum tensile stress occurs at r = 0. At fracture the stress equals the tensile strength (S_t) of the material. Substitution of tensile strength for the stress in (53) and (54) yields the condition:

$$S_t = \frac{2}{5} \quad \frac{\alpha E}{1-\upsilon} \quad \frac{qb}{k} \tag{55}$$

Substitution of (55) into (53) and (54) yields expressions for the radial and tangential stress at fracture as a function of the tensile strength of the material given by:

$$\sigma_r = S_t \left[1 - \frac{r^2}{b^2} \right] \tag{56}$$

and

$$\sigma_\theta = S_t \left[1 - \frac{2r^2}{b^2} \right] \tag{57}$$

The elastic energy content of the sphere (W) is given by[39]:

$$W = \frac{1}{2E} \int_0^b \left[\sigma_r^2 + 2\sigma_\theta^2 - 2\upsilon (2\sigma_r\sigma_\theta + \sigma_\theta^2) \right] 4\pi r^2 dr \quad (58)$$

Substituting of (56) and (57) and integration yields:

$$W = \frac{4\pi}{7} \frac{S_t^2 b^3 (1 - \upsilon)}{E} \quad (59)$$

The elastic energy stored at fracture is, therefore, proportional to the volume of the sphere and the material factor $S_t^2(1 - \upsilon)/E$.

APPENDIX B

THERMAL SHOCK BY RADIATION

Symbols:

α	Coefficient of thermal expansion
a	Thermal diffusivity
b	Radius of sphere or cylinder, half thickness of flat plate
E	Young's modulus of elasticity
ϵ	Emissivity (or absorptivity) of surface
k	Thermal conductivity
q	Rate of heat flux
q_o	Initial rate of heat flux at T = 0^oK
q_{max}	Maximum heat flux to which a body can be subjected without fracture
r, θ, z	Cylindrical coordinates
R^{IV}	Thermal stress resistance factor for thermal shock by radiation
ρ	Stefan-Boltzmann constant = 1.37×10^{-12} cal. $deg.^{-4}$ $cm.^{-2}$ $sec.^{-1}$
S_{ts}	Tensile strength
σ	Stress
σ^*	Non-dimensional stress $\frac{\sigma(1-\upsilon)}{\alpha E}$
T	Temperature
T_{max}	Maximum temperature to which body can be subjected without fracture
t	Time
$t_{0.95}$	Value of time for stress to reach ninety-five percent of value at $t = \infty$
υ	Poisson's ratio
x, y, z	Rectangular coordinates

I. INTRODUCTION

The usual quantitative treatment of the thermal shock resistance of ceramic materials is based on convective or liquid boundary conditions with constant heat transfer coefficient. For these cases, exact analytical solutions for the transient temperature are available in the literature or can be derived. The calculations of the maximum thermal stresses which occur, therefore, do not present great difficulty.

In many cases of the transfer heat, however, thermal radiation (hereafter referred to as radiation) contributes appreciably to the total amount of heat transferred. For instance, calculations by Heilman[40] show that for a commercial rough steel pipe (emissivity 0.95) with a surface temperature of 550°C, surrounded by an ambient temperature of 25°C, the heat loss by radiation amounts to 86 percent of the total heat loss. The remaining 14 percent is lost due to natural convection. The temperature at which radiation accounts for roughly one-half of the total heat transmission depends on such factors as the emissivity of the surface or the magnitude of the convection coefficient[41]. For large pipes losing heat by natural convection this is room temperature, for fine wires of low emissivity, it is above a red heat. In many thermal shock tests employing both radiation and convection as the mechanism of heat transfer, considerably higher temperatures are often employed. Due to the rapid increase of the heat transfer by radiation with temperature, the contribution of natural convection to the total heat flux decreases rapidly. In case of the thermal shock tests by Crandall and Ging[5], which consisted of heating alumina spheres in air, it may be calculated by means of equations given by Heilman[40] (assuming an emissivity of alumina = 0.80) that at the temperatures employed (1000°C - 1200°C) natural convection contributed less than ten percent to the total heat flux. Heating of the spheres occurred chiefly by radiation. Therefore, in the case of thermal shock tests, which employ temperatures in excess of say 1000°C, heat transfer by convection to a first approximation can be neglected. A need, therefore, exists for a quantitative treatment of the thermal shock resistance of ceramic materials heated or cooled by radiation. One of the major difficulties in obtaining solutions for the transient temperatures due to heating or cooling by radiation is that the boundary conditions are temperature dependent. This leads to non-linear integral equations which can only be solved by means of numerical analysis. As far as the authors are aware no solutions for the transient temperatures in a body heated or cooled by radiation has ever appeared in the literature.

It is the purpose of this appendix to show that for thermal shock of a body at low initial temperature subjected to radiation from high temperature that to a good approximation solutions for the thermal stresses can be obtained by regarding the body to be subjected to a constant heat flux. Expression for the maximum temperature to which the body can be subjected without fracturing can then be derived.

II. THEORY

Heat transfer by radiation between two bodies at different temperatures generally depends on the deometry and size of the individual bodies and involves a so-called "view factor"[41]. For reasons of simplicity in the following discussion, the body subjected to thermal shock by radiation will be considered to be completely enclosed by the body emitting radiation. This corresponds closely to actual conditions employed in the usual thermal shock tests. In addition, the emissivity of the body will be considered to be independent of temperature and wave-length. Also, the material is considered to be opaque.

The net heat flux (q) at the surface of the body at temperature T_1 surrounded by an enclosure at temperature T_2 is given by:

$$q = (T_2^4 - T_1^4) \tag{60}$$

Equation (60) can be written in the form:

$$q = q_o \left[1 - \left(\frac{T_1}{T_2} \right)^4 \right] \tag{61}$$

or

$$q/q_o = 1 - \left(\frac{T_1}{T_2} \right)^4 \tag{62}$$

The ratio q/q_o represents the heat flux at temperature T_1 relative to the heat flux at $T_1 = 0^oK$. Similarly, the ratio T_1/T_2 is the relative temperature of the surface with respect to the temperature of the enclosure. Equation (62) is shown graphically in Figure 41 of this appendix. It may be noticed that the heat flux remains virtually constant up to relatively high values of relative surface temperature. The heat flux has decreased only about five percent when the relative surface temperature has reached a value of approximately 0.475. The solution of the initial part of the transient temperature equation for heating by radiation with low initial body temperature can, therefore, be treated as a constant heat flux problem, and up to a relative surface temperature of 0.475 this assumption will introduce an error of less than five percent.

In case of thermal shock of small bodies in a medium of constant heat transfer coefficient, the maximum stress occurs at relative surface temperatures of approximately 0.2 to 0.3 (See Appendix C). If a similar situation would prevail in the case of thermal shock by means of a constant heat flux, this would offer a solution for thermal shock by radiation. This was investigated in detail for simple shapes; namely, the sphere, the cylinder, and the flat plate.

1. The Sphere

The temperature rise in a sphere with arbitrary initial temperature subjected to a constant heat flux[10] is given by:

$$T(r,t) = \frac{q_o\, b}{k}\left[\frac{3\,at}{b^2} + \frac{5r^2-3b^2}{10b^2} - \frac{2b}{r}\sum_{n=1}^{\infty}\frac{\sin\frac{r\beta_n}{b}}{\beta_n^2\sin\beta_n}e^{-\frac{at\beta_n^2}{b^2}}\right] \tag{63}$$

where $\beta_n, n = 1, 2, 3\ldots$ are the roots of $\tan\beta = \beta$ (64)

The radial and tangential thermal stresses[42] are given by:

$$\sigma_r^* = 2\left[\frac{1}{b^3}\int_o^b Tr^2dr - \frac{1}{r^3}\int_o^r Tr^2dr\right] \tag{65}$$

and

$$\sigma_\theta^* = \frac{2}{b^3}\int_o^b Tr^2dr + \frac{1}{r^3}\int_o^r Tr^2dr - T \tag{66}$$

Substitution of (63) into (65) and (66) yields:

$$\sigma_r^* = \frac{q_o b}{5k}\left[1 - \frac{r^2}{b^2} - \frac{20b^3}{r^3}\sum_{n=1}^{\infty}\frac{\sin\frac{r\beta_n}{b} - \frac{r\beta_n}{b}\cos\frac{r\beta_n}{b}}{\beta_n^4\sin\beta_n}e^{-\frac{at\beta_n^2}{b^2}}\right] \tag{67}$$

and

$$\sigma_\theta^* = \frac{q_o b}{5k}\left[1 - \frac{2r^2}{b^2} - \frac{10b^3}{r^3}\sum_{n=1}^{\infty}\frac{\left\{1 - \frac{r^2\beta_n^2}{b^2}\right\}\sin\frac{r\beta_n}{b} - \frac{r\beta_n}{b}\cos\frac{r\beta_n}{b}}{\beta_n^4\sin\beta_n}e^{-\frac{at\beta_n^2}{b^2}}\right] \tag{68}$$

These stresses are a maximum in tension at r = 0 and are given by:

$$\sigma_r^* = \sigma_\theta^* = \frac{2q_o b}{k}\left[\frac{1}{10} + \frac{2}{3}\sum_{n=1}^{\infty}\frac{1}{\beta_n \sin\beta_n} e^{+\frac{at\beta_n^2}{b^2}}\right] \tag{69}$$

The equation for the maximum tensile stress can be seen to consist of a constant term and a transient term which will decrease with time. Let us define a stress value ($\sigma^*_{0.95}$), which is ninety-five percent of the stress value at time equal infinity. Solving equation (69), the stress($\sigma^*_{0.95}$) can be calculated to occur at a value of time ($t_{0.95}$)

$$t_{0.95} = \frac{0.169b^2}{a} \tag{70}$$

The surface temperature $T(b_1, t_{0.95})$ can now be calculated to be

$$T(b, t_{0.95}) = 0.707\ \frac{q_o b}{k} \tag{71}$$

Similarly, the tensile stress at this value of time

$$\sigma^*(0, t_{0.95}) = 0.190\ \frac{q_o b}{k} \tag{72}$$

Since the value of $T(b, t_{0.95})$ and $\sigma^*(0, t_{0.95})$ depend on the numerical value of T_2, a numerical example may be selected for illustration. Suppose a two-inch diameter sphere of dense alumina, which has the following typical mechanical and thermal properties, is subjected to radiation from 1500°K.

$k = 0.050$ cal. deg^{-1}. cm^{-1}. $sec^{-1}C$
$\epsilon = 0.80$
$\alpha = 7.0 \times 10^{-6}\ deg^{-1}$
$E = 60 \times 10^6$ psi
$\nu = 0.25$

Substitution of these values in (71) and (72), and remembering

$$\sigma^* = \frac{\sigma(1-\nu)}{\alpha E} \tag{73}$$

the following values are found:

$$T(b, t_{0.95}) = 199 \text{ degrees K} \tag{74}$$

and

$$\sigma(0, t_{0.95}) = 29{,}900 \text{ psi} \tag{75}$$

The temperature of the surface has, therefore, risen approximately 200°K. Even if the initial temperature of the sphere was taken at room temperature the surface temperature would be approximately 500°K. This corresponds to a relative surface temperature of approximately 0.333. Therefore, the heat flux from the start of the thermal shock to the time for the stress to reach ninety-five percent of its value at time infinity has decreased by less than two percent. The value of the tensile stress for this example is relatively high and probably exceeds the tensile strength of this material. Fracture probably would have occurred.

If for the same mechanical properties a value of thermal conductivity was selected of only one-half the value, or if the radius selected was twice the value of the radius assumed, a surface temperature of 700°K would have resulted, or a relative surface temperature of approximately 0.467. The calculated stresses, however, would be approximately 59,800 psi. Fracture would, therefore, have occurred long before the surface temperature reached the calculated value.

From the above example it is clear that at low temperature the thermal shock problem of heating by radiation from high temperatures can be treated as a problem involving constant heat flux. The error introduced will be no more than five percent.

By setting the maximum stress allowed equal to the tensile strength, the maximum heat flux (q_{max}), or maximum radiation temperature (T_{max}) to which the body can be subjected can be derived.

From equation (69) the maximum stress is given by:

$$\sigma_r = \frac{q_o b \alpha E}{5k\,(1-\upsilon)} \tag{76}$$

When the maximum stress equals the tensile strength (76) becomes:

$$S_{ts} = \frac{q_{max}\, b \alpha E}{5k\,(1-\upsilon)} \tag{77}$$

where $q_{max} = \rho \epsilon\, (T_{max}^4 - T_1^4)$ (78)

Since $T_1^4 << T_{max}^4$ (78) becomes

$$q_{max} = \rho \epsilon\, T_{max}^4 \tag{79}$$

Substitution of (79) into (77) and rearranging yields, the expression for T_{max} is given by:

$$T_{max} = \left[\frac{5\, S_{ts}\,(1-\upsilon)\,k}{\alpha E \epsilon \rho b}\right]^{1/4} \tag{80}$$

Separating the constants and size factor from the material properties, (80) becomes:

$$T_{max} = \left[\frac{5}{\rho b}\right]^{1/4}\left[\frac{S_{ts}\,(1-\upsilon)\,k}{\alpha E \epsilon}\right]^{1/4} \tag{81}$$

2. The Infinite Cylinder

The rise in temperature(T)for an infinite cylinder with arbitrary initial temperature subjected to a constant heat flux[10] is given by:

$$T = \frac{q_o b}{k}\left[\frac{2at}{b^2} + \frac{r^2}{2b^2} - \frac{1}{4} - 2\sum_{n=1}^{\infty}\frac{J_o\left(\frac{r\beta_n}{b}\right)}{\beta_n^2 J_o(\beta_n)} e^{-\frac{a\beta_n^2 t}{b^2}}\right] \tag{82}$$

where β_n with n = 1, 2, 3, 4... are the positive roots of $J_1(\beta) = 0$

The thermal stresses[42] are given by:

$$\sigma_r^* = \frac{1}{b^2}\int_o^b Trdr - \frac{1}{r^2}\int_o^r Trdr \tag{83}$$

$$\sigma_\theta^* = \frac{1}{b^2}\int_o^b Trdr + \frac{1}{r^2}\int_o^r Trdr - T \tag{84}$$

$$\sigma_z^* = \frac{2}{b^2}\int_o^b Trdr - T \tag{85}$$

As in the case of the sphere the maximum tensile stresses occur at r = 0 and are directly given by:

$$\sigma_r^* = \frac{q_o b}{k}\left[\frac{1}{8} + \sum_{n=1}^{\infty} \frac{1}{\beta_n^2 J_o(\beta_n)} e^{-\frac{a\beta_n^2 t}{b^2}}\right] \tag{86}$$

$$\sigma_\theta^* = \frac{q_o b}{k}\left[\frac{1}{8} + \sum_{n=1}^{\infty} \frac{1}{\beta_n^2 J_o(\beta_n)} e^{-\frac{a\beta_n^2 t}{b^2}}\right] \tag{87}$$

$$\sigma_z^* = \frac{q_o b}{k}\left[\frac{1}{4} + 2\sum_{n=1}^{\infty} \frac{1}{\beta_n^2 J_o(\beta_n)} e^{-\frac{a\beta_n^2 t}{b^2}}\right] \tag{88}$$

In this case failure will occur due to the axial tensile stress (σ_z^*) as this stress exceeds both σ_r^* and σ_θ^*.

The time ($t_{0.95}$) for the axial stress to reach ninety-five percent of its final value occurs at

$$t_{0.95} = 0.225 \frac{b^2}{a} \tag{89}$$

The surface temperature at this time is given by:

$$T(b, t_{0.95}) = 0.695 \frac{q_o b}{k} \tag{90}$$

and the axial tensile stress:

$$\sigma_z^*(0, t_{0.95}) = 0.238 \frac{q_o b}{k} \tag{91}$$

Using the same numerical example used in the stress analysis of the sphere gives:

$$T(b, t_{0.95}) = 196 \text{ degrees K} \tag{92}$$

and

$$\sigma(0, t_{0.95}) = 37{,}500 \text{ psi} \tag{93}$$

Comparing (92) and (74) shows that in the case of a cylinder, the stresses have reached ninety-five percent of their final value at a surface temperature lower than the sphere subjected to the same thermal shock. Stresses in the cylinder are considerably higher than in the sphere, and fracture probably would have occurred before the surface reached this temperature. Therefore, as in the case of the sphere, the problem of thermal shock by radiation of a cylinder at low initial temperature can be treated as a constant heat flux problem.

By equating the maximum tensile stress allowed in the cylinder to the tensile strength of the material, an expression can be derived for the maximum radiation temperature (T_{max}) to which an infinite cylinder can be subjected. Using (88) and following the same procedure used in the thermal stress analysis of a sphere the expression of T_{max} for an infinite cylinder is given by:

$$T_{max} = \left[\frac{4}{\rho b}\right]^{1/4} \left[\frac{S_{ts}(1-\nu)\,k}{\alpha E \epsilon}\right]^{1/4} \tag{94}$$

3. The Infinite Flat Plate

The temperature rise in an infinite flat plate ($-b < z < b$) heated at both faces by a constant heat flux[10] is given by:

$$T = \frac{q_o b}{k}\left[\frac{at}{b^2} + \frac{3z^2 - b^2}{6b^2} - \frac{2}{\pi^2}\sum_{n=1}^{\infty}\frac{(-1)^n}{n^2}\cos\frac{n\pi z}{b}\, e^{-\frac{an^2\pi^2 t}{b^2}}\right] \tag{95}$$

The stresses[42] are given by:

$$\sigma_{xx}^* = \sigma_{yy}^* = \frac{1}{2b}\int_{-b}^{b} T\,dz + \frac{3z}{2b^2}\int_{-b}^{b} Tz\,dz - T \tag{96}$$

The maximum tensile stresses occur at $z = 0$ and are given directly by:

$$\sigma_{xx}^* = \sigma_{yy}^* = \frac{q_o b}{k}\left[\frac{5}{18} - \frac{2}{\pi^2}\sum_{n=1}^{\infty}\frac{1}{n^2}\, e^{-\frac{an^2\pi^2 t}{b^2}}\right] \tag{97}$$

Here the ninety-five percent stress level occurs approximately at:

$$t_{0.95} = 0.318 \frac{b^2}{a} \tag{98}$$

The surface temperature at this time is:

$$T(b, t_{0.95}) = 0.642 \frac{q_o b}{k} \tag{99}$$

Similarly, the tensile stress becomes:

$$\sigma_{xx}^* = \sigma_{yy}^* = 0.264 \frac{q_o b}{k} \tag{100}$$

Again, using the same numerical example used in the analysis of the sphere and the cylinder, gives:

$$T(b, t_{0.95}) = 181 \text{ degrees K} \tag{101}$$

$$\sigma_{xx} = \sigma_{yy} = 41,600 \text{ psi} \tag{102}$$

Here the surface temperature is even lower than in the case of the cylinder or the sphere. The stress is correspondingly higher. Therefore, the thermal shock problem of the flat plate with low initial starting temperature also can be treated as a constant heat flux problem. As for the sphere and infinite cylinder, an expression for T_{max} for an infinite plate can be derived and is given by:

$$T_{max} = \left[\frac{3.6}{\rho b}\right]^{1/4} \left[\frac{S_{ts}(1-\upsilon)\,k}{\alpha E \epsilon}\right]^{1/4} {}^{o}K \tag{103}$$

For a flat infinite plate subjected to radiation at one face only, T_{max} is given by:

$$T_{max} = \left[\frac{3}{\rho b}\right]^{1/4} \left[\frac{S_{ts}(1-\upsilon)\,k}{\alpha E \epsilon}\right]^{1/4} {}^{o}K \tag{104}$$

4. General

From the examples discussed above, it can be concluded that the maximum radiation temperature to which a body can be subjected with low initial temperature to a good approximation is given by:

$$T_{max} = \left[\frac{A}{\rho b}\right]^{1/4} \left[\frac{S_{ts}\,(1-\upsilon)\,k}{\alpha E \epsilon}\right]^{1/4} \quad {}^{o}K \qquad (105)$$

where A depends on geometry only and b is a size factor.

A thermal stress resistance parameter (R^{IV})* can now be defined by:

$$R^{IV} = \left[\frac{S_{ts}\,(1-\upsilon)\,k}{\alpha E \epsilon}\right]^{1/4} \qquad (106)$$

which, in addition to the material properties usually considered in thermal shock theory, also contains the emissivity. From the form of (106) the emissivity of the material plays as important a part in the thermal shock resistance as the other material properties usually considered in thermal shock theory. Therefore, in cases of thermal shock where the major part of the heat transfer takes place by radiation, the importance of the emissivity should not be overlooked. Considerable improvement in the thermal shock resistance will be found if low values of emissivity are obtained. Surface condition plays an important role. Smooth polished surfaces are desired. Since metals have generally lower emissivities than ceramics, improved thermal shock resistance of the ceramics can be obtained by metallizing the surface. The increase in thermal shock resistance of metal fiber reinforced ceramics[34] can at least partly be explained by the fact that the emissivity of the surface has been lowered. The writers suggest that many thermal shock results, especially those obtained by thermal cycling of small modulus of rupture bars, should be re-interpreted in the light of possible differences in the emissivities and surface condition of the materials concerned.

Of significance in the theory developed above is that as long as the initial temperature is kept low, the value of T_{max} is independent of the initial temperature. It is only indirectly a function of the initial temperature because the material properties entering the expression for T_{max} are a function of temperature. Improved thermal shock resistance can be obtained if an initial temperature is chosen so as to maximize R^{IV}. Cooling to liquid nitrogen temperature will increase the thermal conductivity substantially which will result in a considerable increase in T_{max}.

Also of interest is the fact that due to the form of the equation for T_{max} (105), any relative error in one of the physical properties is reduced by a factor of four. Therefore, in the case of thermal shock by radiation it is easier to obtain good agreement with experiment than in the case of thermal

* For the thermal stress parameters R^{I}, R^{II}, R^{III}, R^{V} and R^{VI}, see Discussion.

shock with a constant heat transfer coefficient. In this latter case, any relative error in one of the physical properties introduces the same relative error in the calculated value of the temperature difference required to nucleate fracture. (See, for instance, Appendix C).

In the derivation of the equations for T_{max} for simplicity the geometry selected consisted of a small object at low initial temperature completely contained within an enclosure at high temperature. In this manner only the emissivity of the object being heated enters the final expression for T_{max}. For other geometries, the emissivity in the expression for T_{max} can be replaced by an effective emissivity (ϵ_{eff}) which, in general, will depend on the geometry and the emissivities of the object receiving radiation and on the emissivity of the object emitting radiation. A number of effective emissivities for various geometries are given by Hottel[43].

For two parallel infinite plates facing each other, or in the case where the body receiving radiation is large compared to the enclosure in which it is contained, the effective emissivity is given by:

$$\epsilon_{eff} = \frac{1}{\frac{1}{\epsilon_1} + \frac{1}{\epsilon_2} - 1} \qquad (107)$$

where ϵ_1 is the emissivity of the object receiving radiation and ϵ_2 is the emissivity of the object emitting radiation.

The limitations of the above analysis are that it can be applied to materials of moderate thermal stress resistance only. Materials with high thermal stress resistance will require a high temperature difference within the body in order to have a stress level which approaches the tensile strength. The surface temperature, therefore, may have reached a value where the radiation emitted by the surface can no longer be neglected.

A convenient upper limit may be set such that the heat emitted* by the surface has reached a value of five percent of that absorbed by the surface. This occurs at a relative surface temperature of approximately 0.475. In order to determine whether the theory developed above can be applied to a given situation, the value of T_{max} is calculated by means of the appropriate equation for the geometry concerned. With a knowledge of T_{max} the heat flux can be readily calculated. The surface temperature is then calculated from the equation which gives the surface temperature at the time where the stress has reached ninety-five percent of its limiting value. The ratio of surface

* The heat reflected by the surface is not taken into account.

temperature to T_{max} should be less than 0.475. Examination will reveal that the theory is applicable to most of the conventional ceramics. Care should be taken, however, with those ceramics with low thermal expansion or those with very high strength.

III. EXPERIMENTAL

Very few quantitative data exist in the literature to test the above theories. In the opinion of the writers the most carefully carried out quantitative thermal shock tests were carried out by Crandall and Ging[5]. These investigators subjected high alumina porcelain* spheres of various diameters to thermal shock with initial temperature at room temperature and temperatures required for fracture at approximately 1000°C or higher. These data, therefore, lend themselves quite well to check the theory developed above. The properties of the high alumina porcelain ceramic of which these spheres were composed, as determined by Crandall and Ging[5], are listed in Table No. XXVI. The value for the emissivity was obtained from McAdams[41]. Thermal conductivity was given by Coors**. Since fracture occurs at relatively low temperatures, as shown above, the property values selected correspond to room temperature. The calculated and observed values of T_{max} are shown in Table No. XXVII. The excellent agreement should be noted.

TABLE NO. XXVI

Material Properties of High Alumina Porcelain Ceramic

k	=	0.032 cal. deg^{-1}. cm^{-1}. sec^{-1}
ϵ	=	0.80
α	=	6.1×10^{-6} deg^{-1} C
E	=	31.4×10^{6} psi
S_{ts}	=	19,800 psi
ν	=	0.27

TABLE NO. XXVII

Calculated and Experimental Values of T_{max} (°K) for High Alumina Porcelain

Sphere Diameter (in)		3	2	1-1/2	1-1/4
T_{max}	calculated	1305	1445	1552	1625
T_{max}	observed	1250	1417	1528	1644

* Coors Type AB-2. Coors Porcelain Company, Golden, Colorado.
** Coors Data Sheet 001.

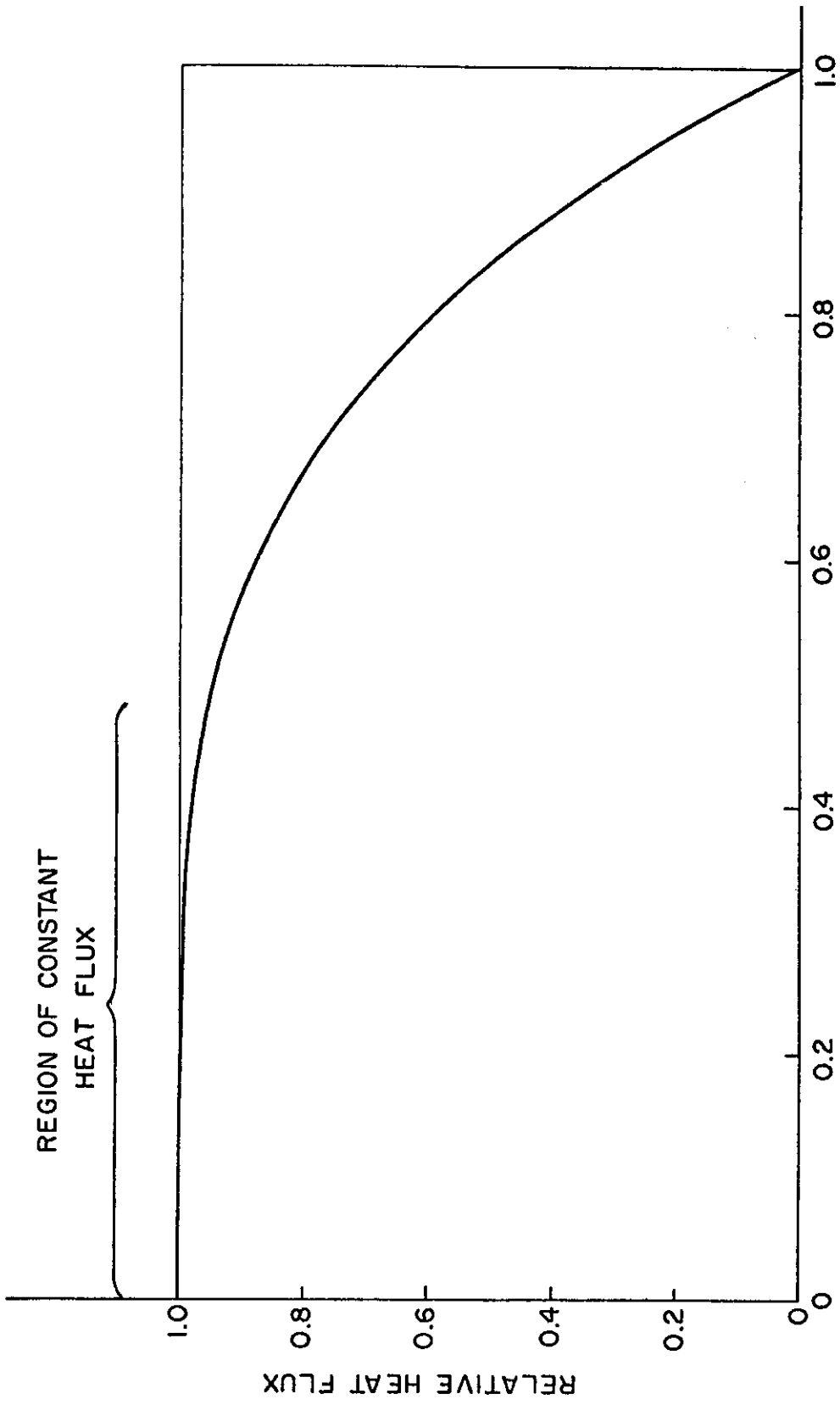

Figure 41 - Heat Flux by Radiation as a Function of Surface Temperature.

APPENDIX C

CALCULATION OF THERMAL STRESSES IN SPHERES SUBJECTED TO THERMAL SHOCK IN A MEDIUM OF CONSTANT HEAT TRANSFER COEFFICIENT AND RECALCULATION OF RESULTS OF CRANDALL AND GING[5]

Symbols:

α	Coefficient of thermal expansion.
a	Thermal diffusivity.
β	Biot's modulus $= \frac{bh}{k}$
b	Radius of sphere.
E	Young's modulus of elasticity.
h	Surface heat transfer coefficient.
k	Thermal conductivity.
r	Radial coordinate.
S_{ts}	Tensile strength.
σ	Stress.
σ^*	Non-dimensional stress $= \frac{\sigma(1-\nu)}{\alpha E \Delta T}$
T_o	Initial temperature of thermal shock test.
T_f	Final temperature of thermal shock test.
ΔT	Temperature difference to which sphere is subjected.
ΔT_{max}	Maximum temperature difference to which sphere can be subjected without fracture or minimum temperature difference required to cause fracture.
t	Time.
θ	Non-dimensional time $= \frac{at}{b^2}$
μ	Non-dimensional transient temperature $= \frac{T_f - T}{T_f - T_o}$
ν	Poisson's ratio.

The non-dimensional transient temperature (μ) in a sphere subjected to a medium with constant surface heat transfer coefficient (h), initial temperature (T_o), and final temperature (T_f), in the notation of Crandall and Ging[5], is given by:

$$\mu = \frac{2\beta b}{r} \sum_{n=1}^{\infty} e^{-\psi_n^2 \theta} \frac{\psi_n^2 + (\beta - 1)^2}{\psi_n^2 \left[\psi_n^2 + \beta(\beta - 1)\right]} \sin \psi_n \sin \frac{r\psi_n}{b} \qquad (108)$$

where ψ_n are the roots of

$$\psi \cot \psi + \beta - 1 = 0 \qquad (109)$$

The radial thermal stresses (σ_r^*) and tangential thermal stress (σ_θ^*)[42] which occur are given by:

$$\sigma_r^* (r,t) = \frac{2}{b^3} \int_o^b \mu r^2 dr - \frac{2}{r^3} \int_o^r \mu r^2 dr \qquad (110)$$

$$\sigma_\theta^* (r,t) = \frac{2}{b^3} \int_o^b \mu r^2 dr - \frac{1}{r^3} \int_o^r \mu r^2 dr - \mu \qquad (111)$$

Substitution of (108) into (110) and (111) yields the stresses as a function of radial coordinates and time. Since brittle ceramic materials subjected to thermal shock generally fail in tension, the maximum tensile stresses are of primary interest. These maximum tensile stresses can be obtained by finding the maximum of equations (110) and (111).

Since the form of equation (108) is rather complex, the numerical evaluation of the maximum stresses becomes rather tedious. Equations (110) and (111), therefore, were programmed for a Univac® electronic computer. Calculated were the maximum tensile stresses which occur for both heating and cooling for various values of Biot's modulus (β). In addition, the non-dimensional time (θ) at which the stresses are a maximum was also computed. From this value of time, the non-dimensional temperature at the center, at the surface and the mean temperature of the sphere at the time of maximum stress were also calculated. During thermal shock on heating the maximum tensile stresses occur at the center of the sphere (r = o). On cooling, the maximum tensile stress occurs at the surface (r = b).

Table No. XXVIII shows the calculated values for the maximum tensile stress, the non-dimensional time and non-dimensional temperature at the time of maximum stress for thermal shock on heating.

Table No. XXIX shows the same values for thermal shock on cooling. Figure 42 shows the maximum stresses for both heating and cooling for various values of Biot's modulus. These values are in agreement with the curves given by Crandall and Ging[5].

Of significance are the values of the non-dimensional temperatures at the time of maximum tensile stress. For both heating and cooling, these are shown in Figure 43. Since thermal shock tests generally are carried out at values of Biot's modulus of unity or less, it may be seen that for both heating and cooling at the time of maximum stress the sphere is still relatively close to its initial temperature. Crandall and Ging, however, in their prediction of the thermal shock behavior of spherical shapes of alumina* from the mechanical and thermal properties, selected the property values at a temperature which corresponded to a temperature approximately half-way between the initial and final temperatures. In their predictions, Crandall and Ging obtained good agreement with experiment for thermal shock on heating. A large discrepancy, however, was found between the predicted values and experimental values for thermal shock on cooling. Since the discrepancy could possibly be due to the erroneous assumption of the temperature at which fracture occurred, it was decided to recalculate the predictions of Crandall and Ging.

In their investigation, Crandall and Ging developed a semi-empirical equation for the maximum temperature difference (ΔT_{max}) to which a sphere can be subjected without fracturing, given by:

$$\Delta T_{max} = \frac{2.5\, S_{ts}\,(1-\nu)}{\alpha E}\left(1+\frac{2}{\beta}\right) \quad ; \quad \beta = \frac{bh}{k} \tag{112}$$

In the physical property measurement the ratio of (h/k) was determined as a function of temperature and in the calculation of (T_{max}) they selected the ratio (h/k) at a temperature which was approximately half-way between the initial and final temperature of the thermal shock test, as discussed above. However, as shown in Figure 43, since the maximum tensile stress occurs at a temperature which lies close to (T_o), the correct value of thermal conductivity (k) should to a first approximation correspond to the initial temperature of the thermal shock test (T_o). Similarly, in the case of a temperature dependent surface heat transfer coefficient (h), the correct value of h should correspond to the temperature of the medium to which the sphere is subjected. Crandall and Ging did not report separate values of thermal conductivity and surface heat transfer coefficient for the thermal shock medium employed. These, therefore, had to be determined.

Crandall and Ging employed two initial temperatures in their thermal shock studies; namely, room temperature for thermal shock by heating and

*Coors Porcelain Company, Type AB-2.

700°C for thermal shock by cooling[44]. The final temperatures of the thermal shock test were varied until fracture was obtained. Data for the thermal conductivity of the alumina had to be determined at room temperature and 700°C only. The surface heat transfer coefficient, however, should be determined over the total temperature range in order to be able to calculate the expected temperature required for fracture (ΔT_{max}).

The value for thermal conductivity at room temperature obtained directly from Coors*, was 0.032 cal. deg.$^{-1}$ cm.$^{-1}$ sec.$^{-1}$. The thermal conductivity at 700°C was calculated from the thermal conductivity at 325°C as reported by Coors* by means of the temperature dependence of the thermal diffusivity as measured by Crandall and Ging[5] and the temperature dependence of the specific heat as reported by Goldsmith, et al[45]. The calculated thermal conductivity value at 700°C was found to be 0.0108 cal. deg.$^{-1}$ cm.$^{-1}$ sec.$^{-1}$.

The determination of the surface heat transfer coefficient of the salt bath** employed by Crandall and Ging presented greater difficulty.

In order to duplicate the condition of thermal shock as closely as possible the method selected to measure the surface heat transfer coefficient of the salt bath was to measure the transient temperature in the center of a sphere composed of a material of known thermal diffusivity and thermal conductivity suddenly submerged into the salt bath. The material selected consisted of Armco iron. Thermal conductivity of Armco iron has been reported by Powell[46] and thermal diffusivity by Cody, Abeles and Beers[47].

The two and one-quarter inch diameter sphere contained a small hole to the center to which a Chromel®-Alumel® thermocouple was inserted. The transient temperature of the center of the sphere when submerged into the salt bath was recorded with an x-y recorder. In order to reduce the effect of the temperature dependence of the thermal conductivity and thermal diffusivity the temperature difference to which the sphere was subjected was kept to approximately 50°C. The above procedure was followed at temperatures ranging from the melting point of the salt to approximately 700°C, the temperature at which the salt starts decomposing rapidly. Once the transient temperature of the center of the sphere was obtained, the logarithm of the relative temperature (μ) was plotted against non-dimensional time (θ), calculated from the time, the known thermal diffusivity and the radius of the sphere. The plot obtained was then compared with curves published by Heisler[48] of the transient temperature of the center of a sphere for various values of Biot's modulus. The value of Biot's modulus in the heat transfer experiment was obtained by interpolation between the curves of Heisler[48]. The thermal conductivity being known, the surface heat transfer coefficient was then readily calculated. Since the thermal diffusivity, as well as the thermal conductivity,

* Coors Data Sheet 0001, page 3.

** Hitec, E. I. duPont de Nemours,

of the Armco iron are a function of temperature, the value of the surface heat transfer coefficient was obtained by the above method from the thermal conductivity of both the starting and final temperature of the heat transfer experiment. The final results obtained of the surface heat transfer coefficient of the salt bath are shown in Figure 44. The scatter in the data obtained indicated an experimental error of approximately five to ten percent.

The predicted values of ΔT_{max} can now be calculated by means of equation (112).

Due to the temperature dependence of the surface heat transfer coefficient, ΔT_{max} cannot be calculated directly from (112), since the correct value of (h) depends on the value of (ΔT_{max}) which is unknown. The procedure which can be followed is to assume a value of (ΔT_{max}), select the appropriate value of (h) and calculate the value of (ΔT_{max}) based on this value of (h). In the case of disagreement between the assumed and calculated value of (ΔT_{max}), a new value is assumed and by a series of successive approximations one finally arrives at a value of (ΔT_{max}) at which the assumed and calculated value agree.

A graphical method, however, was devised which eliminates the use of the empirical relationship (112),as well as the method of successive approximations. Referring to Figure 42, it may be seen that the maximum non-dimensional stress is a function of Biot's modulus (β) only, and may be expressed by:

$$\frac{\sigma_{max}\ (1-\nu)}{\alpha E\ \Delta T} = f(\beta) \tag{113}$$

When the stress equals the tensile strength of the material, equation (113) may be written:

$$\frac{S_t\ (1-\nu)}{\alpha E \Delta T_{max}} = f(\beta) \tag{114}$$

Satisfying equality (114) then yields the desired value of (ΔT_{max}). The graphical method now consists of selecting various values of (ΔT_{max}) from which the corresponding value of (β) is calculated. The value of the non-dimensional stress which corresponds to the calculated value of (β) is then obtained from Figure 42. This value of non-dimensional stress, as well as the left-hand side of (114), are then plotted against the assumed values of (ΔT_{max}). For a given sphere size this will result in two curves at the intersection of which equation (114) is satisfied. The desired value of (ΔT_{max}) is then read from the (ΔT_{max}) axis.

This procedure was followed to obtain the predicted values of (ΔT_{max}) for thermal shock by heating and cooling. The mechanical and thermal properties

used for these calculations were taken directly from the paper by Crandall and Ging[5]. For thermal shock by heating, these were S_{ts} = 19,800 psi, υ = 0.27, α = 6.1 x $10^{-6}/^{o}C$, E = 30.95 x 10^{6} psi. For thermal shock on cooling the values used were S_{ts} = 14,800 psi, υ = 0.15, α = 8.7 x $10^{-6}/^{o}C$ and E = 29.3 x 10^{6} psi. Figure 45 shows the results of the graphical method used to predict the values of (ΔT_{max}) for thermal shock on heating. Similarly, Figure 46 shows the results for thermal shock on cooling. The values predicted in the present investigation, as well as these predicted by Crandall and Ging, are compared with the observed values in Table No. XXX. Excellent agreement was obtained. From these results, it can be concluded that if the material properties of a material are known and an analytical solution exists for the thermal stresses which arise for a thermal shock test of given severity, it is entirely possible to predict the thermal shock behavior, obtaining good agreement with experiment.

Some argument may be presented with regard to the temperature level at which the material properties were selected. On cooling, fracture is initiated at the surface. The value for tensile strength might, therefore, be selected at a temperature somewhat lower than the starting temperature since at fracture the sphere will have cooled down somewhat. This, however, will increase the predicted value of ΔT_{max} by only a few percent. Near room temperature the tensile strength is practically independent of temperature, therefore, no difficulty exists in selecting the proper value of strength for thermal shock on heating. Similarly, for thermal shock on heating and cooling no difficulty exists at which temperature the values of the coefficient of thermal expansion (α), and Young's modulus of elasticity (E) are selected, since the product (α E) to a first approximation is independent of temperature.

The choice of the correct value of thermal conductivity could introduce the greatest uncertainty. Since thermal conductivity at temperatures near room temperature is strongly temperature dependent, considerable error could be introduced in the prediction of ΔT_{max} for thermal shock by heating.

For thermal shock on cooling the selection of the correct value of thermal conductivity is less critical since at the higher temperatures thermal conductivity is less strongly dependent on temperature than at temperature near room temperature.

It may be argued that the value thermal conductivity should be selected at a value of surface temperature which lies between the initial temperature and the temperature of the surface at the time of maximum stress. However, it should be kept in mind that due to the temperature dependence of the thermal diffusivity the temperature distribution is distorted in such a manner as to lower the tensile stresses for thermal shock on heating and to increase the tensile stresses for thermal shock on cooling. This, therefore, at least partially offsets any error introduced when the value of thermal conductivity

is selected at the initial temperature of the thermal shock test.

Including the temperature dependence of thermal conductivity and thermal diffusivity in the thermal stress calculations becomes exceedingly complex and will require the use of high-speed electronic computers. Even then the problem will be quite lengthy. A quantitative prediction of the effect of the temperature dependence of thermal conductivity and thermal diffusivity on the thermal stress level at this stage is still impossible.

In their investigation, Crandall and Ging[5] also subjected alumina spheres to thermal shock by heating in air. The same approach as used above can be applied to these results. However, since high temperatures were required to initiate fracture in the spheres, heat transfer occurred principally by thermal radiation. This was treated successfully in Appendix B.

TABLE NO. XXVIII

Maximum Tensile Stress, Time of Maximum Stress, and Temperature at Time of Maximum Stress, in Spheres Subjected to Thermal Shock by Heating in a Medium of Constant Surface Heat Transfer Coefficient

Biot's Modulus	Non-Dimensional Stress $\frac{\sigma(1-\upsilon)}{\alpha E \Delta T}$	Non-Dimensional Time of Maximum Stress $\frac{at}{b^2}$	Non-Dimensional Temperature		
			Center	Surface	Mean
0.05	0.0095	0.2649	0.0245	0.0484	0.0388
0.1	0.0184	0.2317	0.0385	0.0845	0.0661
0.2	0.0346	0.1994	0.0573	0.1437	0.1092
0.5	0.0744	0.1593	0.0861	0.2719	0.1977
1.0	0.1230	0.1320	0.1032	0.4099	0.2877
2.0	0.1855	0.1085	0.1090	0.5704	0.3873
5.0	0.2706	0.0850	0.0978	0.7672	0.5037
10.0	0.3197	0.0732	0.0843	0.8713	0.5638
16.0	0.3424	0.0678	0.0768	0.9173	0.5904
101.0	0.3785	0.0591	0.0630	0.9866	0.6308

TABLE NO. XXIX

Maximum Tensile Stress, Time of Maximum Stress, and Temperature at Time of Maximum Stress, in Spheres Subjected to Thermal Shock on Cooling in a Medium of Constant Surface Heat Transfer Coefficient

Biot's Modulus	Non-Dimensional Stress $\frac{\sigma(1-\upsilon)}{\alpha E \Delta T}$	Non-Dimensional Time of Maximum Stress $\frac{at}{b^2}$	Non-Dimensional Temperature		
			Center	Surface	Mean
0.05	0.0096	0.2090	0.9834	0.9596	0.9692
0.10	0.0185	0.1756	0.9766	0.9309	0.9494
0.20	0.0350	0.1428	0.9707	0.8854	0.9204
0.50	0.0766	0.1016	0.9712	0.7913	0.8680
1.0	0.1304	0.0733	0.9819	0.6944	0.8248
2.0	0.2070	0.0492	0.9946	0.5833	0.7903
5.0	0.3386	0.0260	0.9999	0.4355	0.7741
10.0	0.4500	0.0148	0.9986	0.3371	0.7870
16.0	0.5255	0.0094	0.9849	0.2830	0.8085

TABLE NO. XXX

Predicted and Observed Temperature Difference (°C) Required to Fracture Alumina Spheres by Thermal Shock in a Liquid Salt Bath

1. Heating

	Sphere Diameter (in)				
	1	1-1/4	1-1/2	2	3
Calculated by Crandall and Ging	736	648	559	448	352
Calculated by present authors	680	625	585	530	455
Observed	722	600	575	540	500

2. Cooling

Calculated by Crandall and Ging	736	648	559	448	352
Calculated by present authors	280	240	-	-	-
Observed	250	230	-	-	-

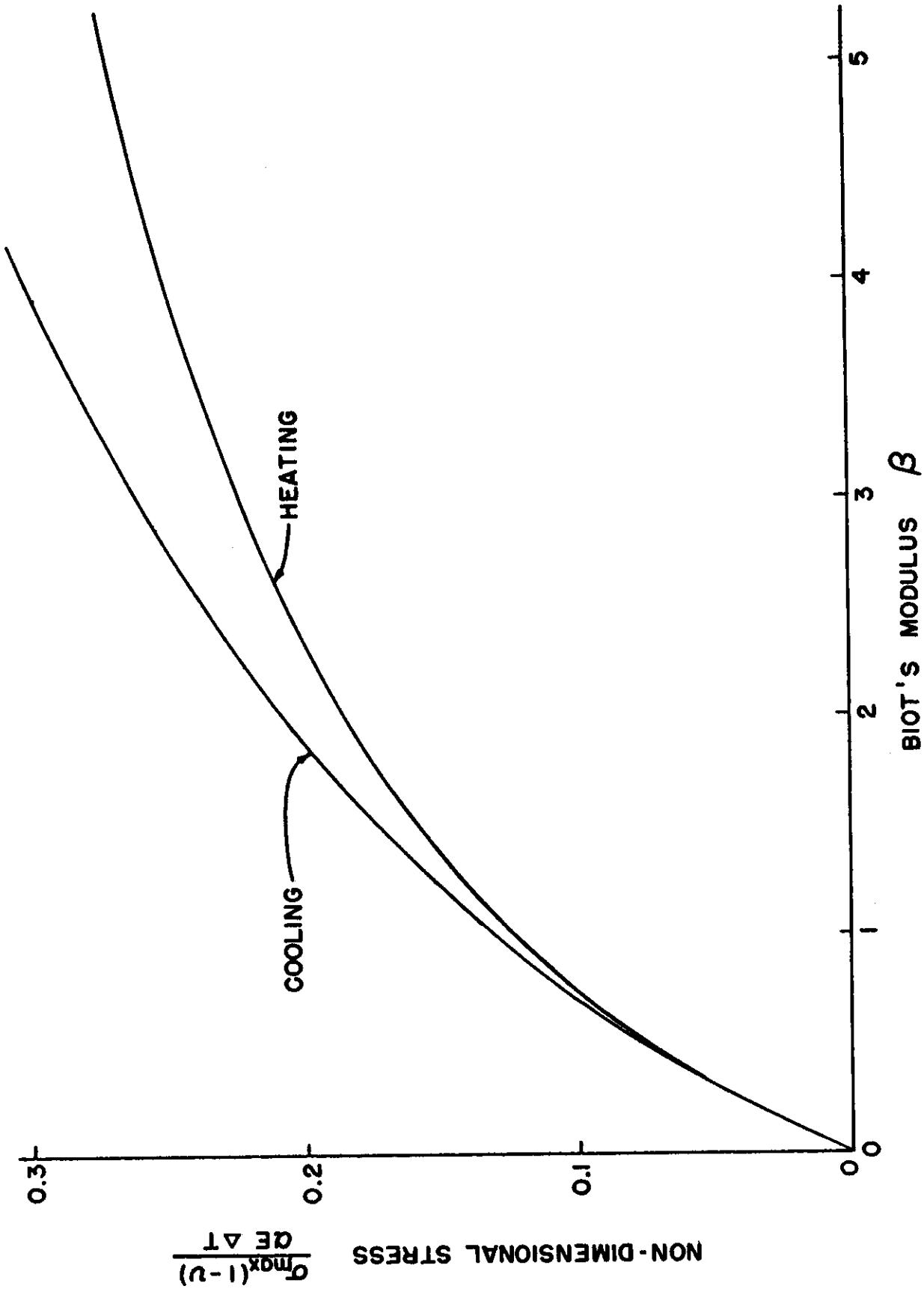

Figure 42 - Non-Dimensional Maximum Tensile Stress in a Sphere Subjected to Thermal Shock in a Medium With Constant Surface Heat Transfer Coefficient.

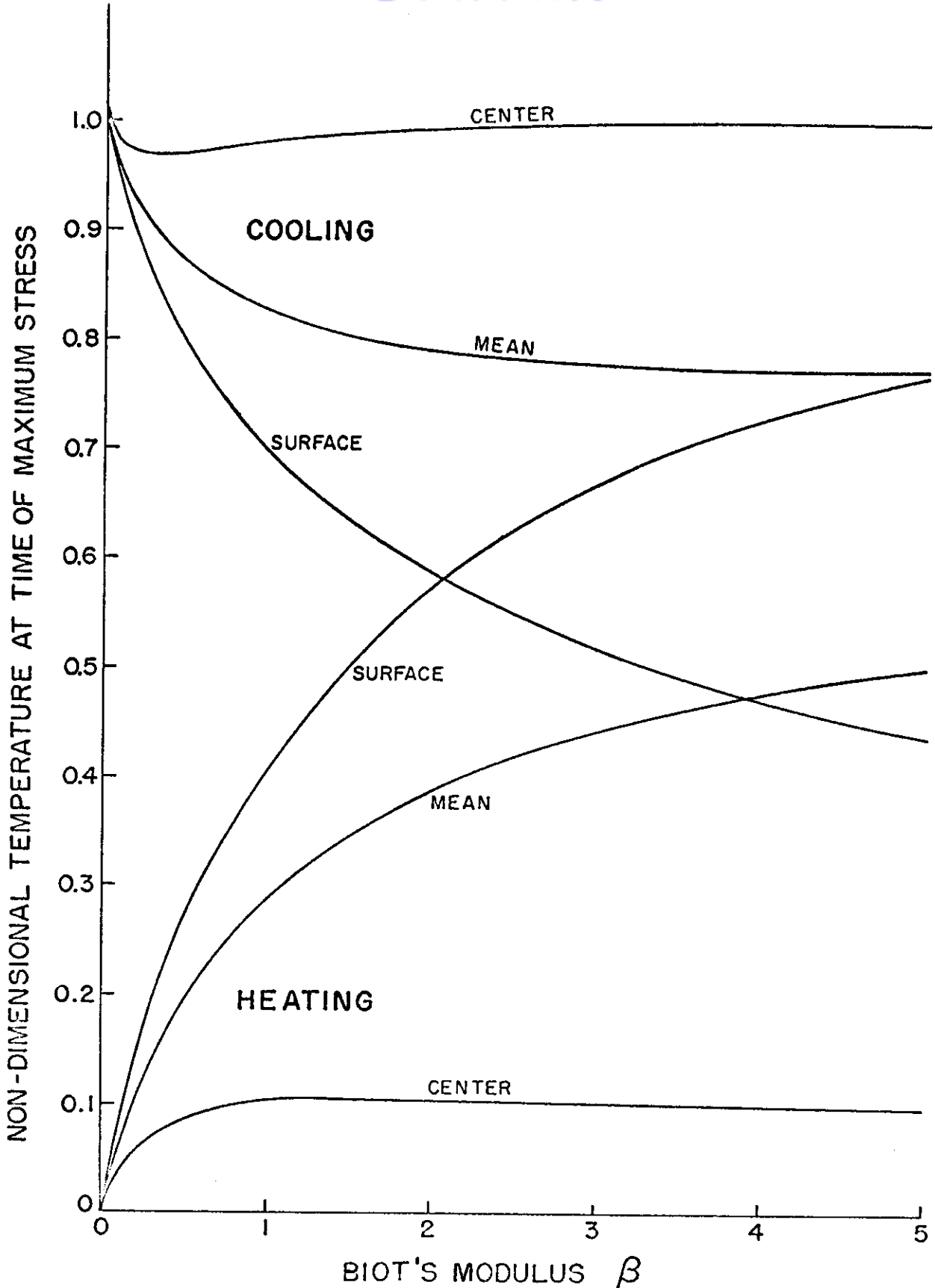

Figure 43 - Non-Dimensional Center, Surface and Mean Temperature at Time of Maximum Stress in a Sphere Subjected to Thermal Shock in a Medium With Constant Surface Heat Transfer Coefficient.

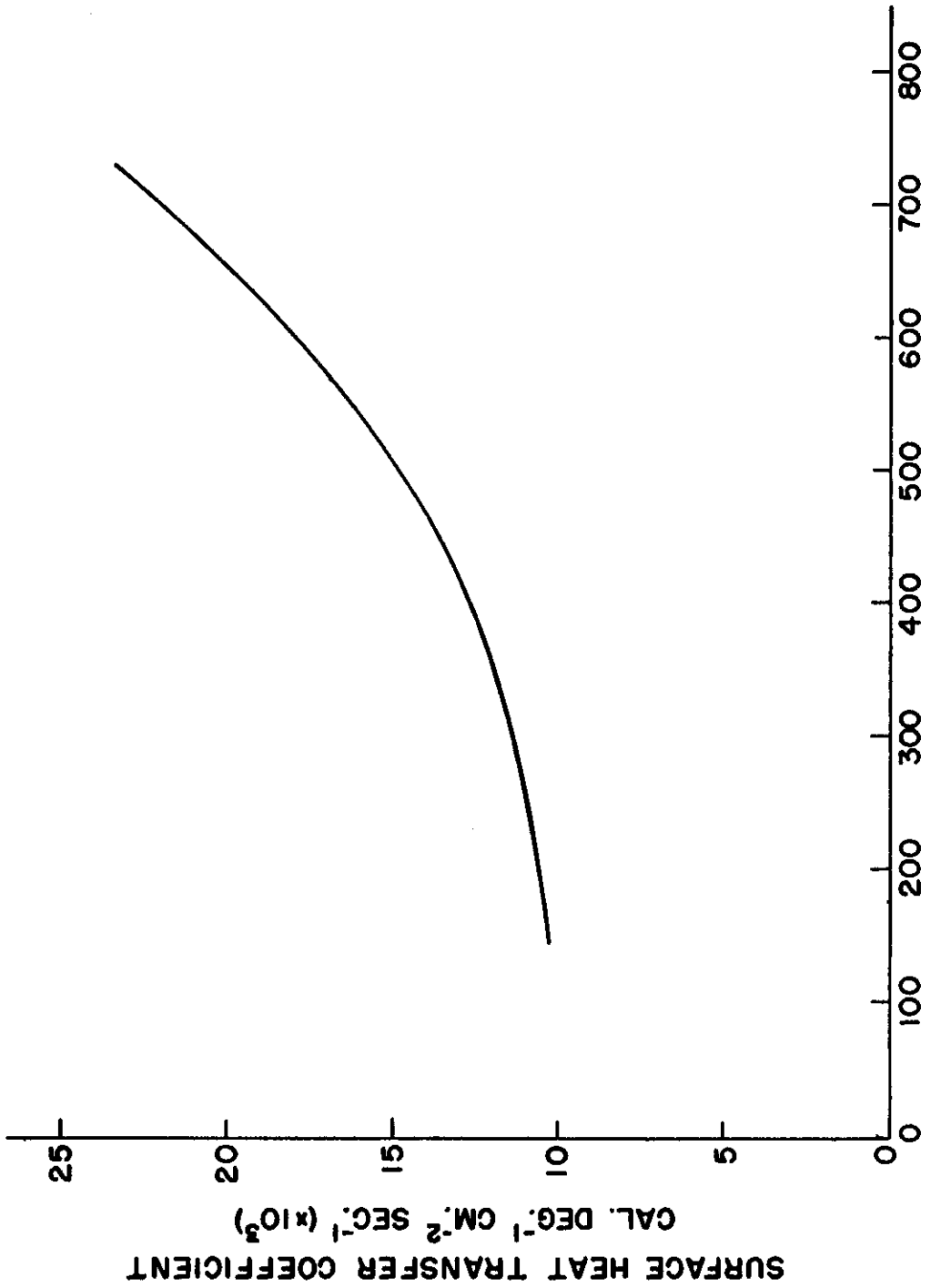

Figure 44 - Surface Heat Transfer Coefficient for a Two and One-Quarter Inch Diameter Sphere in Salt Bath.

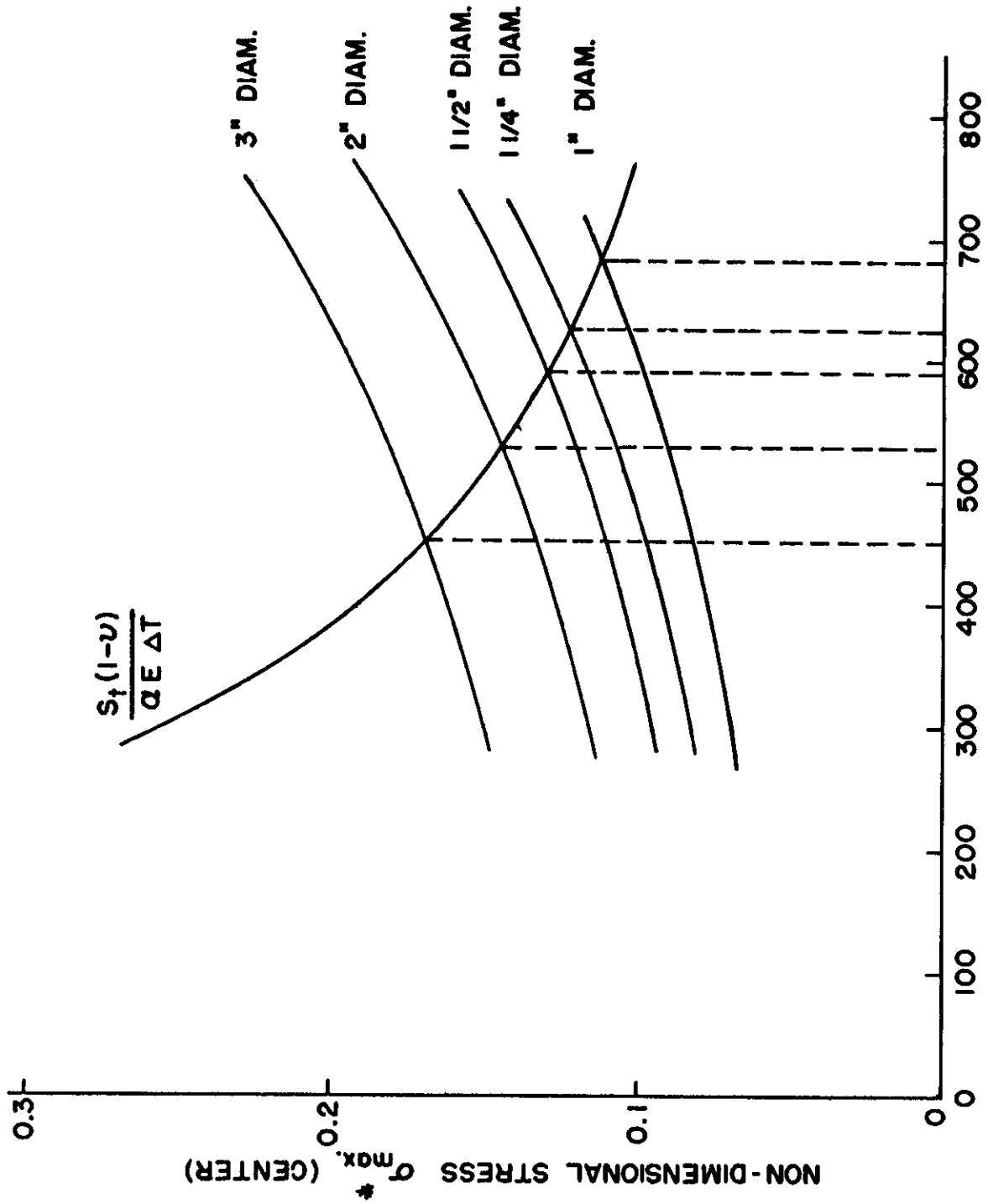

Figure 45 - Graphical Solution for Determining Temperature Difference Required to Fracture Alumina Spheres by Thermal Shock on Heating in Salt Bath.

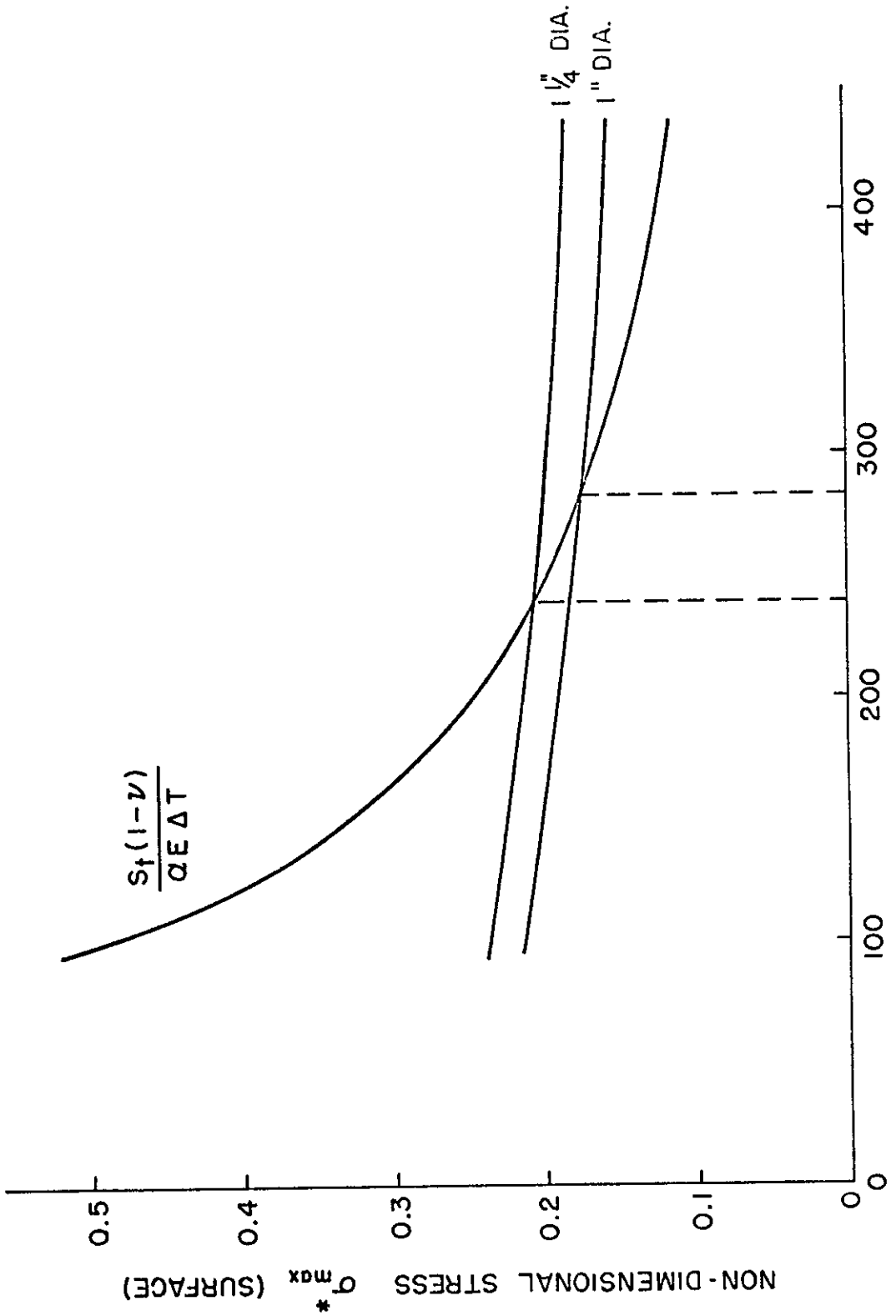

Figure 46 - Graphical Method for Determining Temperature Difference Required to Fracture Alumina Spheres by Thermal Shock on Cooling in Salt Bath.

APPENDIX D

CALCULATION OF THE TENSILE STRENGTH OF SPHERICAL SHAPES UNDER CONDITIONS OF THERMAL SHOCK FROM THE BEND STRENGTH OF RECTANGULAR BARS

In design with brittle materials, one of the major problems is that the strength values of a material obtained under a given condition of stress and body size cannot be arbitrarily employed in the prediction of the fracture behavior of a body of different size and containing a different stress distribution.

The same holds true in this investigation where strength values were obtained by bending rectangular bars, although the actual strength desired is the tensile strength of a sphere under conditions of thermal shock.

These difficulties can be overcome by employing Weibull's[25] statistical theory of strength. Weibull's theory is based on the concept that brittle materials contain a large number of flaws, which appreciably lower the strength of the material from its theoretical strength.

These flaws are assumed to be of random size and distributed throughout the body. The assumption is also made that when the stress at the worst flaw contained within the body becomes large enough to transform it into a propagating crack, the entire body fails (weakest link theory of failure).

Weibull's mathematical formulation adequately described elsewhere[25, 49] consists of calculating the probability of failure of a body of given size containing a given stress distribution.

Briefly, when a stress (σ) acts over a volume (dV) in a body in which the number and size of flaws can be related to a constant (m), (where m is a homogeneity factor; the higher the value of m the more homogeneous is the material) and having a strength constant (S_o) (related to some inherent strength of the material), the probability of failure (P) is:

$$P = \frac{1}{(S_o)^m} \int_V \sigma^m \, dV \qquad (115)$$

The integration is performed over the total volume subjected to tensile stress.

Actually Weibull suggests a more general form given by:

$$P = \frac{1}{(S_o)^m} \int_V (\sigma - \sigma_u)^m \, dV \qquad (116)$$

where σ_u is a stress level below which no failures are to be expected. However, for reasons of simplicity equation (115) will be employed.

In the present investigation, the calculation consists of determining the probability of fracture of rectangular bars and the probability of fracture of a sphere heated by radiation. Equating the two probabilities will enable one to calculate the tensile strength of the sphere subjected to thermal shock from the flexural strength of the rectangular bars.

1. Calculation of the Probability of Fracture of a Rectangular Bar Subjected to Center Loading.

Shown in Figure 47 is a rectangular bar of length (2L), thickness (2d) and width (b) subjected to a center loading. Regarding the part of the bar to the right of the central load and taking the origin on the neutral axis at the right end of the bar, the tensile stress in any part of the bar is given by:

$$\sigma = S_{tb} \frac{xy}{dL} \tag{117}$$

where S_{tb} is the calculated tensile strength in bending at the time of fracture.

Using equation (115), the probability of fracture by bending (P_{tb}) is given by:

$$P_{tb} = \frac{2}{(S_o)^m} \int_0^L \int_0^d b(\sigma_{tb})^m \left(\frac{xy}{dL}\right)^m dxdy \tag{118}$$

$$= 2\left(\frac{S_{tb}}{S_o}\right)^m \frac{b}{d^m L^m} \int_0^L \int_0^d x^m y^m dxdy \tag{119}$$

$$= \frac{2bdL}{(m+1)^2} \left(\frac{S_{tb}}{S_o}\right)^m \tag{120}$$

Since the total volume of the bar $V_{bar} = 4\,bdL$, the expression for P_{tb} can be written:

$$P_{tb} = \frac{V_{bar}}{2(m+1)^2} \left(\frac{S_{tb}}{S_o}\right)^m \tag{121}$$

A similar equation can be derived for the probability of fracture of a rectangular bar subjected to two-point loading. This is given by:

$$P_{tb} = \frac{V_{bar}}{2(m+1)} \left(\frac{S_{tb}}{S_o} \right)^m \qquad (122)$$

where now V_{bar} is the volume of the bar between the two center loading points.

2. Calculation of the Probability of Failure of a Sphere Subjected to Thermal Shock on Heating

A sphere subjected to thermal shock on heating is subjected simultaneously to a system of radial and tangential stresses. Throughout the volume of the sphere, the material is subjected to a condition of triaxial stress. At the time of fracture the radial stress (σ_r) can be expressed by (See Appendix A):

$$\sigma_r = S_{ts} \left[1 - \frac{r^2}{b^2} \right] \qquad (123)$$

where S_{ts} is the tensile strength of the material under conditions of thermal shock and b is the radius of the sphere.

Similarly, the tangential stresses (σ_θ) can be given by (See Appendix A):

$$\sigma_\theta = S_{ts} \left[1 - \frac{2r^2}{b^2} \right] \qquad (124)$$

The radial stress can be seen to be tensile throughout the whole volume of the sphere. The tangential stresses are tensile at the center and compressive at the surface of the sphere.

Due to the existence of a triaxial stress state the calculation of the probability of failure of the sphere should take into account the effect of a multiple stress state on the value of the uniaxial tensile strength.

The maximum stress theory states that the fracture stress in combined stress state (except biaxial and triaxial compression) is the same as in uniaxial tension. The distortion energy theory predicts a higher value for fracture stress under conditions of biaxial tension than the uniaxial fracture stress.

Experimental findings on brittle materials such as glass and plaster by Davidenkov, et al.[50] showed the same tensile strength values for biaxial stress as for uniaxial stress for a tensile stress ratio of unity and for a compressive to tensile stress ratio as high as four. This is in support of the maximum stress theory. Similar findings were obtained by Salmassy, et al.[49].

Assuming that these findings can be applied to the system under study it is sufficient in the calculation of the probability of failure of the sphere to calculate the probability of failure due to one stress system only. Since the radial tensile stress throughout the volume of the sphere exceeds the tangential tensile stress and since it also acts over a larger volume, at first sight the probability of failure should be calculated on the basis of the radial stress system rather than the tangential stress system. The expression obtained for the probability of failure for a sphere under conditions of thermal shock is, therefore, based on a combination of the maximum stress theory and Weibull's statistical theory of strength.

The probability of failure (P_{ts}) of the sphere under conditions of thermal shock on heating in terms of the radial stress is then given by:

$$P_{ts} = 4\pi \left[\frac{S_{ts}}{S_o} \right]^m \int_o^b \left[1 - \frac{r^2}{b^2} \right]^m r^2 dr \qquad (125)$$

Writing $\frac{r^2}{b^2} = x$, (125) can be written in a more convenient form given by:

$$P_{ts} = \frac{4\pi b^3}{2} \left[\frac{S_{ts}}{S_o} \right]^m \int_o^1 (1-x)^m x^{1/2} dx \qquad (126)$$

which upon integration gives:

$$P_{ts} = 2\pi b^3 \left[\frac{S_{ts}}{S_o} \right]^m B(3/2, m+1) \qquad (127)$$

where B(n, p) is the Beta function of n, p.

Since the volume of the sphere (V_{sphere}) is given by:

$$V_{sphere} = \frac{4\pi b^3}{3} \qquad (128)$$

equation (127) can be expressed in terms of the volume of the sphere by:

$$P_{ts} = 3/2\, V_{sphere} \left[\frac{S_{ts}}{S_o} \right]^m B(3/2, m+1) \qquad (129)$$

Another approach to the question of which stress system is responsible for fracture of the sphere by thermal shock is to regard it from the point of view of crack propagation.

Illustrated in Figure 48a is a sphere subjected to thermal shock on heating containing a small elliptical flaw at its center. This flaw, regardless of its orientation, once it has been transformed into a propagating crack will propagate along a plane which dissects the sphere through its center. Figure 48b shows a magnified view of the tip of the flaw. The direction of crack propagation may be seen to be parallel to the radial stresses and perpendicular to the tangential stresses. The release of elastic energy which is the driving force for crack propagation is provided principally by the tangential stress system. Therefore, a flaw located at the center can be transformed into a propagating crack under the influence of the tangential stresses only. The radial stresses might also transform a flaw into a propagating crack but will require a much higher stress level to do so.

For flaws located away from the center, the radial stress system can provide energy for crack propagation but due to the decrease in stress level the overall probability of failure due to the radial stresses is still small compared to the probability of failure due to the tangential stress system.

The argument presented above may be applied to any biaxial or tri-axial stress state and possibly offers an explanation for the experimental evidence in support of the maximum stress theory.

In terms of Weibull's theory the probability of failure of the sphere due to the tangential stresses is then given by:

$$P_{ts} = 4\pi \left[\frac{S_{ts}}{S_o}\right]^m \int_o^{\frac{b}{\sqrt{2}}} \left[1 - \frac{2r^2}{b^2}\right] r^2 dr \qquad (130)$$

where the integration is performed over the volume where the tangential stress is tensile only.

Writing $\frac{2r^2}{b^2} = x$, equation (130) can be simplified to:

$$P_{ts} = \frac{\sqrt{2}}{2} \pi \, b^3 \left[\frac{S_{ts}}{S_o}\right]^m \int_o^1 (1-x)^m \, x^{1/2} \, dx \qquad (131)$$

$$= \frac{\sqrt{2}}{2} \pi b^3 \left[\frac{S_{ts}}{S_o}\right]^m B(3/2, m+1) \quad (132)$$

Since the volume of the sphere V_{sphere} equals $\frac{4\pi b^3}{3}$, (132) can be written:

$$P_{ts} = \frac{3\sqrt{2}}{8} V_{sphere} \left[\frac{S_{ts}}{S_o}\right]^m B(3/2, m+1) \quad (133)$$

It may be noticed that the probability of failure due to the tangential stresses is considerably less than due to the radial stresses calculated previously.

3. Calculation of the Tensile Strength Under Conditions of Thermal Shock From the Bending Strength of Rectangular Bars

By equating the probability of failure of the rectangular bar to the probability of failure of the sphere, an expression is obtained from which the strength of the sphere subjected to thermal shock can be calculated from the bending strength of the rectangular bar.

For failure to occur due to the radial stress equating (122) and (129) gives:

$$\frac{V_{bar}}{2(m+1)^2}\left[\frac{S_{tb}}{S_o}\right]^m = 1.5\, V_{sphere}\left[\frac{S_{ts}}{S_o}\right]^m B(3/2, m+1) \quad (134)$$

After cancellation of S_o and simplification, the expression for S_{ts} in terms of S_{tb} is given by:

$$S_{ts} = S_{tb}\left[\frac{V_{bar}}{V_{sphere}}\right]^{1/m}\left[\frac{1}{3(m+1)^2\ B(3/2, m+1)}\right]^{1/m} \quad (135)$$

For failure due to the tangential stress, a similar expression is given by:

$$S_{ts} = S_{tb}\left[\frac{V_{bar}}{V_{sphere}}\right]^{1/m}\left[\frac{4}{3\sqrt{2}(m+1)^2\ B(3/2, m+1)}\right]^{1/m} \quad (136)$$

The value of m for a given material can be obtained experimentally by determining the bend strength of two sets of rectangular bars of volumes V_1 and V_2, yielding bend strengths S_{1b} and S_{2b}. The value of m is then calculated* from:

$$m = \log\left[\frac{V_2}{V_1}\right] / \log\left[\frac{S_{1b}}{S_{2b}}\right] \quad (137)$$

*See Experimental Results and Table No. XIII.

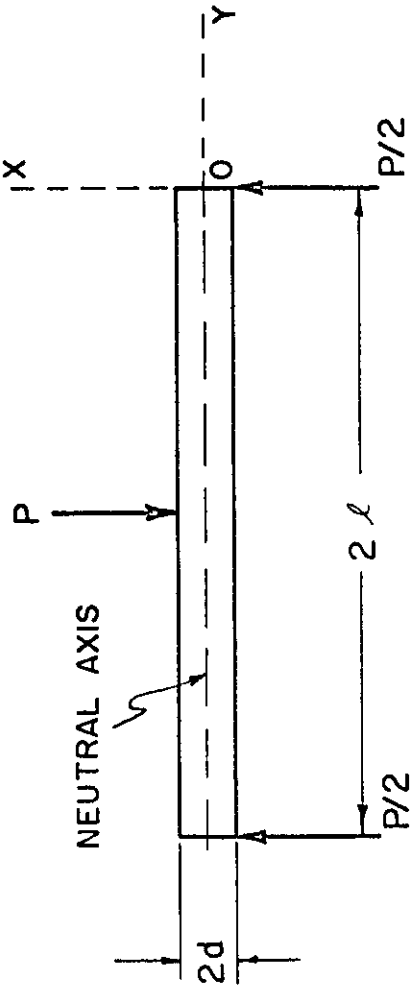

Figure 47 - Modulus of Rupture Bar Subjected to Three-Point Loading.

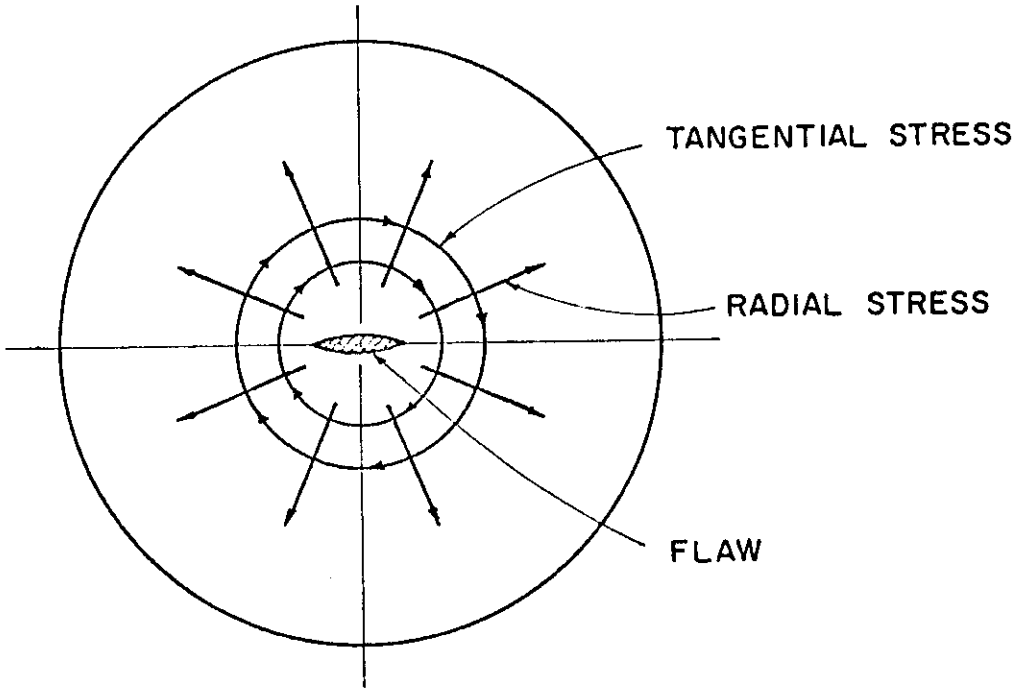

(a.)

Figure 48a - Stresses in a Sphere Subjected to Thermal Shock.

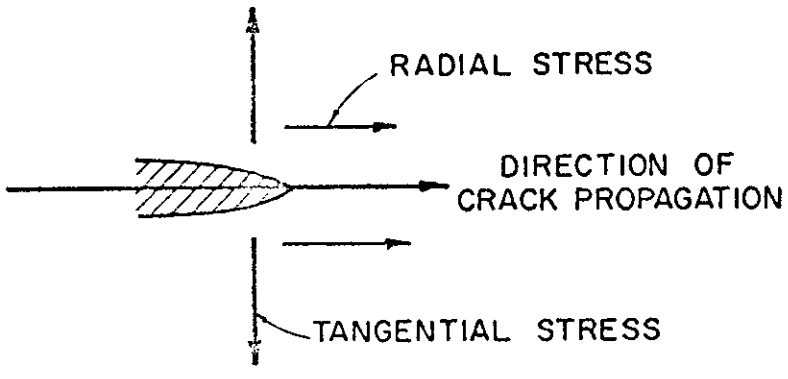

(b.)

Figure 48b - Thermal Stresses at Flaw Located Near the Center of the Sphere.

APPENDIX E

GENERAL DERIVATION* OF STATISTICAL EQUATIONS USED IN CURVE-FITTING FOR MODULUS OF ELASTICITY AND STRENGTH DATA

The general equations used in the curve-fitting of the experimental data can be reduced to the rational form given by:

$$f(x) = \frac{1 + A_{01}\,x + A_{02}\,x^2 + \ldots + A_{on}\,x^n}{A_{10} + A_{11}\,x + A_{12}\,x^2 + \ldots + A_{1n}\,x^n} \tag{138}$$

or the implicit form:

$$C\,f(x,y) = 1 \tag{139}$$

where in the last case, C is the only undetermined parameter.

The resultant formulas are all best fitting in the Gaussian (least square) sense that $\sum \epsilon^2$ is minimized for k given points (x_i, y_i).

The unconventional residual

$$\epsilon = A_{10}f + A_{11}\,x\,f + \ldots + A_{1n}\,x^n f - A_{01}\,x - A_{02}\,x^2 - \ldots - A_{0n}\,x^n - 1, \tag{140}$$

has been used for (138) to avoid the well known difficulties with non-linear parameters pointed out by Scarborough[51].

The unconventional residual

$$\epsilon = Cf - 1 \tag{141}$$

has been used for (139) to produce the convenient computational technique

$$C = \frac{\sum f}{\sum f^2} \tag{142}$$

The computational technique used to minimize the sum of the squares of the residuals (140) is the pseudo-matrix technique of Moore[52].

* The writer is indebted to Mr. C. Maley, Mathematician of the Quality Control Branch, for this appendix.